NTNU – Trondheim
Norwegian University of
Science and Technology

Relating acoustic wave velocities to formation mechanical properties

Linn Tove Brandås

Earth Sciences and Petroleum Engineering
Submission date: May 2012
Supervisor: Erling Fjær, IPT
Co-supervisor: Johan Tronvoll, Weatherford Petroleum Consultants AS

Norwegian University of Science and Technology
Department of Petroleum Engineering and Applied Geophysics

Abstract

Proper correlation between formation mechanical properties and acoustic data is essential for acquiring field rock mechanical data for analysis, and it has thereby a great significance to oilfield development.

This thesis presents results from a correlation study between formation mechanical properties and acoustic wave velocities from a set of unpublished rock mechanical experiments on sandstone samples from the Norwegian shelf. The core samples from the Norwegian shelf were subjected to triaxial compression tests performed at various confining pressures with simultaneous measurements of acoustic velocities. Correlations between formation compressive strength, elastic stiffness and Poisson's ratio and compressional and shear transit time have been established.

The results obtained in this study confirm that the stress level and the stress configuration affect the acoustic velocities, and this should be accounted for when using generalized empirical correlations to estimate formation strength, elastic stiffness and Poisson's ratio from acoustic logs in field studies. The empirical correlations established through this work are found to match reasonable well with other published relations. By acoustic logs from field studies, it is found that the empirical correlations overestimate the formation strength and the elastic stiffness.

Sammendrag

Riktig korrelasjon mellom formasjon mekaniske egenskaper og akustiske data er viktig for å tilegne bergmekanisk data i feltet for analyse, og den har dermed stor betydning for oljefelt-utvikling.

Denne avhandlingen presenterer resultater fra en korrelasjons studie mellom formasjon mekaniske egenskaper og akustiske hastighetene fra et sett upubliserte bergmekaniske eksperimenter på sandstein prøver fra norsk sokkel. Kjerne prøvene fra norsk sokkel ble utsatt for triaksial kompresjons tester utført ved ulike omslutningstrykk med samtidige målinger av akustiske hastigheter. Korrelasjoner mellom formasjon mekanisk styrke, elastisk stivhet og Poisson's forhold og kompresjons- og skjær transit tid har blitt fastslått.

Resultatene oppnådd i denne studien bekrefter at stress nivået og stress konfigurasjonen påvirker de akustiske hastighetene, og dette bør gjøres rede for ved bruk av generaliserte empiriske korrelasjoner til å anslå formasjonsstyrke, elastisk stivhet og Poisson's forhold fra akustiske logger i feltstudier. De empiriske korrelasjonene etablert gjennom dette arbeidet er funnet å samsvare rimelig godt med andre publiserte relasjoner. Ved bruk av akustiske logger fra feltstudier ble det funnet at de empiriske korrelasjonene overestimerte formasjonsstyrken og den elastiske stivheten.

Acknowledgements

I would like to express my deepest gratitude to Erling Fjær, my supervisor at the Norwegian University of Science and Technology (NTNU). He has offered me guidance and support throughout my last year at NTNU, and through his enthusiasm and encouragement I have given my best in this thesis.

I would also like to thank Johan Tronvoll for his guidance and help in the last year, I am sure he is the reason for me gaining such an interest in rock mechanics. For all the hours collecting data in the laboratory and for all the questions related to the rock mechanical tests, I give my thanks to Karl Tokle. And I thank Arent Arntzen, for help related to the mathematical questions and the programming in R.

For the opportunity to perform and publish this study, I would like to express my appreciation to Statoil and Weatherford Laboratories.

And finally, I would like to thank my class mates for five wonderful years at NTNU. The atmosphere and solidarity have made these years unforgettable. And last, I give my appreciations to my family, for support through these years, and to my fiancé Ole Christian Hovstein, for putting up with me through all the exams and all the stress every year, and for helping me giving the best of me throughout my study.

Table of Contents

List of Figures

List of Tables

Appendix

1. Introduction

1.1 Goal of study

The challenge is *how to estimate correct formation mechanical properties by the use of dynamic measurements*, since the conversion from dynamic measurements to static parameters is not straight forward. The purpose of this thesis is to suggest models for this.

In addition, the aim is to compare the obtained models against log data from wells where plug samples already have been tested in a laboratory, and thereby the formation mechanical properties are known from static measurements.

1.2 Methodology

Formation mechanical properties obtained from static measurements are acquired from Weatherford Laboratories and Statoil. The utilized data have been subjected to the same type of plug preparation, followed by a standard triaxial compression test (TCT). Series of experimental results have been analyzed though series expansion performed with a set of parameters (including confining pressure) for each elastic parameter, this by the use of the least squares method. By this method, the sum of errors (i.e. difference between estimated and measured value), is set to be as small as possible by tuning a number of constants. The estimated values are plotted against the measured values to judge the goodness of fit.

The confining pressure is then set equal to zero for each obtained model, and the resulting values are plotted as a function of compressional and shear transit time. The best fit through the obtained values are then found, resulting in the respective empirical equation for each plot. A statistical analysis is also performed for each model, this by the use of the open source programming language and software environment for statistical computing and graphics R.

Finally, the obtained empirical equations are compared to log data from Statoil, this to confirm the validity of the obtained models. The results are also compared to a set of equations from already published literature.

1.3 Scope

The utilized data set is limited to unpublished triaxial compression test data on core samples from the Norwegian shelf, and the validity of the results are thereby also limited to this area. The obtained models should therefore be used with care for any other data. The obtained empirical models are also limited to be used for sandstone samples.

The static measurements performed on these plug samples were obtained by triaxial compression tests with different confining pressures, and all values are thereby not in itself representative for a zero confining pressure environment.

1.4 Master thesis layout

A brief introduction to the basic rock mechanical properties needed for geomechanical analyses in oilfield development is provided along with a short definition of static and dynamic measurements (Chapter 2).

Chapter 3 gives an overview of the available data for this study, including a description of the method used when preparing the plug samples for the laboratory test and a description of the laboratory test itself.

A number of empirical equations from literature are presented in Chapter 4, along with an introduction to sonic transit time.

In Chapter 5, all calculations and their respective results are listed for all parameters. Also listed in this chapter are the obtained models for each parameter.

Chapter 6 includes statistical analyses of the obtained models, and their respective empirical equations. These statistical analyses have been performed by the open source programming language and software environment for statistical computing and graphics R.

And finally, in Chapter 7, the obtained empirical equations are compared to log data to confirm their validity. The empirical equations are also compared to other empirical relations from literature.

Suggestions for further work, and discussion related to the obtained results are given in Chapter 8 and Chapter 9, respectively.

2. Background

Geomechanics analysis has gradually become an integrated part of oilfield development. This includes several topics such as pre-drill wellbore stability analyses, utilizing seismic for pore pressure estimation and basic data acquisition during exploration. Before drilling a well and developing a field, the stability of the drill site must be estimated and further on determined to avoid critical issues, e.g. stuck pipe. Pore pressure estimation is also a critical evaluation, as it may lead to blow out or wellbore failure. These are dangerous hazards that not only could danger people on drill site and the environment; such events will also result in great economic losses. During the development phase, further wellbore stability issues are faced, as well as sand production risk analysis which also may cause great concerns in the oilfield development. And further on in the production phase, hydraulic fracture stimulation can be used in terms of production optimization, and reservoir compaction as a result of drainage must be addressed and analyses of stress-dependent permeability for infill well placement can be performed.

2.1 Formation mechanical properties

Basic rock mechanical properties must be determined or estimated for all the applications in the oil and gas industry mentioned above. Such properties are formation mechanical properties, elastic properties and plastic properties. Examples of formation mechanical properties are compressive and tensile strength. These parameters describe the maximum strength a material can endure before going into shear or tensile failure respectively.

When a test sample is subjected to axially directed forces, the test sample is crushed or fails when its limit of compressive strength is reached. The unconfined compressive strength (UCS) is related to when the confining pressure is zero, and is usually determined by the uniaxial compressive test or the triaxial compressive test, where the latter require the use of the Mohr-Coulomb theorem to determine the UCS. These tests will be given a more thoroughly introduction in section 3.4 and 3.3, respectively.

When the effective tensile stress across some plane in the plug samples exceeds a critical limit, the material will go into tensile failure (Fjær et al. 1992). The tensile strength of a material is determined by the tensile test, but can also be given from the Brazilian test (see Appendix B.6)

2.2 Elastic properties

Some materials have the ability to deform elastically, i.e. the deformation is not permanent and the material will go back to its original state after the applied force is removed. This tendency is described by a set of elastic moduli which is given as the slope of the stress - strain curve in the region of elastic deformation. There are several types of elastic moduli, given from specifications of how the appropriate stress (denoted σ) and strain (denoted ε) are measured, and in which direction they are to be measured. Young's modulus and Poisson's ratio will be briefly mentioned and described below.

2.2.1 Young's modulus

Young's modulus describes the stiffness of the sample (Fjær et al. 1992), which is the plug sample's ability to resists compression by uniaxial stress. Young's modulus is denoted E, and is defined as the ratio of the extensional stress to the extensional strain;

$$E = \frac{\sigma_{zz}}{\varepsilon_{zz}} \tag{2-1}$$

when $\sigma_{xx} = \sigma_{yy} = \sigma_{xy} = \sigma_{xz} = \sigma_{yz} = 0$ which is given as uniaxial stress state.

This parameter is often called the modulus of elasticity, as it is the most common used parameter of the elastic moduli. It is also important to state that Young's modulus depend of the direction it is measured, thereby resulting in that anisotropic materials have different Young's modulus depending on the direction of the force applied.

2.2.2 Poisson's ratio

Poisson's ratio is a dimensionless parameter that measures the ratio of lateral expansion to longitudinal contraction. This is a result of the common trend of materials, which is that they tend to expand in the directions perpendicular to the direction they are compressed. Poisson's ratio is denoted v and is given as;

$$\nu = -\frac{\varepsilon_{xx}}{\varepsilon_{zz}} \tag{2-2}$$

when $\sigma_{xx} = \sigma_{yy} = \sigma_{xy} = \sigma_{xz} = \sigma_{yz} = 0$.

2.3 Plastic properties

The plastic properties of a material describe its non-reversible deformation as a result of the applied force to the material. This means that when the applied force is removed, the material will not go back to its original state, and plastic deformation is thereby the opposite of elastic deformation. The transition from elastic to plastic behavior is described by the yield point of the material. Plastic properties are also used to describe and estimate the ductile behavior of a material, i.e. the material can endure the failure load beyond the failure point.

It is not straight forward to estimate static stiffness based on sound measurements, and plasticity is an important reason for this. This is because plasticity may influence the stiffness measured from static measurements, since such measurements inflict a high degree of deformation in a given direction of the sample. While during measurements with sound waves, the waves inflict small, periodical deformations to the sample, for which plastic deformation does not occur, and thereby the sound waves are not affected by the plasticity of the given sample.

(For examples of failure modes and interpretation of elastic parameters, see Appendix B.4 and B.5, respectively).

2.4 Static and dynamic measurements

Formation mechanical properties, elastic properties and plastic properties are normally derived from static measurements on core plugs in laboratories, but measurements on cuttings and cavings may as well be used to derive certain rock mechanical properties (Nes et al. 1996, Ringstad et al. 1998). Static measurements are time consuming and thereby not economical beneficial and as a result of this, theoretical models and correlations have been derived to take well logs in direct use for estimating rock mechanical properties, despite the fact that such methods are not straight forward. Such theoretical models take into use the formation principal stresses (often the vertical and the maximum/minimum horizontal stresses) as well as the pore pressure, which are a result of well measurements (e.g. well hydraulic fracture tests, caliper/image logs and density log).

Formation mechanical properties obtained from a single well may be applied to constitute a simple 1D model. But, various measurements from multiple wells may also be integrated through the use of geostatistics or alternatively through a 3D numerical model. This may define a 3D geomechanical model, or a "Mechanical Earth Model". Such models are the basis for almost any geomechanical analysis.

2.5 Summary

Geomechanical analyses are important when assessing the development of an oilfield. Such analyses include several different topics, both during exploration, development phase and during the production phase. These geomechanical analyses are in the need of basic rock mechanical properties, including formation mechanical properties, elastic properties and plastic properties. Such static properties can be determined from both static and dynamic measurements. However, the conversion from dynamic measurements to static parameters is not straight forward.

3. Rock Mechanical Data

3.1 Available data

The data samples included in this study are sandstone samples from the Norwegian shelf, which have been subjected to triaxial compression tests to determine their peak stress (failure stress) and elastic moduli such as Young's modulus and Poisson's ratio. These data samples are provided by Statoil and the tests have been performed by Weatherford Laboratories, including the petrophysical measurements which determine, amongst other, the porosity and the bulk volume of each sample. It is also essential to mention that these samples have been subjected to acoustic measurements.

This set of new, unpublished data from the Norwegian shelf will in this chapter be compared to already published work (presented in the article by Chang et al. 2006).

It should be noted that not all samples evaluated in this study are obtained from the same geological area, which may give way to differences in the petrophysical measurements. Chang et al. (2006) presented a summary of empirical equations, along with the data sets of several authors that have performed similar studies; relating unconfined compressive strength (UCS) to compressional transit time, Young's modulus or porosity. Lama and Vutukuri (1978) and Carmichael (1982) provided rock mechanical data from sedimentary rocks from locations all around the world. This data set reveal scatter which may be a result of the degree of compaction, as well as lithological and mineralogical effects. Kwasniewski (1989) also listed UCS and porosity data from various sandstones, and Wong et al. (1997) presented strength and other physical properties of several representative porous sandstones. From Texas, Jizba (1991) provided rock mechanical properties from sandstones, but despite the fact that this data set is obtained from one single borehole, some scatter can be seen (Figure 3-1 and Figure 3-2). And finally, the last data set from Bradford et al. (1998) comprise of laboratory test results on sandstones from the North Sea (Chang et al. 2006).

3.1.1 Compressional transit time

In Figure 3-1 the data sets obtained from the article by Chang et al. (2006), which are measured under dry conditions, are plotted together with the data set from the Norwegian shelf, which are saturated (with synthetic formation water) plug samples. The compressional transit time is directly measured for all data sets.

The figure show plot of measured unconfined compressive strength (UCS) against compressional transit time (Δt_p), and a clear scatter can be observed in the data collected from literature, while the unpublished results from the Norwegian shelf show a clear trend. It can also be seen that the samples from the study by Bradford et al. (1998) appear to follow the same trend as the unpublished data, and it is given that both of these data sets are obtained from the same geological area, i.e. the Norwegian shelf and the North Sea. Despite the scatter in Figure 3-1, the trend of decreasing UCS with increasing compressional transit time is evident.

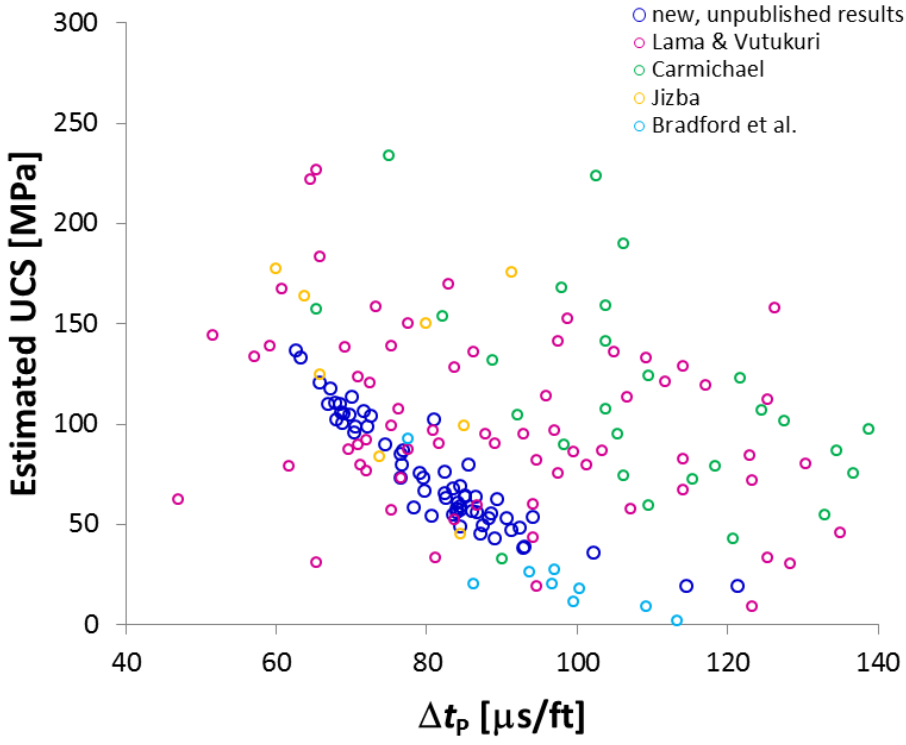

Figure 3-1. Available data- UCS as a function of Δt_p.

3.1.2 Young's modulus

Unconfined compressive strength (UCS) can also be evaluated as a function of Young's modulus (E). In Figure 3-2, plug samples obtained from the article by Chang et al. (2006) are plotted together with the unpublished data from the Norwegian shelf, as a function of Young's modulus. It can be seen that this correlation reveals a clear scatter, also for the unpublished data from the Norwegian shelf, which revealed a clear trend in Figure 3-1 when plotted as a function of Δt_p. Despite this scatter, it can be observed that UCS increases with increasing Young's modulus.

Young's modulus has been obtained through density and velocity measurements for the data sets found in the article by Chang et al. (2006), while for the plug samples which were subjected to static measurements performed by Weatherford Laboratories, Young's modulus was interpreted using linear regression in the 40 - 60 % range of the peak axial stress (see Appendix B.5).

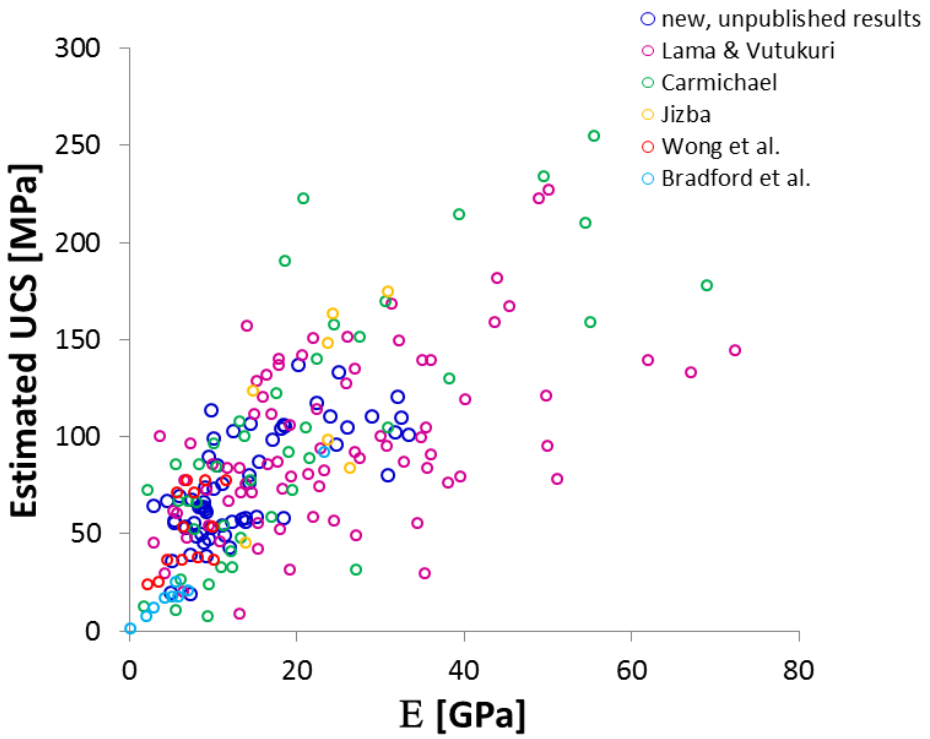

Figure 3-2. Available data- UCS as a function of E.

3.1.3 Porosity

As for Δt_p and Young's modulus, UCS can also be evaluated as a function of porosity (φ), and thereby the degree of compaction (as porosity decreases with increasing compaction). In Figure 3-3, the plug samples obtained from the article by Chang et al. (2006) and the plug samples obtained from the Norwegian shelf, are plotted as a function of φ. A more evident trend is observed for the porosity than for Δt_p and Young's modulus, as it can be seen that the UCS is decreasing for increasing porosity.

It can also be seen that the unpublished data set from the Norwegian shelf appear to give a linear trend as a function of porosity.

Porosity is derived from density measurements, where rock matrix and fluid densities are assumed, using;

$$\varphi = \frac{\rho_{ma} - \rho_b}{\rho_{ma} - \rho_f} \tag{3-1}$$

where φ is given in fractions, ρ_{ma} denotes the matrix density which is assumed to be equal to 2.64 g/cm^3 for sandstones, ρ_b denotes the bulk density which is given in g/cm^3 as mass divided by total volume, and ρ_f is given as the fluid density, and is assumed to be 0.8 g/cm^3 for oil.

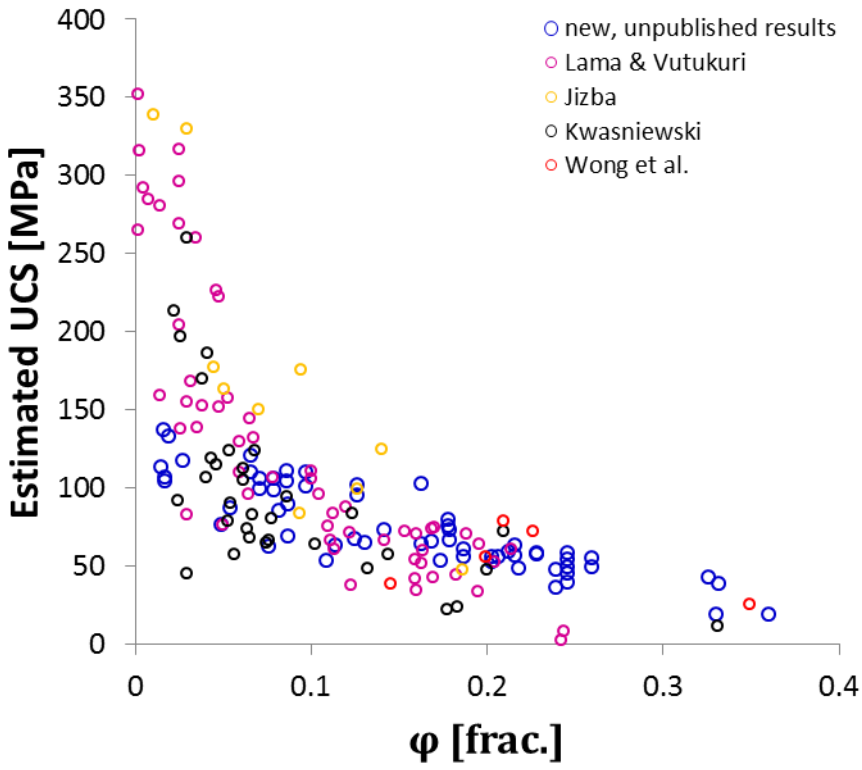

Figure 3-3. Available data- UCS as a function of φ.

3.2 Sample preparation

The unpublished sandstone samples from the Norwegian shelf have all been subjected to similar preparation by Weatherford Laboratories, by the instructions of Statoil. The plugs were supplied from a set of seal peals (directly drilled cores), where they were drilled parallel to the seal peal axis (i.e. vertically oriented). When drilling plugs that are to be used in rock mechanical tests, it is convenient to drill three plug samples at the exactly same depth. This method ensures homogeneous core samples, i.e. similar compaction and mineralogical composition, which gives the best correlation when constructing the Mohr-Coulomb failure envelope. After drilling, the plug end-surfaces were ground plane and parallel according to ISRM-standard (recommended tolerance in end parallelism is ± 0.0254 mm (Britt Rock Mechanics Lab)) to ensure that the plugs are perfectly attached to the pistons, as small errors may have great significance to the results. Further on the plug samples were adjusted to a length of approximately two times the diameter, and the length and diameter of each sample were measured to be used for the calculations of deformation and axial stress. In addition to that the weight of each sample was measured; digital images were used to describe the failure mechanism of each plug afterwards.

Cleaning is essential to remove any residual hydrocarbons which may affect the petrophysical measurements on the plugs, but the cleaning itself may also affect the rock mechanical measurements. This has resulted in several different trends regarding the question of cleaning the samples before rock mechanical testing. Some of the samples from the Norwegian shelf have been subjected to a standard soxhlet cleaning with toluene and methanol as solvents, before they were dried in a heat cabinet and further on the mercury (Hg) – bulk volume and helium (He) – porosity were measured. Other plugs were not cleaned, but instead subjected to circulation with paraffin oil, this to remove any possible residuals of the heaviest hydrocarbon compounds. This circulation is performed because some plugs are considered too fragile to be subjected to the standard cleaning procedure.

3.3 Triaxial compression test

The unpublished plug samples from the Norwegian shelf have been subjected to standard triaxial compression tests with different confining pressures. The plug samples were tested at drained conditions with SFW (synthetic formation water), and the sandstone samples provided by Statoil are also known to have been tested with a pore pressure of 0.5 MPa for the most recent studies and 1.0 MPa for studies performed several years ago. During such studies and tests, it is also standard procedure to measure the pore volume, this by connecting the pore pressure system to a volume gauge. Further on, the plug samples are loaded up to a predetermined hydrostatic load value, at a loading rate of about 1.0 MPa/minute. Then the plugs are unloaded hydrostatically to a low load value, before they are reloaded and subjected to hydrostatic consolidation for 30-60 minutes. Finally the samples are axially compressed with an axial deformation rate of normally 10 mStrain/hour, until clear failure are observed or 20 mStrain axial strain is obtained. Here it is as previously mentioned convenient to have three different confining pressures for three plugs obtained at the same depth, which will give a more accurate determination of the unconfined compressive strength using the Mohr-Coulomb failure envelope.

Acoustic measurements are essential to this study, as rock mechanical parameters are found to be a function of sonic transit time. For the unpublished samples from the Norwegian shelf, the acoustic velocities are measured in the axial direction of the sample, with either P-wave or S-wave transducers. P-wave transducers were common several years ago, before S-wave transducers became standard as it was discovered that the arrival of P-waves could also be seen with S-wave transducers. The arrival of the S-wave can sometimes be difficult to interpret, and therefore P-wave velocities are more frequently found in the data available and in literature generally. It is also essential that the signal/noise ratios are high enough to be able to interpret the wave traces to determine the velocities. The data included in this study for comparison, which are collected from literature (Chang et al. 2006), are confined to P-wave velocities.

As S-waves are to a very little extent affected by liquid effects (see section 4.2), as opposed to P-waves, a better correlation between S-waves and rock mechanical parameters are expected than between P-waves and rock mechanical parameters. The reason for this is the considerable, and unknown, variation the liquid effect has to P-waves.

3.4 Uniaxial compression test

The unconfined compressive strength (UCS) of a material is determined by the uniaxial compression test. This test has several similarities with the triaxial compression test (TCT), but also includes one major divagation from the TCT, namely zero confining pressure.

The uniaxial compression test requires a rigid loading frame for testing, and the triaxial cell (see Appendix B.1) is suited, and thereby often used, for this purpose.

The sample preparation for the uniaxial compression test includes cutting the plug samples to the specified length, and the ends are ground plane and parallel, as for the TCT. It is also possible to conduct uniaxial compression tests on different plugs drilled at different directions in a core to capture strength anisotropy (directional dependent) in the material. In the uniaxial compression test, the specimen is shortened by the load and is normally expanding laterally as a result of the Poisson effect (see section 2.2.2).

In Figure 3-4, a typical result from the uniaxial compression test is showed, and several important concepts are defined (Fjær et al. 1992):

- The elastic region defines that the specimen will return to its original state after the stress is released.
- Hardening region is where the sample undergoes plastic deformation with increasing ability to sustain load.
- Softening region is where the specimen's ability to withstand stress decreases as deformation increases.

For more failure modes, see Appendix B.4

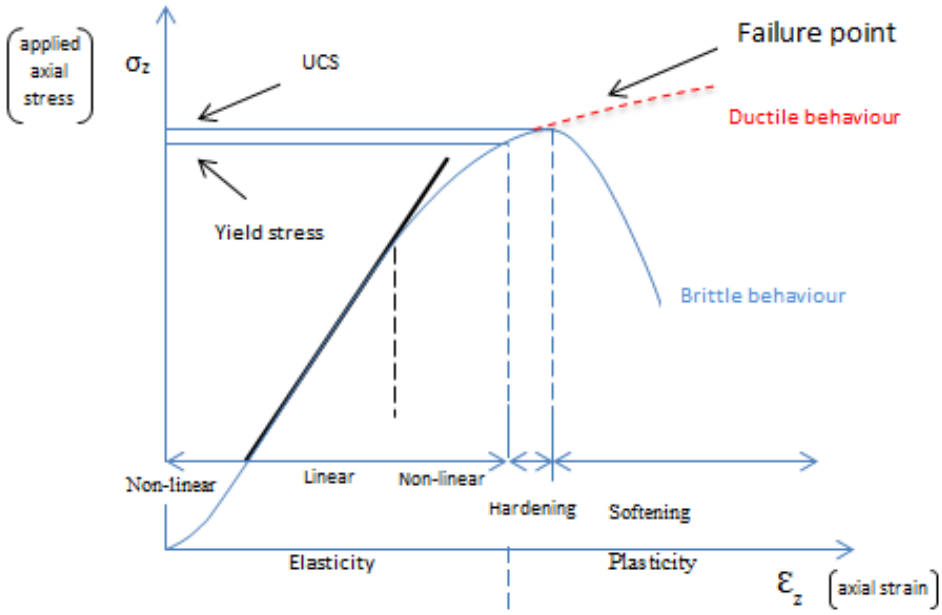

Figure 3-4. Stress vs deformation in a uniaxial compression test. Edited from Fjær et al. (1992).

3.5 Evaluation of data samples

Plug samples from the Norwegian shelf have been evaluated individually by Weatherford Laboratories, and two of the plug samples were excluded from further testing during the test procedure due to different reasons:

- One plug has been removed due to the fact that its lithological description show heterogeneity on this plug in particular, while other plugs from the same seal peal show homogeneity. Observations on this plug after testing show that the measurements are most likely affected by this heterogeneity, and thereby the results are interpreted as not valid.
- The second plug in question was removed due to the reason that it showed a special fracture phenomenon where the radial deformation after failure is positive (reduction of diameter). The measured peak stress on this plug is significant lower than those on other plugs from the same seal peal.

In this study, an upper limit for Poisson's ratio has not been set to 0.5, which is the theoretical upper limit for isotropic, linear elastic materials. Since rocks may behave plastically, values greater than 0.5 have been included as well.

3.6 Summary

A set of plug samples from the Norwegian shelf provided by Statoil and tested by Weatherford Laboratories, along with plug samples from locations all over the world found in the article by Chang et al. (2006), have been subjected to triaxial compression tests to determine their elastic moduli. The cleaning and handling of the plug samples from the Norwegian shelf have been taken into consideration, and the unconfined compressive strength (UCS) of each sample has been plotted as a function of compressional transit time (Δt_p), Young's modulus (E) and porosity (φ).

From the available data, it is found that the overall trend is decreasing UCS with increasing Δt_p, increasing UCS with increasing E, and decreasing UCS with increasing φ.

3.7 Discussion

It was also found that the unpublished data from the Norwegian shelf followed these overall trends, but showed a higher degree of consistency related to the given parameter than the data obtained from literature. This may be related to the fact that the unpublished data from the Norwegian shelf are much more restricted regarded to area than the other data collected from literature. However, some of the data sets collected from literature are limited to one single well, so the consistency of the compaction and mineralogical composition may also influence the results.

4. Static – dynamic correlations

As mentioned earlier, rock mechanical properties can be derived from static measurements. This is however time consuming and thereby related to economic aspects, as rock samples need to be transported to a laboratory.

The work performed in this thesis will try to establish a relation between acoustic properties and elastic properties and rock compressive strength for sandstone, based on acoustic and static measurements from plug samples provided by Statoil obtained from the Norwegian shelf. By comparing static and dynamic measurements from laboratory tests, a simple empirical model is given to determine Young's modulus, Poisson's ratio and unconfined compressive strength (UCS) from the use of sonic transit time, both compressional and shear. The obtained model will then be compared and discussed with already published relations, these from locations all around the world.

4.1 P-waves

Compressional wave, longitudinal wave, primary wave and P-wave are names describing the same type of wave. P-wave includes a periodic compression of the material it travel through, and are named primary waves after the studies of earthquakes (Fjær et al. 1992). This periodic compression implies that the P-wave will vibrate in the same direction as the direction the wave travel in, or more thoroughly explained; each component in the medium will oscillate in the same direction as the motion of the wave. Compressional waves can be illustrated by the use of a spring, as can be seen in Figure 4-1. The components of the medium vibrate back and forth in the direction of travel. In the compressions the particles are pushed together, and in the rarefactions they are pulled apart.

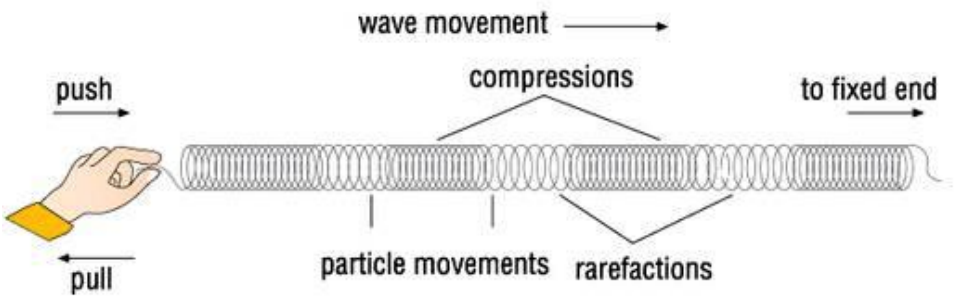

Figure 4-1. Illustration of compressional wave (after www.talktalk.co.uk).

4.2 S-waves

As for P-waves, there are several names for describing the second type of body waves, namely the transversal wave, shear wave, secondary wave or S-wave. S-wave includes a periodic shear of the material it travels through, and thereby S-waves cannot travel through fluids since they do not exhibit shear stiffness, i.e. S-waves are in a very little extent influenced by the liquid within the rock. For an S-wave the particles of the solid move in the orthogonal direction compared to a P-wave, as the components in the material moves perpendicular to the direction of the wave. Shear waves are best illustrated by the use of a rope, as can be seen in Figure 4-2. The particles oscillate at right angles to the direction of wave.

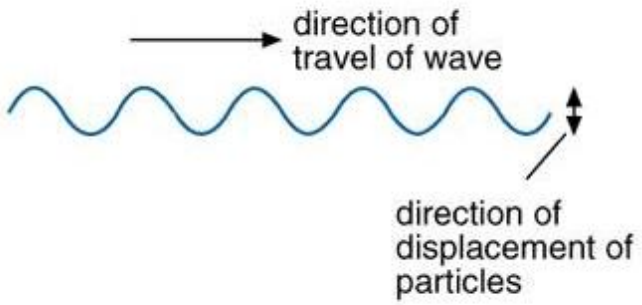

Figure 4-2. Illustration of shear wave (after www.talktalk.co.uk).

4.3 Sonic transit time

Sonic transit time can be divided into compressive and shear transit time, describing the propagation of the wave (see section 4.1 and 4.2). Transit time, in this relation, is given as the time it takes for a wave to travel from the source to the receiver, and is proportional with the given distance. Compressional and shear transit time is denoted Δt_p and Δt_s respectively, and is related to compressional and shear wave velocity by

$$V = \frac{304878}{\Delta t} \tag{4-1}$$

where Δt is given in μs/ft and V in m/s.

Sonic transit time is also directly related to stiffness, as is shown below;

$$x_p = \rho \cdot v_p^2 = \rho(\Delta t_p)^{-2} \tag{4-2}$$

$$x_s = \rho \cdot v_s^2 = \rho(\Delta t_s)^{-2} \tag{4-3}$$

where x_p is the uniaxial compaction modulus, x_s is the shear modulus, ρ is the density, and v_p and v_s are the compressional and shear velocity, respectively.

The uniaxial compaction modulus and the shear modulus are dynamic stiffnesses (i.e. they are obtained from acoustic velocities and densities). For sedimentary rocks, the dynamic stiffnesses may differ significantly from their static (obtained from static stress and strain measurements) counterparts, although they in theory should be equal for an undrained (or dry), linear elastic material. This difference in static and dynamic moduli is mainly a result of two main features; cracks and pore fluid. In the static case, closed cracks may slide against each other when the strain is sufficiently high, and thereby reduce the stiffness of the rock. While in the dynamic case, the amplitude of the strain is often much lower and sliding may not be an effect. Regarding the effect of pore fluid, both fluid flow in pores and local flow between cracks or narrow pore channels, may increase the measured acoustic velocity. Despite this fact, some degree of correlation between dynamic and static stiffnesses is expected.

A link between dynamic stiffness and strength is also to be expected, since both strength and stiffness depend largely on the amount of solid material present in the rock, or – equivalently – they both depend on the porosity. However, the geometrical distribution of the solid material in terms of pore shape, degree of cementation etc. is also important, and this distribution affects stiffness and strength differently. Thus, some correlation between strength and sonic data, and between static stiffness and sonic data, is to be expected, but these correlations may not be very strong.

4.4 Empirical equations from literature

There are numerous empirical equations found in literature that relates unconfined compressive strength (UCS) to sonic transit time, elastic constants and porosity. The results from the study performed here will be compared and evaluated against some of the empirical relations found in literature, several of them mentioned in the article by Chang et al. (2006).

McNally (1987) developed two separate empirical equations based on the region the samples were collected from. A set of data from fine grained sandstone from the Bowen Basin in Australia were collected. The data included both consolidated and unconsolidated sandstones, thereby including all porosity ranges. This resulted in a relation (Eq. (4-4)) that included compressional transit time (Δt_p) for estimation of the UCS.

$$UCS = 1200 \cdot e^{(-0.036 \Delta t_p)} \tag{4-4}$$

where UCS is given in MPa and Δt_p in μs/ft.

A second set of data was collected from the Gulf Coast, USA. These samples are limited to weak and unconsolidated sandstones, and are also expressed in terms of Δt_p;

$$UCS = 1.4138 \cdot 10^7 \Delta t_p^{-3} \tag{4-5}$$

where UCS is given in MPa and Δt_p in μs/ft.

Raaen et al. (1996) presented an equation relating UCS to Δt_p on sandstone samples obtained (mostly) from the North Sea. The sandstone samples were regarded to be of weak material, and Eq. (4-6) was initially developed to include the confining pressure of the test procedure. However, setting the confining pressure equal to zero, one obtains the given equation for UCS;

$$UCS = 140 - 2.1\Delta t_p + 0.0083\Delta t_p^2 \tag{4-6}$$

where UCS is given in MPa and Δt_p in μs/ft.

For a range of igneous, sedimentary and metamorphic rocks, Sharma and Sing (2008) presented a linear equation (Eq. (4-7)) that gives a correlation between the UCS and the P-wave velocity (V_p) for the given material.

$$UCS = 0.0642V_p - 117.99 \tag{4-7}$$

where UCS is given in MPa and V_p in m/s.

And from the region Thuringia in Germany, Freyburg (1972) developed a linear empirical equation (Eq. (4-8)), relating V_p to the UCS of sandstone samples.

$$UCS = 0.035V_p - 31.5 \tag{4-8}$$

where UCS is given in MPa and V_p in m/s.

From the McArthur River Field at Cook Inlet, Alaska, Moos et al. (1999) developed an empirical equation (Eq. (4-9)) that predicted the UCS for the given material, depending both on the density (ρ) and the P-wave velocity. These rock samples from the Cook Inlet were described as coarse grained sandstones, and also included some conglomerates.

$$UCS = 1.745 \cdot 10^{-9} \rho V_p^2 - 21 \tag{4-9}$$

where UCS is given in MPa, V_p in m/s and ρ in g/cm^3.

Chang et al. (2006) presented as previously mentioned a summary of empirical equations for sandstones (as well as for shales and limestones and dolomites). The final two equations that will be compared to the result from this study are given below, and are based on sandstone samples from Australia (Eq. (4-10)) and the Gulf of Mexico (Eq. (4-11)) respectively. These are unpublished empirical relations obtained from the article by Chang et al. (2006).

$$UCS = 42.1 \cdot e^{(1.9 \cdot 10^{-11} \rho V_p^2)} \tag{4-10}$$

$$UCS = 3.87 \cdot e^{(1.14 \cdot 10^{-10} \rho V_p^2)} \tag{4-11}$$

where UCS is given in MPa, V_p in m/s and ρ in g/cm^3.

In order to compare these empirical equations with each other, only depending on the compressional transit time (Δt_p), a constant value of density (ρ) is set to 2.3 g/cm^3 as this is regarded as a reasonable average value for sandstone (Chang et al. 2006).

4.5 Summary

Rock mechanical properties may be derived from both static and dynamic measurements, and the ability to determine elastic properties and compressive strength from dynamic measurements is beneficial both regarded to time and economics. Dynamic measurements are related to acoustic velocities and densities, and may differ significantly from static measurements that are related to stress and strain measurements, although they in theory should be equal for an undrained, linear elastic material.

A set of empirical equations for sandstones, derived from locations all over the world, have been evaluated and will be compared against the empirical relations obtained in this study.

5. Calculations

The plug samples available from the Norwegian shelf have been subjected to triaxial compression tests performed by Weatherford Laboratories. The plugs were tested at different confining pressures. Therefore, to be able to compare the test result on these plug samples, models as functions of confining pressure needed to be established for the various parameters.

5.1 Data values

The results from the triaxial compression tests performed on the samples from the Norwegian shelf are given in Table 1 below. These data values are given with permission from Statoil.

Table 1. Main results of static and dynamic measurements on core samples from the Norwegian shelf (performed by Weatherford Laboratories).

ID	φ [frac.]	ρ_b [g/cm^3]	ρ_{ma} [g/cm^3]	σ_c [MPa]	p_p [MPa]	$\sigma_{c,net}$ [MPa]	E [GPa]	ν [-]	σ_{max} [MPa]	UCS [MPa]	Vp [m/s]	Vs [m/s]
1	0.332	2.03		3.0	1.0	2.0	9.2	0.19	40.9	34.5	3280	2090
2	0.207	2.26		3.0	1.0	2.0	14.0	0.13	70.2	60.6	3515	2125
3	0.228	2.22		3.0	1.0	2.0	13.5	0.22	73.9	71.0	3610	1990
4	0.228	2.22		7.0	1.0	6.0	18.5	0.34	99.1	60.6	3630	2260
5	0.212	2.25		7.0	1.0	6.0	15.3	0.41	88.6	71.0	3610	2255
6	0.326	2.04		13.0	1.0	12.0	12.0	0.24	72.8	34.5	3420	2180
7	0.126	2.38	2.66	6.0	1.0	5.0	24.8	0.19	116.9	64.6	4330	
8	0.097	2.37	2.68	6.0	1.0	5.0	33.5	0.2	130.9	78.6	4430	
9	0.079	2.43	2.63	6.0	1.0	5.0	17.2	0.19	108.8	3.9	4320	
10	0.179	2.22	2.64	6.0	1.0	5.0	4.6	0.25	46.7	19.6	3820	
11	0.178	2.45	2.73	6.0	1.0	5.0	11.1	0.39	66.8	19.4	3850	
12	0.216	2.26	2.68	6.0	1.0	5.0	5.5	0.14	39.8	16.0	3540	
13	0.086	2.52	2.67	6.0	1.0	5.0	26.1	0.21	136.3	46.0	4370	
14	0.017	2.66	2.68	6.0	1.0	5.0	18.2	0.32	75.7	43.2	4200	
15	0.066	2.54	2.69	6.0	1.0	5.0	24.0	0.29	128.1	83.9	4450	
16	0.187	2.33	2.68	6.0	1.0	5.0	5.5	0.35	45.6	17.5	3440	
17	0.203	2.23	2.66	6.0	1.0	5.0	9.8	0.16	63.0	27.0	3450	
18	0.218	2.28	2.73	6.0	1.0	5.0	8.1	0.21	42.9	14.0	3300	
19	0.163	2.41	2.75	6.0	1.0	5.0	8.7	0.28	56.1	23.8	3580	
20	0.071	2.55	2.69	6.0	1.0	5.0	10.1	0.34	69.1	28.8	4220	
21	0.126	2.37	2.66	11.0	1.0	10.0	31.8	0.2	160.6	73.1	4480	
22	0.097	2.45	2.68	11.0	1.0	10.0	32.5	0.31	150.5	111.0	4550	
23	0.079	2.48	2.63	11.0	1.0	10.0	18.6	0.34	133.4	4.9	4420	

24	0.179	2.23	2.64	11.0	1.0	10.0	10.1	0.21	68.2	23.8	3980	
25	0.178	2.43	2.73	11.0	1.0	10.0	14.4	0.36	92.2	41.4	3970	
26	0.216	2.31	2.68	11.0	1.0	10.0	8.9	0.16	61.1	18.5	3690	
27	0.086	2.52	2.67	11.0	1.0	10.0	29.0	0.52	174.5	98.0	4490	
28	0.017	2.66	2.68	11.0	1.0	10.0	14.6	0.16	68.1	43.2	4250	
29	0.066	2.57	2.69	11.0	1.0	10.0	32.1	0.41	180.9	75.3	4630	
30	0.187	2.28	2.68	11.0	1.0	10.0	9.2	0.26	70.7	20.5	3620	
31	0.203	2.21	2.66	11.0	1.0	10.0	12.3	0.06	84.9	41.1	3630	
32		2.54		11.0	1.0	10.0	30.9	0.11	185.3	91.4	3560	
33	0.163	2.45	2.75	11.0	1.0	10.0	12.5	0.08	80.5	31.6	3760	
34	0.071	2.56	2.69	11.0	1.0	10.0	18.5	0.22	109.4	28.8	4440	
35	0.015	2.7	2.71	11.0	1.0	10.0	9.9	0.31	74.8	30.2	4350	
36	0.027	2.59		6.0	1.0	5.0	22.5	0.26	83.50	66.80	4530	
37	0.049	2.55		6.0	1.0	5.0	14.4	0.31	61.20	56.00	3700	
38	0.087	2.48		6.0	1.0	5.0	6.1	0.28	46.90	27.70	3610	
39	0.109	2.44		6.0	1.0	5.0	6.7	0.2	45.80	28.90	3240	
40	0.174	2.32		6.0	1.0	5.0	6.7	0.29	44.90	31.20	3360	
41	0.019	2.59		21.0	1.0	20.0	25.1	0.16	145.1	108.5	4810	
42	0.082	2.49		21.0	1.0	20.0	10.6	0.33	100.7	58.0	3980	
43	0.114	2.43		21.0	1.0	20.0	8.4	0.25	89.8	53.2	3520	
44	0.168	2.33		21.0	1.0	20.0	9.0	0.23	93.4	43.5	3700	
45	0.016	2.61		31.0	1.0	30.0	20.2	0.22	163.5	108.5	4860	
46	0.054	2.54		31.0	1.0	30.0	15.6	0.37	111.8		3960	
47	0.087	2.48		31.0	1.0	30.0	9.5	0.41	122.0	58.0	4090	
48	0.125	2.41		31.0	1.0	30.0	7.5	0.27	108.1	53.2	3650	
49	0.141	2.38		31.0	1.0	30.0	9.1	0.27	118.3	43.5	3830	
50	0.130	2.4		3.0	1.0	2.0	2.9	0.08	28.2	26.8	3580	
51	0.239	2.2		6.0	1.0	5.0	5.1	0.36	42.0	26.8	2980	
52	0.076	2.5		11.0	1.0	10.0	9.1	0.17	59.8	26.8	3410	
53	0.239	2.2		21.0	1.0	20.0	9.5	0.26	91.8	26.8	3340	
54	0.246	1.95	2.65	2.5	0.5	2.0	7.4	0.28	27.3	25.0	3279	1848
55	0.246	1.95	2.65	5.5	0.5	5.0	8.9	0.11	42.3	25.0	3497	2028
56	0.246	1.95	2.65	10.5	0.5	10.0	11.4	0.21	62.2	25.0	3610	2114
57	0.246	1.95	2.65	20.5	0.5	20.0	11.1	0.23	86.1	25.0	3774	2237
58	0.246	1.95	2.65	40.5	0.5	40.0	14.0	0.06	89.7	25.0	3891	2320
59	0.33	2.08	2.67	10.5	0.5	10.0	7.4	0.28	49.3	10.9	2513	1481
60	0.36	1.93	2.67	12.5	0.5	12.0	5.0	0.13	45.2	10.9	2660	1490
61	0.26	2.13	2.63	12.5	0.5	12.0	8.7	0.27	73.9	20.3	3484	1894
62	0.26	2.13	2.63	12.5	0.5	12.0	7.8	0.19	73.2	20.0	3650	2083

where

φ	=	porosity [fraction]
ρ_b	=	bulk density [g/cm^3]
ρ_{ma}	=	matrix density [g/cm^3]
σ_c	=	confining pressure [MPa]
p_p	=	pore pressure [MPa]
$\sigma_{c,net}$	=	net confining pressure [MPa] ($\sigma_c - p_p$)
E	=	Young's modulus [GPa]
v	=	Poisson's ratio [-]
σ_{max}	=	peak stress [MPa]
UCS	=	estimated UCS [MPa] (from TCT and Mohr-Coulomb)
Vp	=	P-wave velocity [m/s]
Vs	=	S-wave velocity [m/s]

5.2 Empirical model

A number of series expansions have been performed in order to determine the appropriate elastic properties and compressive strength of a material as a function of confining pressure, density, sonic transit time and porosity. This was performed by a series of trials and errors, with the aim of developing a model that gave the least error between the modeled parameter and the resulting true parameter for each plug sample (see Eq. 5-4). The method of least squares (Miller 2006) was used to estimate the given parameters and to find the corresponding residuals.

5.3 Unconfined compressive strength

As unconfined compressive strength (UCS) tests are not as common as the standard triaxial compression tests (TCT), the Mohr-Coulomb criterion is frequently used to derive the UCS, as the Mohr-Coulomb criterion is based on the assumption that the critical shear stress is a linear function of the normal stress, where the intercept with the y-axis is known as the inherent shear strength of the material, which is closely related to the UCS of the same material (see Eq. (5-1)).

$$\tau_{\max} = S_0 + \mu \cdot \sigma' \tag{5-1}$$

where σ_{max} is the critical shear stress, S_0 is the inherent shear strength of the material, μ is the coefficient of internal friction and σ' is the normal stress acting over the failure plane (Fjær e al. 1992).

For the work performed in this study, a model based on the Mohr-Coulomb criterion (Eq. (5-2)) was chosen.

$$\sigma_{\max} = A + \sigma_c \cdot B \tag{5-2}$$

where σ_{max} is the peak stress, A represent the UCS, σ_c is the confining pressure and B represent the coefficient of internal friction. A and B are assumed to be function of porosity and the respective dynamic stiffness (see section 4.3).

From the available data, e.g. porosity and dynamic stiffness, and the assumption that there is a connection between stiffness and strength, expressions for A and B were estimated. The connection between stiffness and strength may vary with varying porosity, and this was also taken into consideration in the expressions for A and B.

$$\begin{aligned} A &= a + (b \cdot \varphi) + (c \cdot x) \\ B &= d + (e \cdot \varphi) + (f \cdot x) \end{aligned} \tag{5-3}$$

where the porosity (φ) is given in fractions and x represents the corresponding dynamic stiffness (compressional (x_p) or shear (x_s)) given in $g.cm^{-3}.cm^2.\mu s^{-2}$. Appropriate values for the parameters a, b, c, d, e and f were found, this by setting the sum of residuals (see Eq. (5-4)) between the modeled peak stress and the measured peak stress to be as small as possible.

$$\sum (\text{peak stress}_{\text{modeled}} - \text{peak stress}_{\text{measured}})^2 \tag{5-4}$$

Parameters (a-f) that showed minimal influence on the results were set equal to zero to minimize the number of free parameters.

5.3.1 P-waves

By the use of the least squares method, the following values of the parameters a [MPa], b [MPa], c [-], d [-], e [-] and f [1/Pa] were found:

$$\begin{aligned} a &= 0 \\ b &= -31.06 \\ c &= 222.5 \\ d &= 1.32 \\ e &= 0.77 \\ f &= -0.40 \end{aligned} \tag{5-5}$$

Resulting in the following expressions for A [MPa] and B [-]:

$$\begin{aligned} A &= -31.06 \cdot \varphi + 222.5 \cdot x_p \\ B &= 1.32 + 0.77 \cdot \varphi - 0.40 \cdot x_p \end{aligned} \tag{5-6}$$

where φ is given in fractions and $x_p = \rho(\Delta t_p)^{-2}$ in $g.cm^{-3}.cm^2.\mu s^{-2}$.

The measured peak stress and the modeled peak stress, by the use of Eq. (5-2) and Eq. (5-6), are plotted in Figure 5-1. The coefficient of determination R_1^2 is equal to 0.6102.

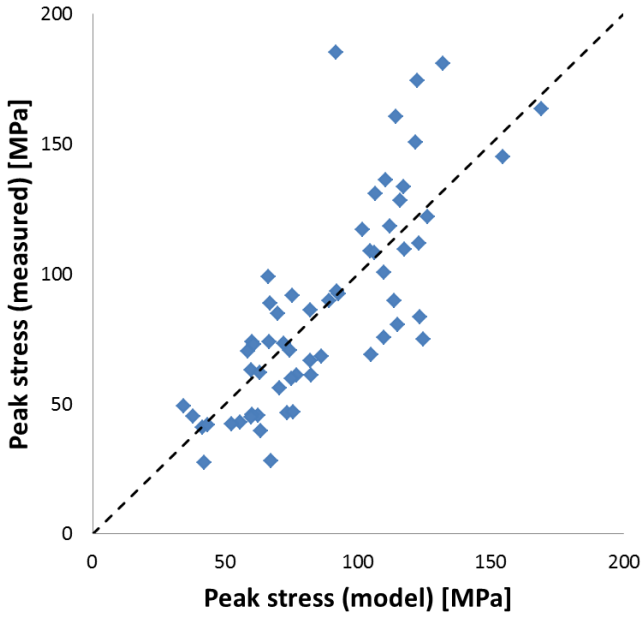

Figure 5-1. Measured peak stress vs modeled peak stress (P-waves).

Based on the calibrated strength in Eq. (5-2) and on the expressions in Eq. (5-6), it is now possible to estimate the UCS for each plug sample. This is done by setting the confining pressure equal to zero and plotting the result as a function of compressional transit time (Δt_p). The result may be seen in Figure 5-2. The trendline plotted in Figure 5-2 is found by the best fit of an exponential function, and is given as

$$UCS = 1198.2 \cdot e^{-0.035 \Delta t_P} \tag{5-7}$$

where UCS is given in MPa and Δt_p in μs/ft, with the resulting coefficient of determination R_2^2 equal to 0.9133.

As an indication of the goodness of fit for the obtained empirical equation (Eq. (5-7)), the product of the coefficients of determination for the two steps involved is determined, giving $R_1^2 R_2^2$ = 0.56.

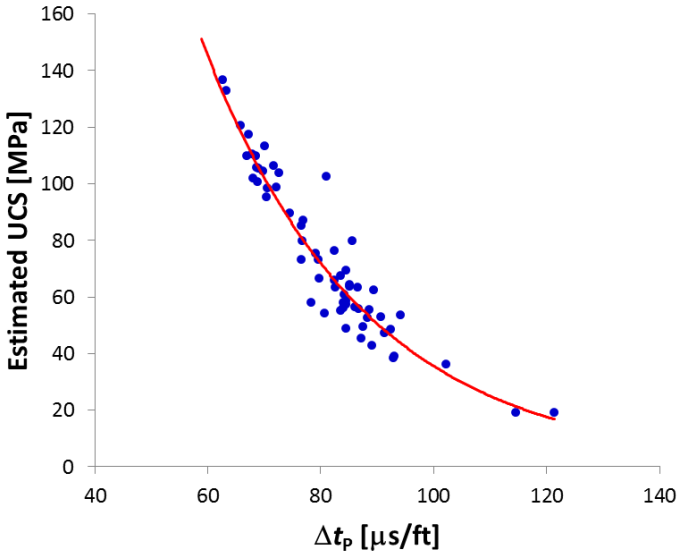

Figure 5-2. Estimated UCS vs Δt_p.

5.3.2 S-waves

The same procedure is used when estimating peak stress for shear waves, with Eq. (5-2) and the expressions for A and B in Eq. (5-3). However, separate values for the parameters a [MPa], b [MPa], c [-], d [-], e [-] and f [1/Pa] were found;

$$\begin{aligned} a &= -7.97 \\ b &= -133.34 \\ c &= 397.65 \\ d &= -7.38 \\ e &= 31.88 \\ f &= 0 \end{aligned} \tag{5-8}$$

Giving;

$$\begin{aligned} A &= -7.97 - 133.34 \cdot \varphi + 397.65 \cdot x_s \\ B &= -7.38 + 31.9 \cdot \varphi \end{aligned} \tag{5-9}$$

where φ is given in fractions, $x_s = \rho(\Delta t_p)^{-2}$ in $g.cm^{-3}.cm^2.\mu s^{-2}$, A in MPa and B is unit less.

The modeled peak stress for shear waves are plotted against measured peak stress in Figure 5-3, giving a fairly well estimation with a corresponding R_1^2 of 0.7397. The estimated UCS plotted as a function of shear transit time (Δt_s) is found in Figure 5-4, where the corresponding best fit is given as;

$$UCS = 425.68 \cdot e^{-0.015 \Delta t_S} \tag{5-10}$$

where UCS is given in MPa and Δt_s in μs/ft, and R_2^2 = 0.8567.

The product of the coefficients of determination is thereby $R_1^2 R_2^2$ =0.63.

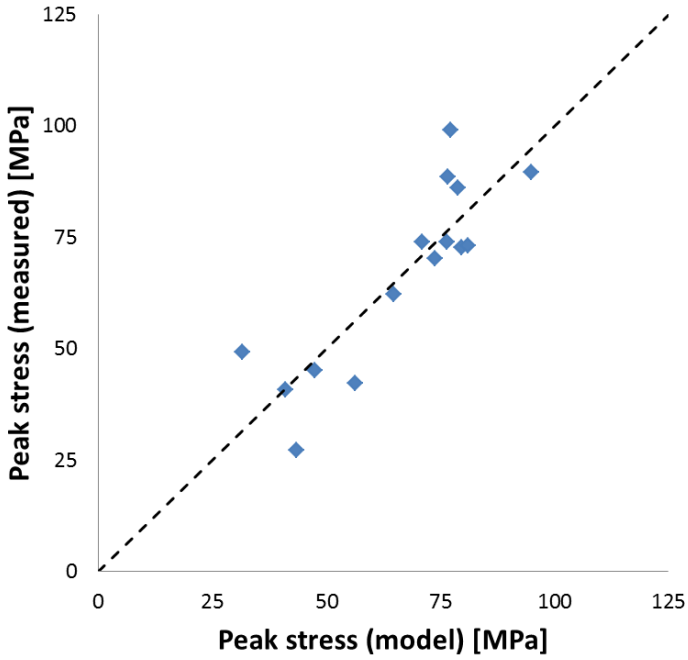

Figure 5-3. Measured peak stress vs modeled peak stress (S-waves).

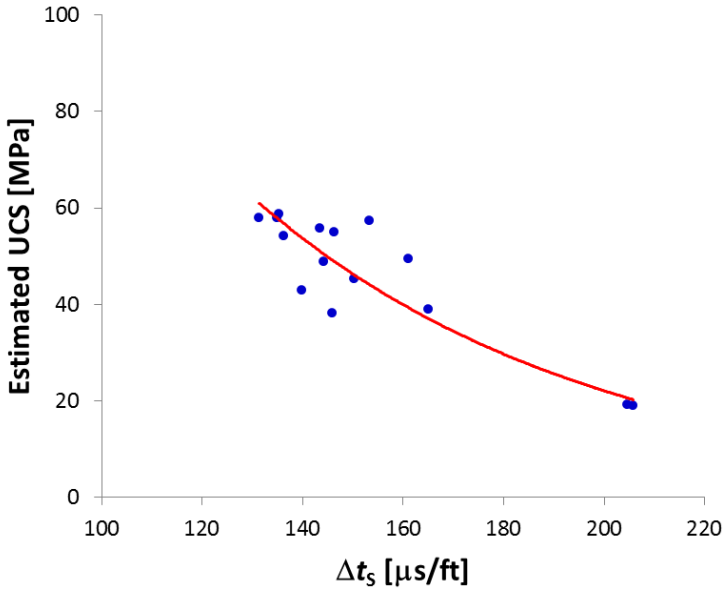

Figure 5-4. Estimated UCS vs Δt_s.

5.4 Young's modulus

When estimating the Young's modulus (E) of a sample, it is important to take into consideration the confining pressure applied to the given plug sample, as this may have great effect on the stiffness of the sample. When estimating the Young's modulus for the plug samples obtained from the Norwegian shelf, a standard series expansion was performed. Two separate parameters were used, namely the confining pressure (σ_c) and the dynamic stiffness (x) (compressional (x_p) or shear (x_s)), and through trials and errors the appropriate model was found for Young's modulus;

$$E = a + b \cdot x + c \cdot \sigma_c + d \cdot x^2 + e \cdot \sigma_c^2 + f \cdot x \cdot \sigma_c \qquad (5\text{-}11)$$

where E is given in GPa, x in $g.cm^{-3}.cm^2.\mu s^{-2}$ and σ_c in MPa.

5.4.1 P-waves

Through the use of the least squares method, the following values for the parameters a [GPa], b [-], c [-], d [1/Pa], e [1/Pa] and f [1/Pa] were found:

$$\begin{aligned} a &= 7.21 \\ b &= -17.68 \\ c &= 0.129 \\ d &= 115.28 \\ e &= 0.0074 \\ f &= -1.57 \end{aligned} \qquad (5\text{-}12)$$

The modeled Young's modulus is plotted against the measured Young's modulus in Figure 5-5. The resulting coefficient of determination is R_1^2 =0.5475.

Figure 5-6 gives the estimated Young's modulus plotted as a function of compressional transit time (Δt_p), where σ_c is equal to zero and the trendline is given as;

$$E = 9925.85 \cdot (\Delta t_p - 38.09)^{-1.73} \quad (5\text{-}13)$$

where E is given in GPa and Δt_p in μs/ft, and the resulting R_2^2 is equal to 0.9282, giving $R_1^2 R_2^2$ =0.51.

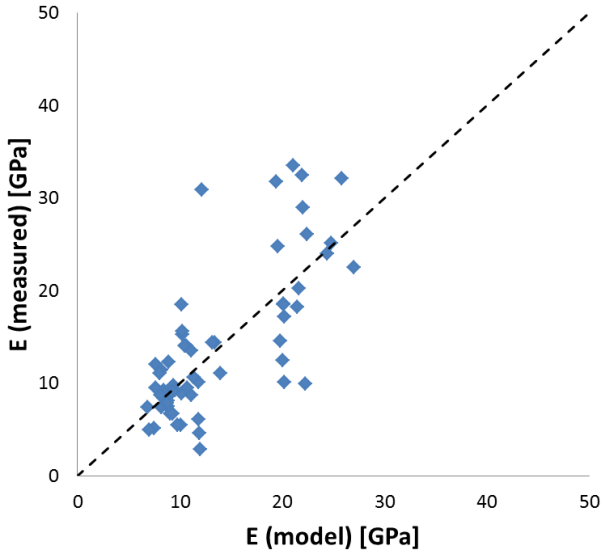

Figure 5-5. Measured E vs modeled E (P-waves).

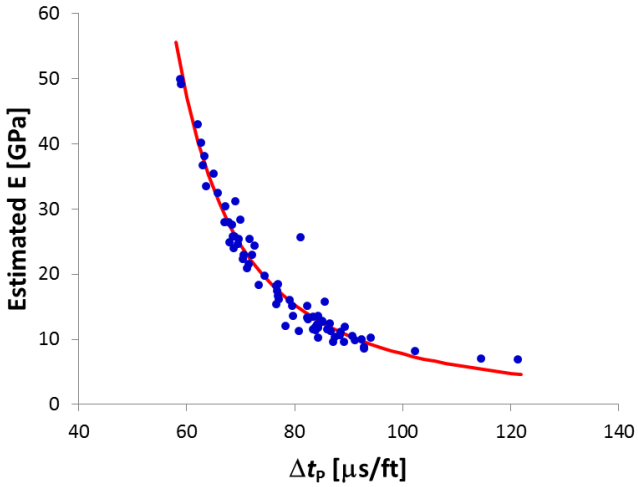

Figure 5-6. Estimated E at zero confining pressure vs Δt_p.

5.4.2 S-waves

For S-waves, the following values for the parameters a [GPa], b [-], c [-], d [1/Pa], e [1/Pa] and f [1/Pa] were found;

$$\begin{aligned} a &= 3.84 \\ b &= 0 \\ c &= 0 \\ d &= 1061.29 \\ e &= 0.0062 \\ f &= -2.73 \end{aligned} \tag{5-14}$$

The result is compared against the measured Young's modulus in Figure 5-7, with a coefficient of determination R_1^2 of 0.8173.

In Figure 5-8, Young's modulus, with σ_c = 0, is plotted as a function of shear transit time (Δt_s). The best fit (Eq. (5-15)) gives R_2^2 = 0.8901, and $R_1^2 R_2^2$ =0.73.

$$E = 170.41 \cdot (\Delta t_s - 107.35)^{-0.716} \tag{5-15}$$

where E is given in GPa and Δt_s in μs/ft.

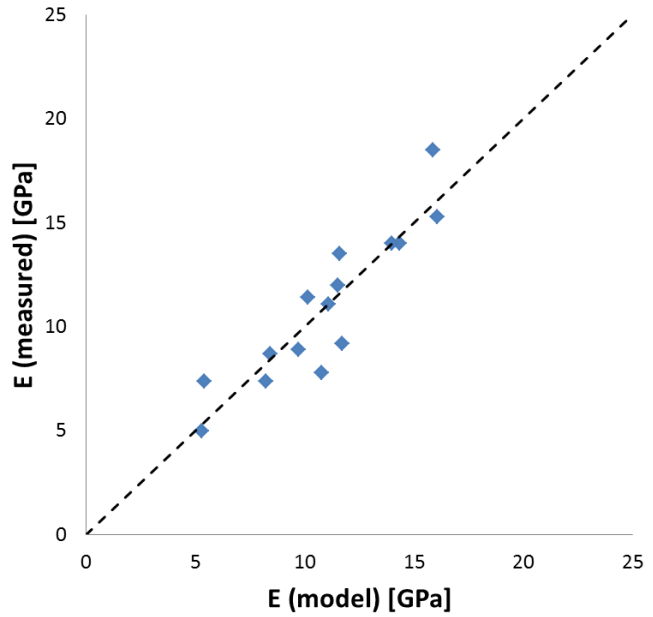

Figure 5-7. Measured E vs modeled E (S-waves).

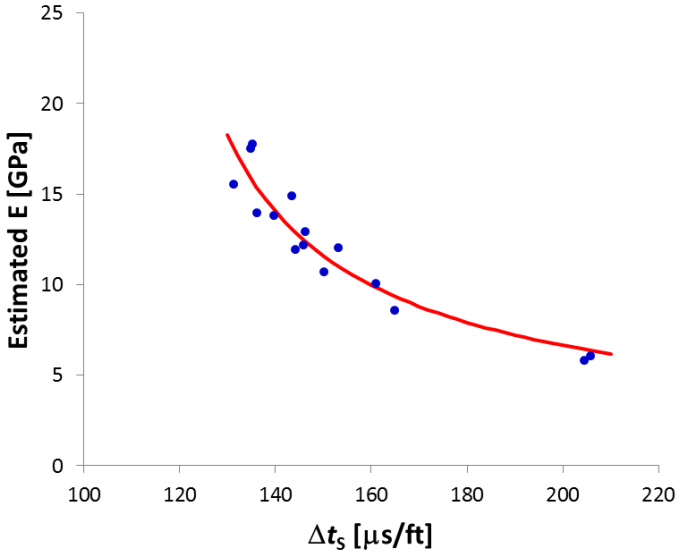

Figure 5-8. Estimated E at zero confining pressure vs Δt_s.

5.5 Poisson's ratio

Finally, a model for determining the Poisson's ratio (v) by the use of confining pressure (σ_c) and dynamic stiffness (x) were derived. As for Young's modulus, series expansion was performed, resulting in two separate models for dynamic compressional stiffness and dynamic shear stiffness, respectively.

The obtained model for Poisson's ratio is given below;

$$\nu = a + b \cdot x + c \cdot \sigma_c + d \cdot x^2 + e \cdot \sigma_c^2 + f \cdot x \cdot \sigma_c \qquad (5\text{-}16)$$

where x is given in $g.cm^{-3}.cm^2.\mu s^{-2}$ and σ_c in MPa.

5.5.1 P-waves

The given values were found for the parameters a [-], b [1/Pa], c [1/Pa], d [$1/Pa^2$], e [$1/Pa^2$] and f [$1/Pa^2$] by the least squares method;

$$\begin{aligned} a &= 0.0089 \\ b &= 0.8107 \\ c &= 0.0152 \\ d &= 0 \\ e &= -0.0002 \\ f &= -0.0407 \end{aligned} \qquad (5\text{-}17)$$

The plot of modeled Poisson's ratio versus measured Poisson's ratio is shown in Figure 5-9. As can be seen from the figure, there is no match between the modeled and the measured Poisson's ratio, as confirmed by the coefficient of determination R_1^2 which is equal to 0.02. Due to this, a trendline for Poisson's ratio versus compressional transit time has not been found.

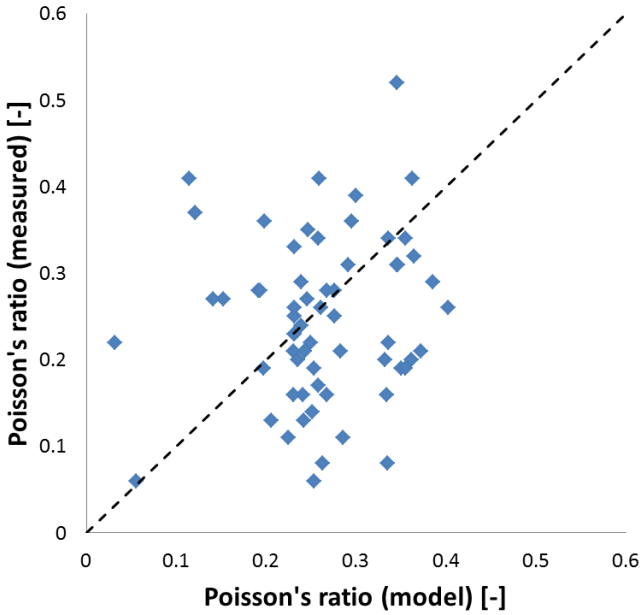

Figure 5-9. Measured ν vs modeled ν (P-waves).

5.5.2 S-waves

The following values for a [-], b [1/Pa], c [1/Pa], d [1/Pa^2], e [1/Pa^2] and f [1/Pa^2] for S-waves were found;

$$\begin{aligned} a &= 1.435 \\ b &= -26.37 \\ c &= -0.055 \\ d &= 134.85 \\ e &= -0.00067 \\ f &= 0.755 \end{aligned} \tag{5-18}$$

giving R_1^2 = 0.648, and is compared to the measured Poisson's ratio in Figure 5-10.

And finally, with σ_c = 0, the modeled Poisson's ratio for S-waves is plotted as a function of shear transit time (Δt_s) in Figure 5-11, with R_2^2 = 0.9721 and $R_1^2 R_2^2$ =0.63, and the best fit given as;

$$\nu = 1.397 - 0.0188 \cdot \Delta t_s + 7 \cdot 10^{-5} \cdot \Delta t_s^2 \tag{5-19}$$

where Δt_s is given in μs/ft.

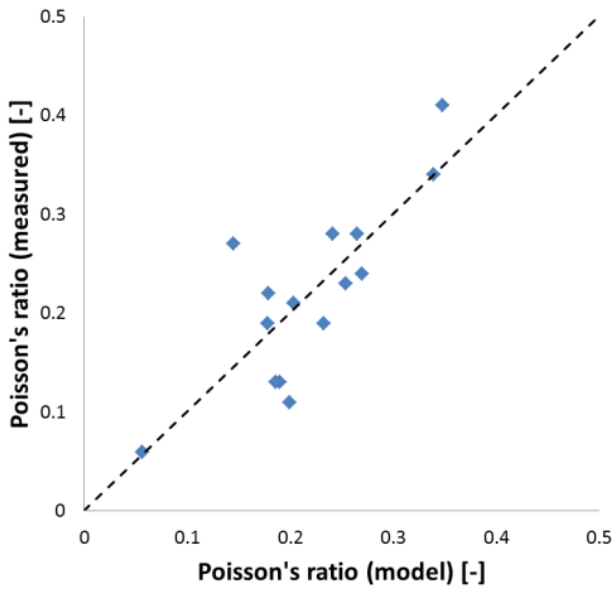

Figure 5-10. Measured ν vs modeled ν (S-waves).

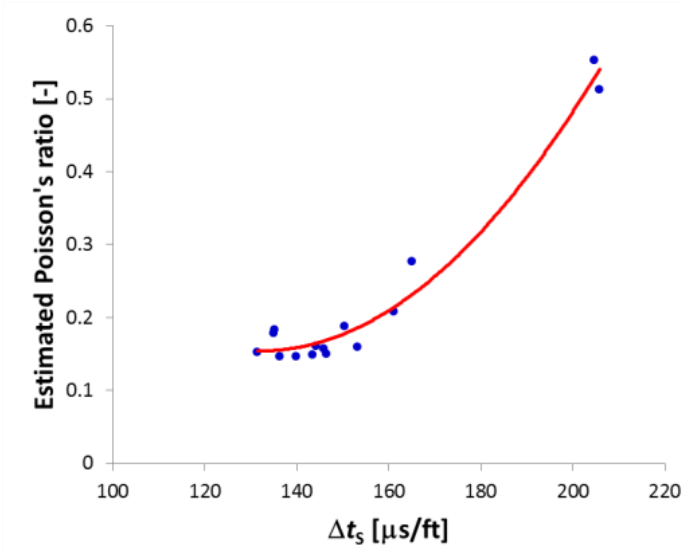

Figure 5-11. Estimated ν at zero confining pressure vs Δt_s.

5.6 Summary

A set of models have been derived for peak stress, Young's modulus and Poisson's ratio, each as a function of confining pressure, porosity, density and sonic transit time, by the use of series expansion. The aim was to obtain as small as possible sum of residuals between the modeled value and the measured value, by the use of the least squares method.

Further on the confining pressure (σ_c) was set equal to zero, and the modeled parameters were plotted as a function of compressional and shear transit time. The trendline, revealing the best fit, were found for each plot, as well as the coefficient of determination R^2 (see Table 2). The product of the coefficients of determination is included as an indication of the goodness of fit, since this product includes both steps of the models.

Table 2. Coefficients of determination R^2 for the modeled parameters and the resulting models with zero confining pressure.

Modeled parameters	R_1^2	**Eq.**	$\sigma_c = 0$	R_2^2	**Eq.**	$R_1^2 R_2^2$
Peak stress	0.6102	(5-6)	UCS	0.9133	(5-7)	0.56
Peak stress	0.7397	(5-9)	UCS	0.8567	(5-10)	0.63
Young's modulus	0.5475	(5-12)	Young's modulus	0.9282	(5-13)	0.51
Young's modulus	0.8173	(5-14)	Young's modulus	0.8901	(5-15)	0.73
Poisson's ratio	0.02	(5-17)	-	-	-	-
Poisson's ratio	0.648	(5-18)	Poisson's ratio	0.9721	(5-19)	0.63

5.7 Discussion

It can be seen in Table 2 that the obtained models including shear transit time give a better correlation for the given parameter than the models including compressional transit time. As mentioned in section 3.3, this may be a result of the considerable effect liquids has to P-waves.

6. Statistical analysis

6.1 Introduction

A statistical analysis was performed by the use of the software language R, to estimate the standard deviation (Δσ) of each obtained empirical equation in chapter 5. This was performed to give valuable insight to the validity of each obtained model. By estimating the standard deviation for the zero confining pressure parameters, the uncertainty of the transit time is taken into consideration. However, the uncertainty of the first step must also be regarded, as this may influence the second step to a large degree. The overall procedure is given below, and is also linked to each multiple-frame picture (a - f) in Figure 6-1 to Figure 6-6.

For each given parameter, i.e. peak stress, Young's modulus and Poisson's ratio, the obtained model values were plotted against the measured values (multiple-frame picture a). The errors, i.e. the difference between the model and the measured value, were then plotted against the measured value, to evaluate if the errors were increasing or decreasing with increasing measured value (multiple-frame picture c). The errors were then plotted as a histogram (multiple-frame picture e), and in a normal Q-Q plot (multiple-frame picture g). A normal Q-Q plot compares the observed sample quantiles with the theoretical quantiles of a normal distribution with an expected value of zero and a given value of standard deviation, and would thereby reveal a straight line if the sample quantiles are given by a normal distribution as well.

Further on, the obtained values with zero confining pressure were plotted as a function of the respective transit time, i.e. compressional or shear transit time (multiple-frame picture b). In the same picture, the obtained best-fit equation was plotted as a red line, and a 95% confidence interval (given in blue lines) was found by evaluating the errors between the best-fit line and each measured value. The lower limit of the 95% confidence interval was then subtracted from the upper limit, and the result was plotted as a function of the respective transit time (multiple-frame picture d). And finally, the difference between the best-fitted line and the estimated zero confining pressure values was plotted in a histogram (multiple-frame picture f) with red lines showing the 95% confidence interval, and in a normal Q-Q plot (multiple-frame picture h).

The utilized R codes are listed in Appendix C.

6.2 Peak stress

6.2.1 P-waves

The statistical analysis for peak stress and unconfined compressive strength (UCS) as a function of compressional transit time (Δt_p) are plotted in Figure 6-1.

In c), one can see that the errors, i.e. differences between modeled and measured peak stress values, are increasing with increasing measured peak stress. It can also be seen that the error is increasing in a negative manner, i.e. the obtained model is estimating too low values compared to the measured values as the peak stress is increasing. In the plotted histogram in e), a near normal distribution is observed, which is confirmed by the normal Q-Q plot in g).

In b), the modeled UCS is plotted as a function of Δt_p. In d) it can be seen that the 95% confidence interval is constant regardless of Δt_p, and is thereby homoscedastic. The confidence interval is not narrowing or widening and this implies that the resulting standard deviation found is constant, and not a function of Δt_p. The resulting histogram of the error between modeled UCS and the obtained best-fit line in f) show a similar trend to that of a normal distribution, and is confirmed by the normal Q-Q plot in h), despite the small breaks in the curve.

The standard deviation $\Delta\sigma_1$ was estimated to 24.77 MPa, resulting in;

$$\sigma_{\max} = A + \sigma_c \cdot B \pm 24.77 \tag{6-1}$$

where σ_{max} is the peak stress given in MPa, σ_c is the confining pressure given in MPa, and A and B are given in Eq. (5-6).

For the modeled UCS, the standard deviation $\Delta\sigma_2$ was estimated to 8.1 MPa;

$$UCS = 1198 \cdot e^{-0.035\Delta t_P} \pm 8.1 \tag{6-2}$$

where UCS is given in MPa and Δt_p in μs/ft.

It may also be convenient to summarize the two errors found, this to take into consideration the error in the first step (multiple-frame picture a and c) of the statistical analysis, as this may give a better indication of the validity of the fitted red line to the UCS in b). By using Eq. (6-3), which applies for summation of independent errors,

$$\Delta\sigma = \sqrt{(\Delta\sigma_1)^2 + (\Delta\sigma_2)^2} \tag{6-3}$$

it was found that the error $\Delta\sigma$ for UCS (for P-waves) was equal to 26.06 MPa, thereby resulting in a much higher uncertainty (see Eq. (6-4)).

$$UCS = 1198 \cdot e^{-0.035\Delta t_P} \pm 26.06 \tag{6-4}$$

where UCS is given in MPa and Δt_p in µs/ft.

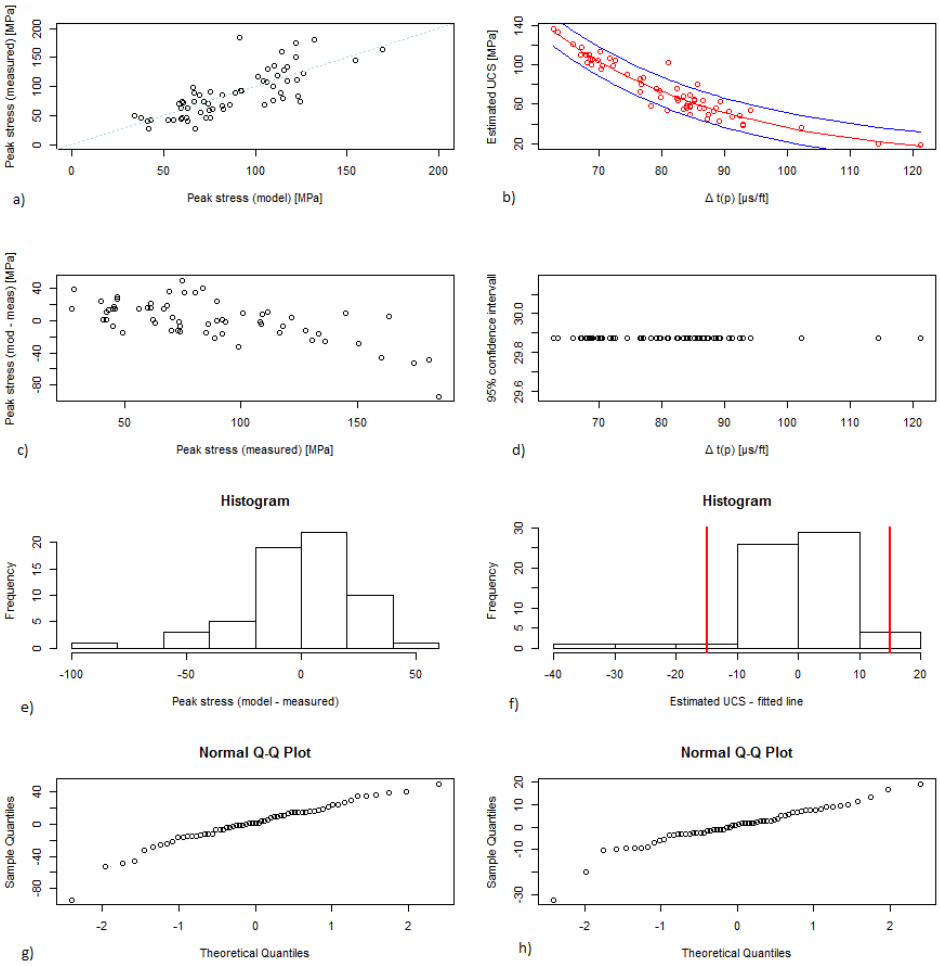

Figure 6-1. Statistical plots - peak stress and UCS for P-waves.

6.2.2 S-waves

The statistical analysis for peak stress and UCS as a function of shear transit time (Δt_s) is plotted in Figure 6-2.

The difference between the modeled and the measured peak stress for S-waves in c), are not showing any clear trend with increasing measured peak stress value. This is also evident from the histogram in e), which shows almost no resemblance to a normal distribution, and the non-linear curve in the normal Q-Q plot in g).

The modeled UCS is plotted as a function of Δt_s in b). As for P-waves, there are no changes in the 95% confidence interval with increasing Δt_s, and the resulting error is thereby constant. Although the histogram (f) resembles a normal distribution, the normal Q-Q plot (h) reveals that this is not the case (non-linear curve).

The statistical analysis performed here resulted in a standard deviation $\Delta\sigma_1$ of 10.76 MPa for the modeled peak stress for S-waves;

$$\sigma_{\max} = A + \sigma_c \cdot B \pm 10.76 \tag{6-5}$$

where σ_{max} is given in MPa, σ_c in MPa, and A and B are given in Eq. (5-9).

A standard deviation $\Delta\sigma_2$ = 6.5 MPa was determined for the modeled UCS for S-waves;

$$UCS = 426 \cdot e^{-0.015\Delta t_S} \pm 6.5 \tag{6-6}$$

where UCS is given in MPa and Δt_s in μs/ft.

By the use Eq. (6-3) it was found that the uncertainty $\Delta\sigma$ for the modeled UCS for S-waves, which depend on both steps in the statistical analysis, was equal to 12.57 MPa.

$$UCS = 426 \cdot e^{-0.015\Delta t_S} \pm 12.57 \qquad (6\text{-}7)$$

where UCS is given in MPa and Δt_s is given in µs/ft.

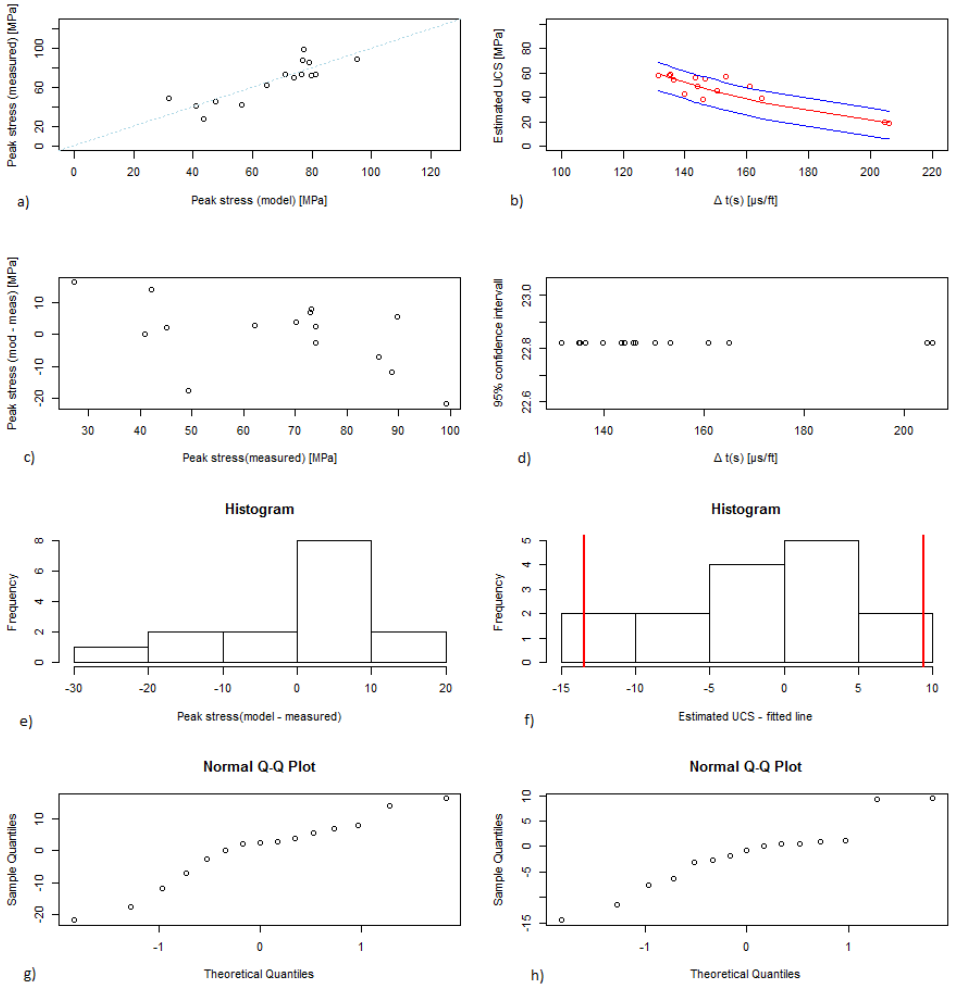

Figure 6-2. Statistical plots - peak stress and UCS for S-waves.

6.3 Young's modulus

6.3.1 P-waves

The statistical analysis for Young's modulus as a function of compressional transit time (Δt_p) is given in Figure 6-3.

In c) one can see that the difference between the modeled and the measured Young's modulus is increasing with increasing values for the measured Young's modulus. As for peak stress (for P-waves) the difference is increasing in a negative manner. But it can also be seen, by comparing with the plot in a), that the model is estimating too high values for Young's modulus for some low measured values. This may result in that the errors cancel each other out and when plotted as a histogram in e) and a normal Q-Q plot in g), the result would appear as a near normal distribution. From Figure 6-3 c) it can also be seen that the data seem to divide into two groups, and within each group there is a clear trend. This may be a result of different compaction and/or mineralogical composition, the depth-interval may also be an explanation. As these plug samples are collected from different depths in different wells on the Norwegian shelf, the latter is the most likely explanation. Such observations is an indication of that the derived and utilized equations are not optimal, and thereby should be revised.

In d) one can see the difference between the upper and lower limit of the 95% confidence interval, and it is evident that this is constant and not dependent of Δt_p. The histogram in f) show a near normal distribution trend, which is confirmed by the normal Q-Q plot in h).

The obtained standard deviation $\Delta\sigma_1$ was found to be 5.34 GPa for the modeled Young's modulus (E), giving;

$$E = a + b \cdot x_p + c \cdot \sigma_c + d \cdot x_p^2 + e \cdot \sigma_c^2 + f \cdot x_p \cdot \sigma_c \pm 5.34 \qquad (6\text{-}8)$$

where E is given in GPa, σ_c in MPa, x_p is the dynamic stiffness given in $g.cm^{-3}.cm^2.\mu s^{-2}$, and the parameters a-f are given in Eq. (5-12).

For the modeled Young's modulus with $\sigma_c = 0$, the statistical analysis revealed a standard deviation $\Delta\sigma_2$ of 2.12 GPa, resulting in;

$$E = 9926\left(\Delta t_P - 38.1\right)^{-1.73} \pm 2.12 \qquad (6\text{-}9)$$

where E is given in GPa and Δt_p in µs/ft.

The standard deviation $\Delta\sigma$ which depends on both steps in the statistical analysis (Eq. (6-3)) was found to be 5.75 GPa, resulting in the following equation for Young's modulus for P-waves with zero confining pressure;

$$E = 9926\left(\Delta t_P - 38.1\right)^{-1.73} \pm 5.75 \qquad (6\text{-}10)$$

where E is given in GPa and Δt_p in µs/ft.

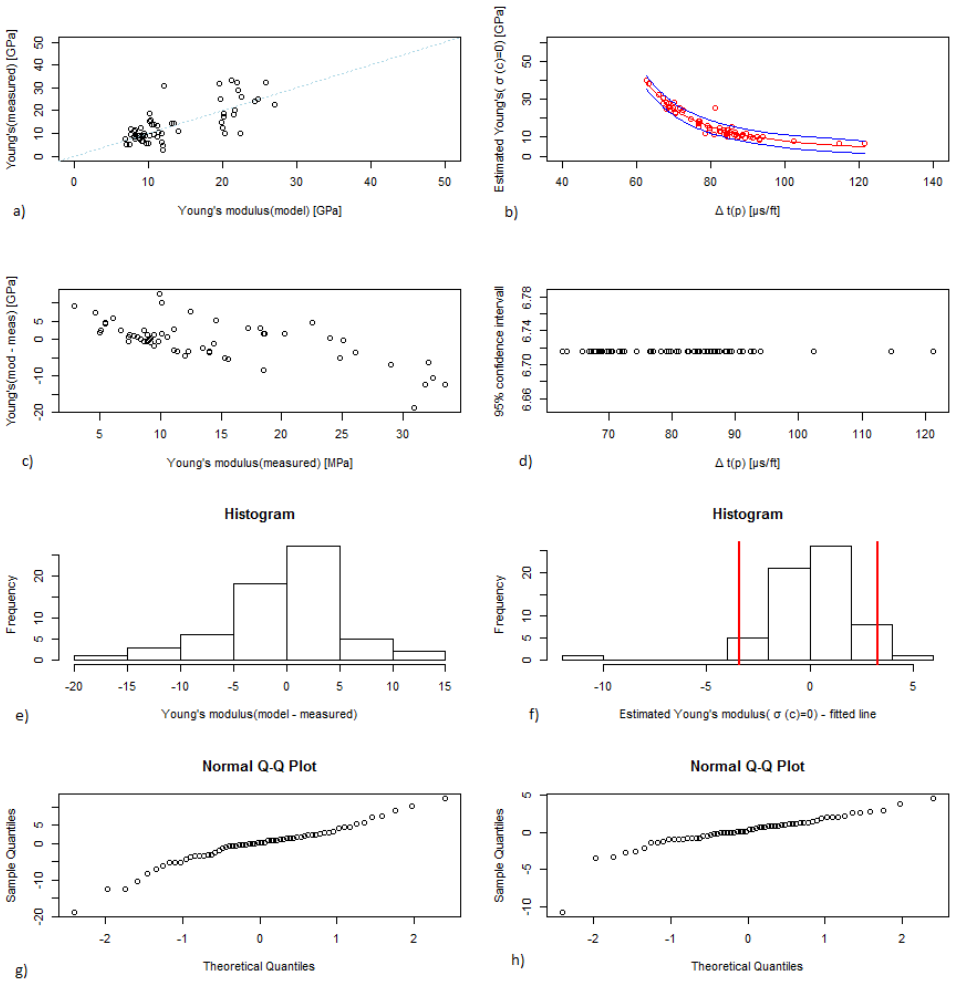

Figure 6-3. Statistical plots - Young's modulus for P-waves.

6.3.2 S-waves

In Figure 6-4, the performed statistical analysis for Young's modulus as a function of shear transit time (Δt_s) is given.

As can be seen in a), the modeled Young's modulus seem to give a fairly good estimate of the measured Young's modulus. And in c) one can see that the difference between the modeled and the measured value does not appear to increase or decrease with increasing measured values. In the histogram (e), no normal distribution is observed, which is confirmed by the normal Q-Q plot in g).

The estimated Young's modulus values for zero confining pressure are plotted as a function of Δt_s in b). And as can be seen in d), this 95% confidence interval is constant regarded to Δt_s. The histogram in f) and the normal Q-Q plot in h) do not indicate that of a normal distribution.

This statistical analysis gave a standard deviation $\Delta\sigma_1$ of 1.56 GPa for the modeled Young's modulus, resulting in;

$$E = a + b \cdot x_s + c \cdot \sigma_c + d \cdot x_s^2 + e \cdot \sigma_c^2 + f \cdot x_s \cdot \sigma_c \pm 1.56 \qquad (6\text{-}11)$$

where E is given in GPa, σ_c in MPa, x_s is the dynamic shear stiffness given in $g.cm^{-3}.cm^2.\mu s^{-2}$, and the parameters a-f are given in Eq. (5-14).

A value of 1.2 GPa as standard deviation $\Delta\sigma_2$ was found by the statistical analysis for the estimated Young's modulus with zero confining pressure, resulting in;

$$E = 170\left(\Delta t_S - 107.4\right)^{-0.716} \pm 1.2 \qquad (6\text{-}12)$$

where E is given in GPa and Δt_s in μs/ft.

As for the previous parameters, the standard deviations for each step in the statistical analysis (Eq. (6-3)) were summarized. This resulted in a possible error $\Delta\sigma$ of 1.97 GPa for Young's modulus for S-waves with zero confining pressure.

$$E = 170\left(\Delta t_S - 107.4\right)^{-0.716} \pm 1.97 \qquad (6\text{-}13)$$

where E is given in GPa and Δt_s in μs/ft.

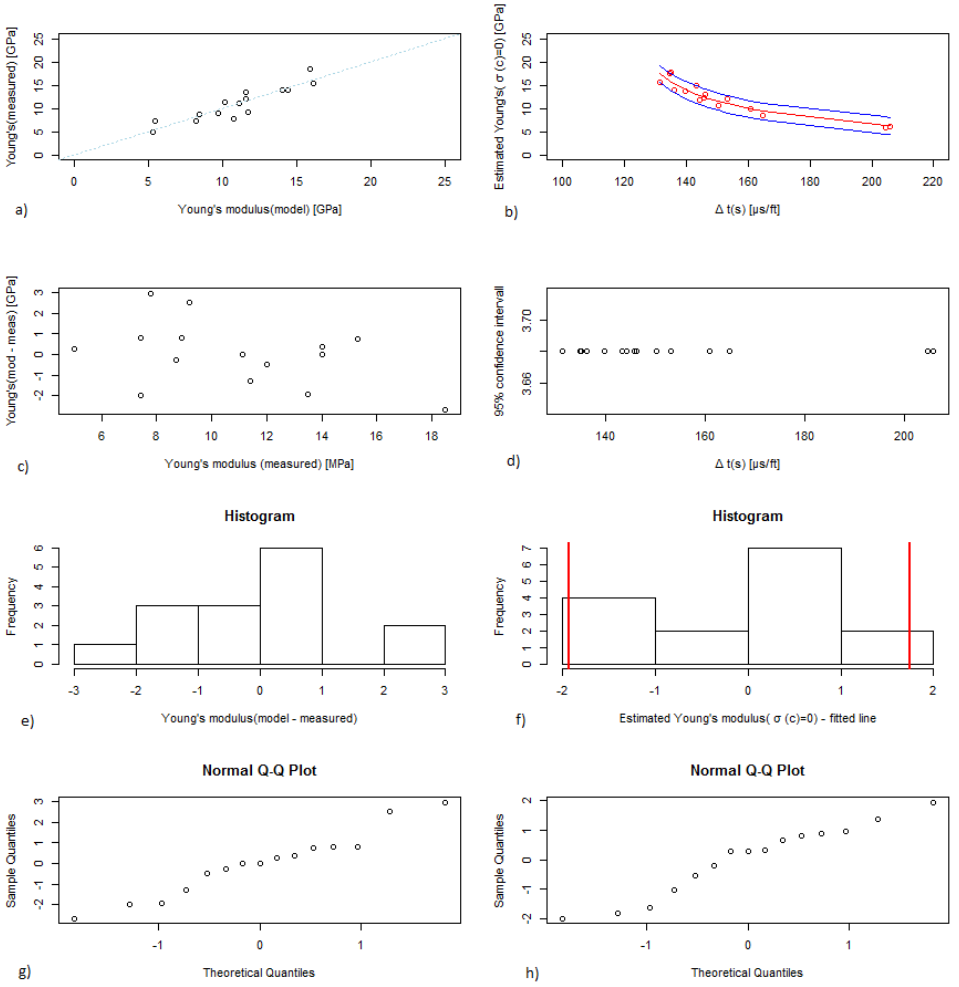

Figure 6-4. Statistical plots - Young's modulus for S-waves.

6.4 Poisson's ratio

6.4.1 P-waves

Statistical analysis for Poisson's ratio as a function of P-waves is shortened compared to the other performed analyses. This is due to the reason that no correlation between the modeled Poisson's ratio and the measured Poisson's ratio was found (see section 5.5.1 and Figure 6-5 a)).

In a), the modeled Poisson's ratio and the measured Poisson's ratio is compared. b) plot the errors, i.e. the difference between the modeled and the measured Poisson's ratio, versus the measured Poisson's ratio. The histogram of the errors is given in c), and the normal Q-Q plot of the errors is given in d).

In b) it may look like that the difference between the modeled and the measured value of Poisson's ratio is increasing in a negative manner as the measured value of the Poisson's ratio increases. And in c) the difference reveal a relatively good normal distribution trend, confirmed by the normal Q-Q plot in d). However, these obtained data are not reliable and should not be used.

The short statistical analysis resulted in a standard deviation $\Delta\sigma_1$ of 0.114 for the modeled Poisson's ratio for P-waves, resulting in the following equation;

$$\nu = a + b \cdot x_p + c \cdot \sigma_c + d \cdot x_p^2 + e \cdot \sigma_c^2 + f \cdot x_p \cdot \sigma_c \pm 0.114 \qquad (6\text{-}14)$$

where v is the Poisson's ratio, σ_c is given in MPa, x_p in $g.cm^{-3}.cm^2.\mu s^{-2}$, and the parameters a-f are given in Eq. (5-17).

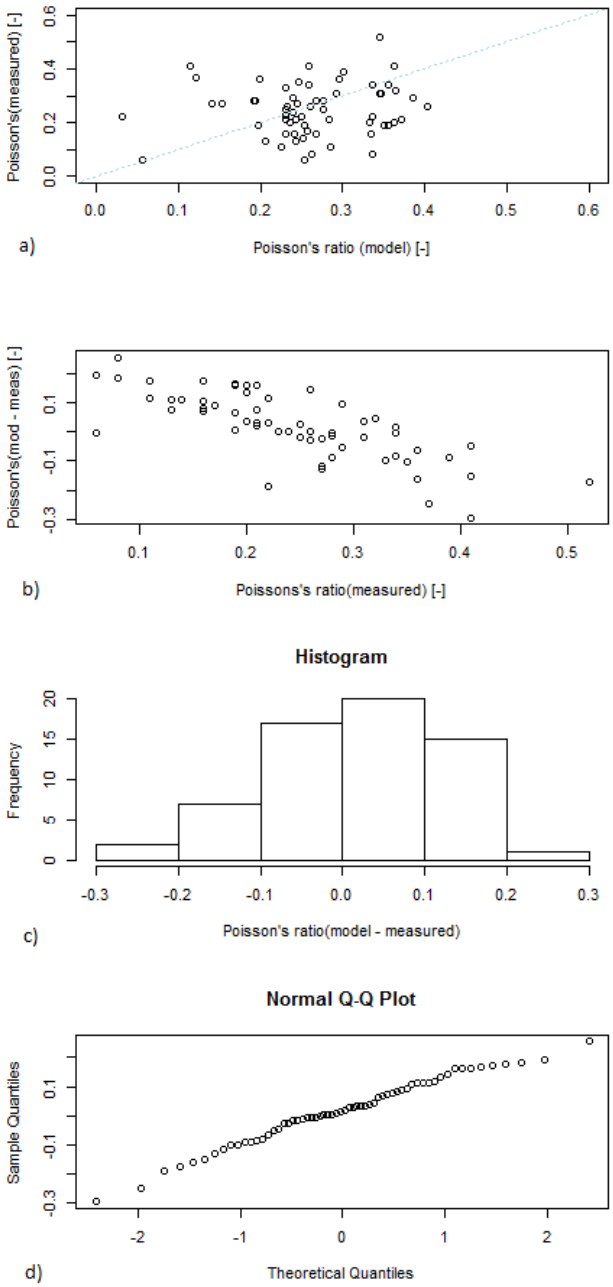

Figure 6-5. Statistical plots - Poisson's ratio for P-waves.

6.4.2 S-waves

The final statistical analysis was performed for Poisson's ratio as a function of shear transit time (Δt_s), and the resulting plot are shown in Figure 6-6.

In c) one can see some slight evidence of increasing errors, i.e. difference between modeled and measured Poisson's ratio for S-waves, with increasing measured values. As for previous parameters, this increase in errors is in a negative manner, i.e. the model is estimating too low values as the measured value increase. This is also confirmed by the histogram in e) and the normal Q-Q plot in g), as these show no normal distribution trend or no linear trend, respectively.

As for the other parameters, i.e. peak stress and Young's modulus, the 95% confidence interval is constant and thereby not related to Δt_s (d). The difference between the fitted line and the measured values for Poisson's ratio with zero confining pressure in the histogram in f) shows no normal distribution trend. This is also confirmed by the normal Q-Q plot in h).

The statistical analysis resulted in a standard deviation $\Delta\sigma_1$ of 0.054 for the modeled Poisson's ratio, resulting in the following equation;

$$\nu = a + b \cdot x + c \cdot \sigma_c + d \cdot x^2 + e \cdot \sigma_c^2 + f \cdot x \cdot \sigma_c \pm 0.054 \qquad (6\text{-}15)$$

where v is the Poisson's ratio, σ_c is given in MPa, x_s in $g.cm^{-3}.cm^2.\mu s^{-2}$, and the parameters a-f are given in Eq. (5-18).

The standard deviation $\Delta\sigma_2$ for estimated Poisson's ratio at zero confining pressure was found to be equal to 0.022, giving;

$$\nu = 1.40 - 0.0188\Delta t_S + 7.1 \cdot 10^{-5} \Delta t_S^2 \pm 0.022 \qquad (6\text{-}16)$$

where Δt_s is given in μs/ft.

And finally, the two-step dependent standard deviation $\Delta\sigma$ (Eq. (6-3)) for Poisson's ratio with zero confining pressure for S-waves was found to be equal to 0.058.

$$\nu = 1.40 - 0.0188\Delta t_S + 7.1\cdot 10^{-5}\Delta t_S^2 \pm 0.058 \qquad (6\text{-}17)$$

where Δt_s is given in μs/ft.

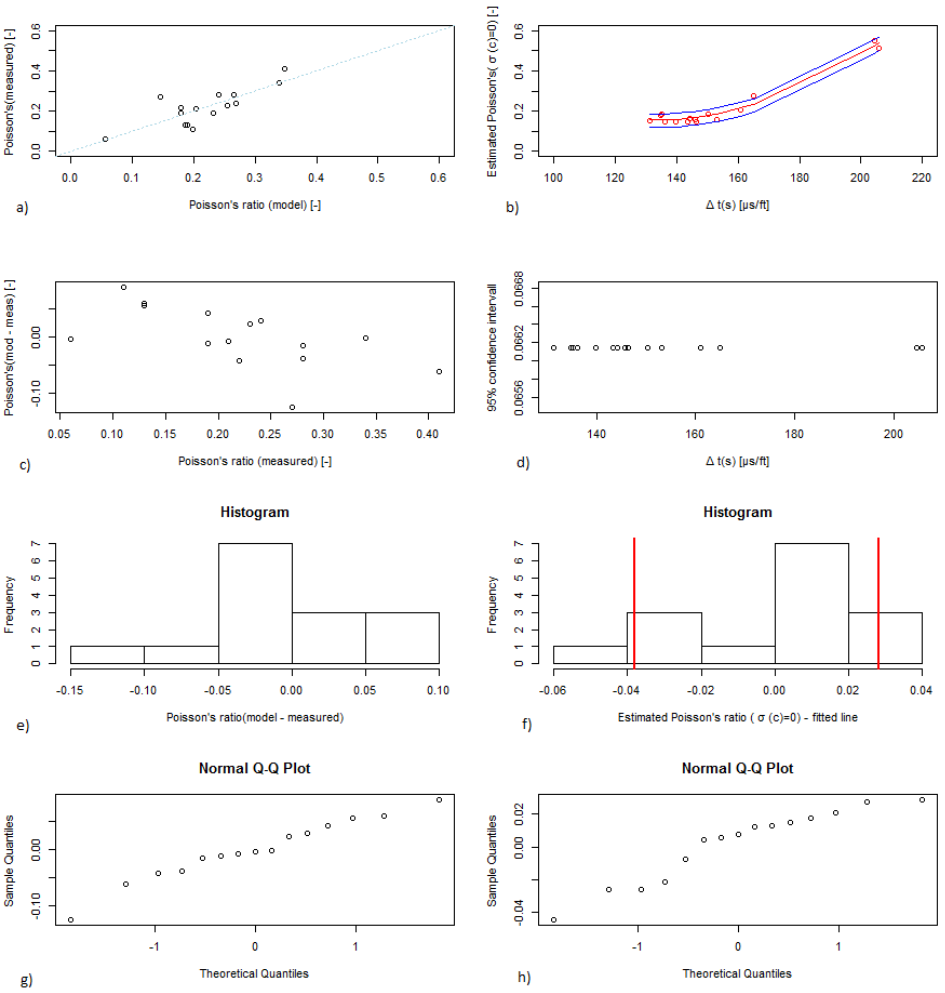

Figure 6-6. Statistical plots - Poisson's ratio for S-waves.

6.5 Summary

A set of statistical analyses were performed for peak stress, Young's modulus and Poisson's ratio, for both P- waves and S-waves, by the use of the software language R. This resulted in a set of statistical errors for the empirical equations, found earlier in chapter 5, for the respective parameters.

It was found that for each modeled parameter the error between the modeled and the measured value is increasing with increasing measured value. However, this trend is not as clear for the model for peak stress (S-waves) and Young's modulus (S-waves). The increasing error is observed to be in a negative manner, i.e. the given model is estimating too low values when the measured values increase.

A 95% confidence interval was determined for each zero confining pressure parameter, and the results were the same for all six statistical analyses. The confidence intervals were constant, i.e. they do not dependent of their respective transit times.

The confidence intervals resulted in a set of estimated standard deviations ($\Delta\sigma$) that also were constant, and not a function of their respective transit times. These standard deviations were summarized to ensure that the uncertainty of the whole correlation, i.e. both steps, was taken into account. It was found that the uncertainty was significantly higher when taking both steps into account.

The error between the modeled and the measured value and the error between the fitted line and the modeled zero confining pressure value were plotted in a histogram and in a normal Q-Q plot for each parameter. This was performed to reveal any resemblances to a normal distribution. The overall trend showed a close resemblance to a normal distribution for P-wave related models.

Table 3. Standard deviation $\Delta\sigma=\sqrt{((\Delta\sigma_1)^2+(\Delta\sigma_2)^2)}$ for the modeled parameters and for the resulting models with zero confining pressure.

Modeled parameter	$\Delta\sigma_1$	**Eq.**	$\sigma_c = 0$	$\Delta\sigma_2$	**Eq.**	$\Delta\sigma$	**Eq.**
Peak stress	24.77 MPa	(6-1)	UCS	8.1 MPa	(6-2)	26.06 MPa	(6-4)
Peak stress	10.76 MPa	(6-5)	UCS	6.5 MPa	(6-6)	12.57 MPa	(6-7)
Young's modulus	5.34 GPa	(6-8)	Young's modulus	2.12 GPa	(6-9)	5.75 GPa	(6-10)
Young's modulus	1.56 GPa	(6-11)	Young's modulus	1.2 GPa	(6-12)	1.97 GPa	(6-13)
Poisson's ratio	0.114	(6-14)	-	-	-	-	-
Poisson's ratio	0.054	(6-15)	Poisson's ratio	0.022	(6-16)	0.058	(6-17)

6.6 Discussion

The increasing error, between the modeled and measured value, may be a result of the confining pressure. As the measurements have been conducted at different confining pressures during the triaxial compression tests, the obtained models may be affected by this and thereby give better approximations for lower values than for higher values of confining pressure. Normally the UCS reveals more scatter at low confining pressures, i.e. opposite of what obtained here. This may imply that the estimated models utilized for these unpublished data are not adequate enough, and such results should be used to improve the empirical models by the choice of functions.

Due to the reoccurring trend of independence to the respective transit time, there is most likely a distinctive reason for this. Such a reason may be an error in the statistical analysis.

7. Validation of results

To confirm the validity of the obtained empirical equations, the results have been compared to log data from the same wells as those the unpublished data from the Norwegian shelf utilized in this study were obtained from.

In the log data provided by Statoil, the measured compressional transit time (Δt_p) is found and utilized in the empirical equations for unconfined compressive strength (UCS) and Young's modulus. Since only Δt_p is available from the log data, only the empirical equations who take Δt_p into account will be evaluated. Poisson's ratio will not be evaluated as there has not been found a reliable correlation for this parameter with Δt_p.

The compressional transit time found by acoustic measurements in the laboratory is also plotted together with the original log data. This is to ensure that the depth that is measured from the logs and the depth that is given to the laboratory measurements is the same. This comparison is performed since the wireline may stretch due to the weight of the wireline and the drill track may not be vertical, and thereby log-depth and plug-depth do not coincide.

7.1 Relations from literature

When comparing the results for UCS obtained in this study with already published relations (see section 4.4), it is noticed that the obtained empirical equation related to Δt_p (Eq. (5-7)) is almost identical to the relation presented by McNally (1987) (Eq. (4-4)). The empirical equation found by McNally (1987) was based on rock from the Bowen Basin in Australia, which included all porosity ranges.

In Figure 7-1, one can see the mentioned empirical equations given in literature plotted as a function of Δt_p. Also plotted is the unpublished data set from the Norwegian shelf utilized in this study, and it can be seen that these falls in the middle of the range spanned by the published relations. The best fit for an exponential trendline through the data from the Norwegian shelf matches almost exactly, as mentioned above, the empirical correlation derived by McNally (1987) for a set of sandstones (sst) from Australia. (Brandås et al. 2012, see Appendix A).

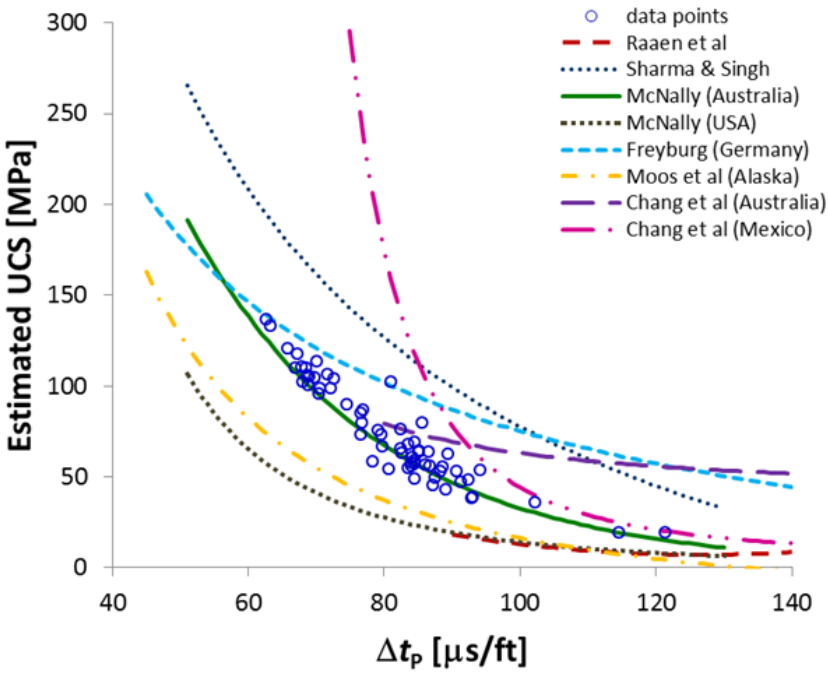

Figure 7-1. Estimated UCS vs Δt_p from this study, compared to a set of published relations for sst.

7.2 Log data

7.2.1 Unconfined compressive strength

When the available plug samples provided by Statoil were subjected to laboratory test by Weatherford Laboratories, a triaxial compression test (TCT) was performed on each plug sample. Normally the UCS of a material is determined by the uniaxial compressive strength test (see section 3.4), but here the Mohr-Coulomb failure envelope (linear extrapolation) was utilized to determine the UCS from the TCT (see section 3.2 and 3.3). This implies that the value plotted in Figure 7-2 as "measured UCS" is in reality an extrapolated UCS value from the laboratory.

As can be seen from Figure 7-2, the empirical equation for determining the UCS by the use of Δt_p (Eq. (5-7)) model a higher value than what estimated from the laboratory tests. This over-estimation of the UCS is regarded to be 0 – 90 %.

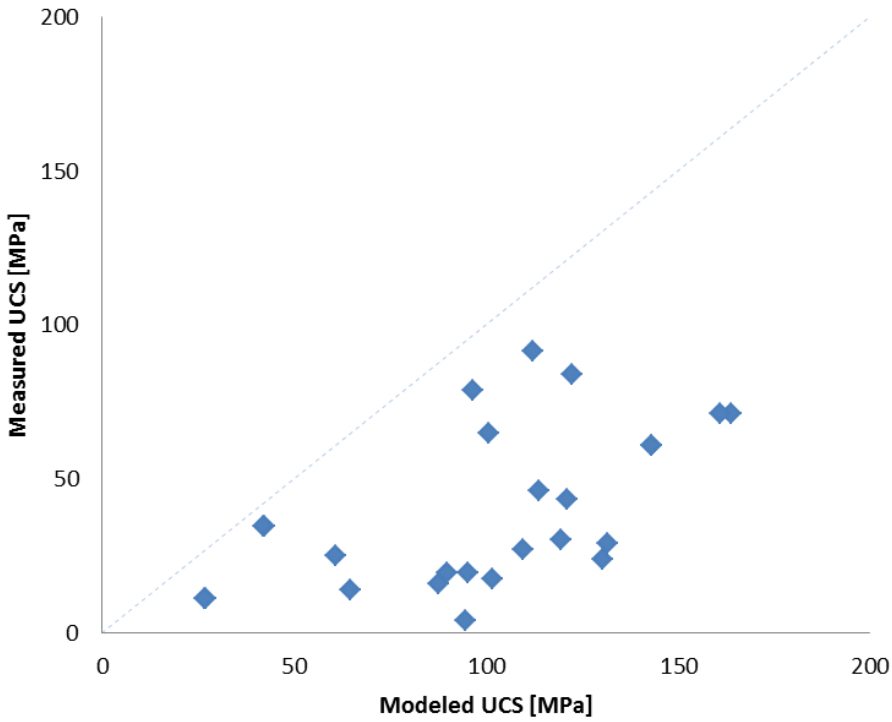

Figure 7-2. Measured UCS vs modeled UCS.

7.2.2 Young's modulus

Young's modulus (E) is also found from the triaxial compression test (TCT) performed by Weatherford Laboratories. This is done by performing linear regression, normally in the 40-60% area of the peak stress of the given plug. A more thoroughly explanation can be found in Appendix B.5.

The values plotted as "measured Young's modulus" in Figure 7-3 is therefore found by direct measurements on each plug samples. These values are thereby regarded as valid and true. As can be seen in Figure 7-3, the modeled Young's modulus from Δt_p, obtained from Eq. (5-13), estimate higher values of Young's modulus than those found from laboratory measurements.

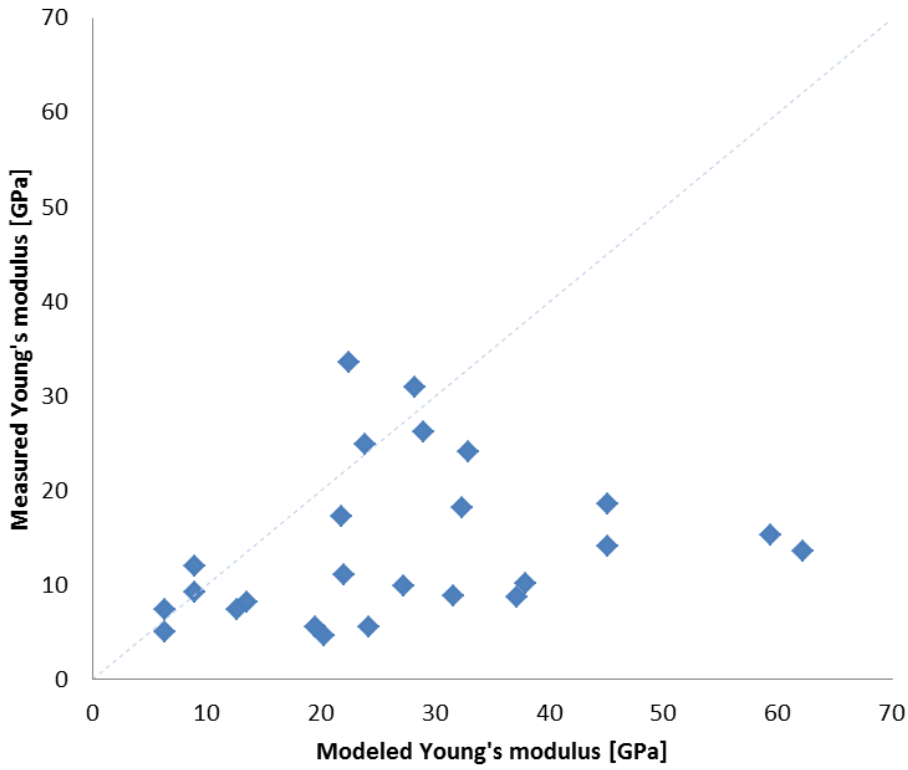

Figure 7-3. Measured E vs modeled E.

7.3 Log-depth to core-depth

The original log-values for the unpublished data from the Norwegian shelf were provided by Statoil, and the compressional transit time (Δt_p) obtained from the four different logs (i.e. four different wells) are plotted as a function of depth in Figure 7-4 to Figure 7-7. Also plotted is the laboratory measured Δt_p, with the confining pressure given in the legend.

When drilling a well, the wireline may stretch due to the weight of itself. And when measuring the length of the wireline, the direction of the wireline must be taken into consideration, as the well may be drilled vertically or at a given angle. These are two reasons for any possible differences between the log-depth and the core-depth for the given plug samples from the Norwegian shelf.

As can be seen from Figure 7-4 to Figure 7-7, the laboratory measured Δt_p is generally higher than the log-Δt_p.

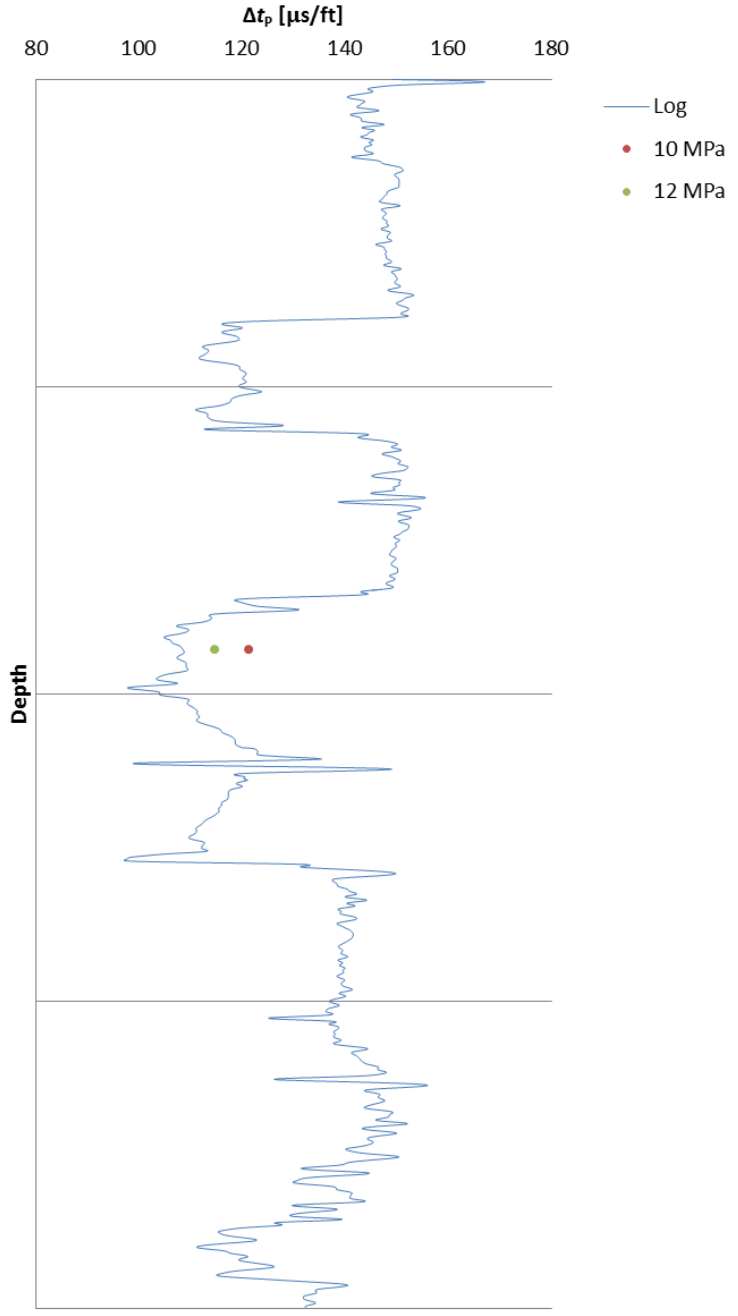

Figure 7-4. Log-depth vs log-Δt_p well 1. Measured Δt_p is included.

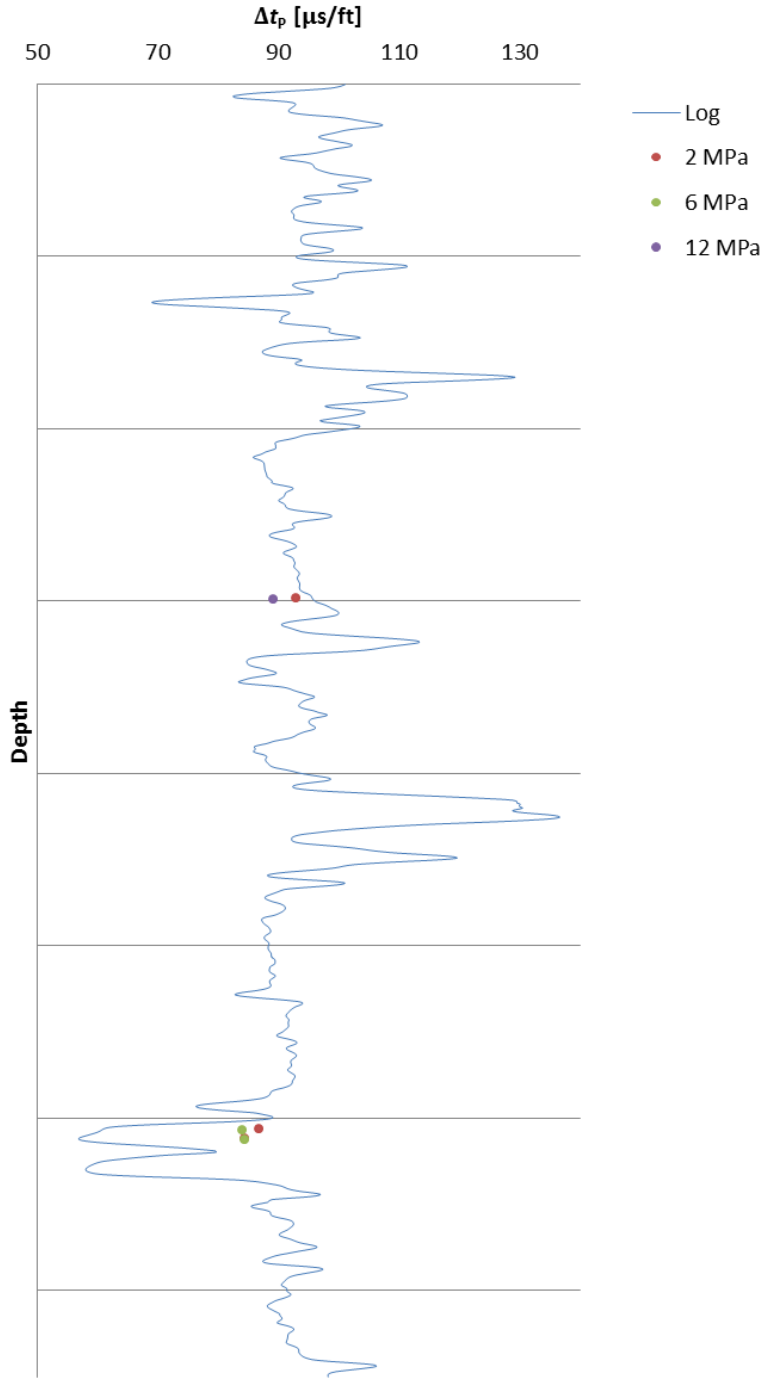

Figure 7-5. Log-depth vs log-Δt_p well 2. Measured Δt_p is included.

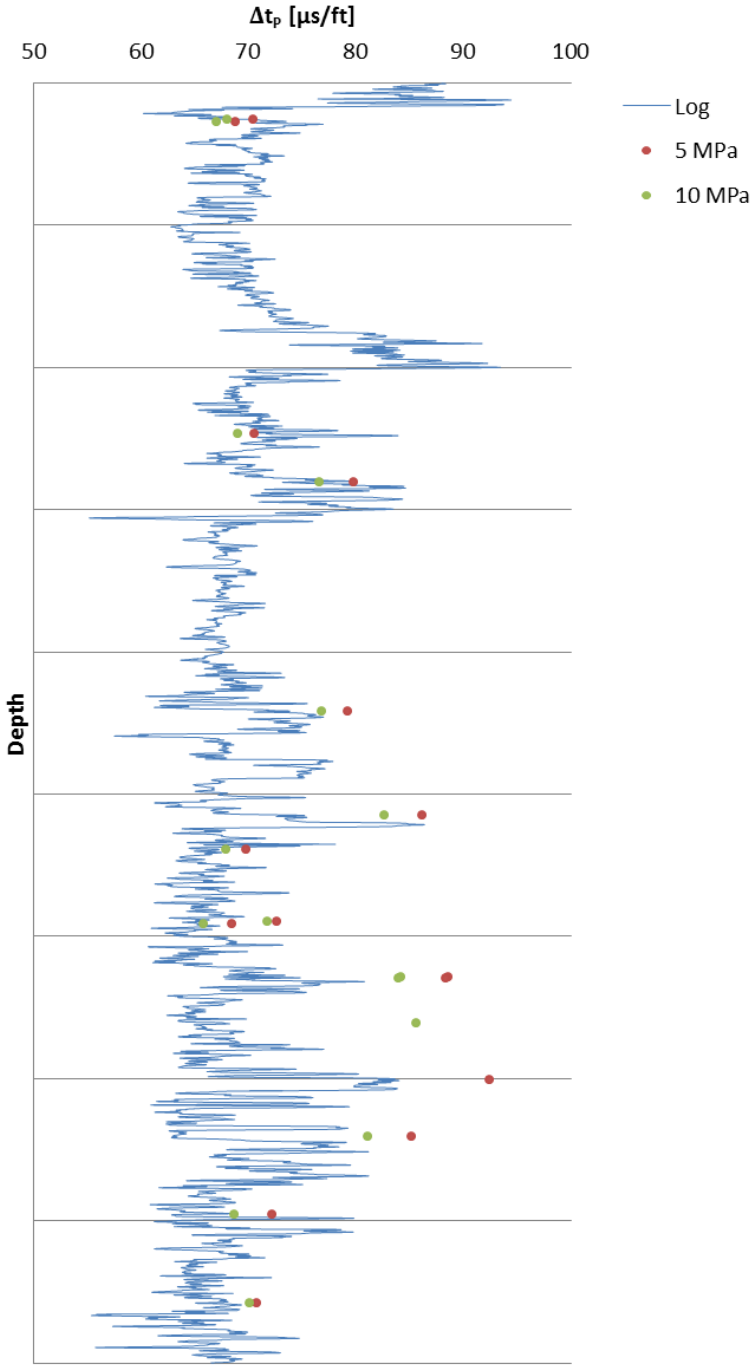

Figure 7-6. Log-depth vs log-Δt_p well 3. Measured Δt_p is included.

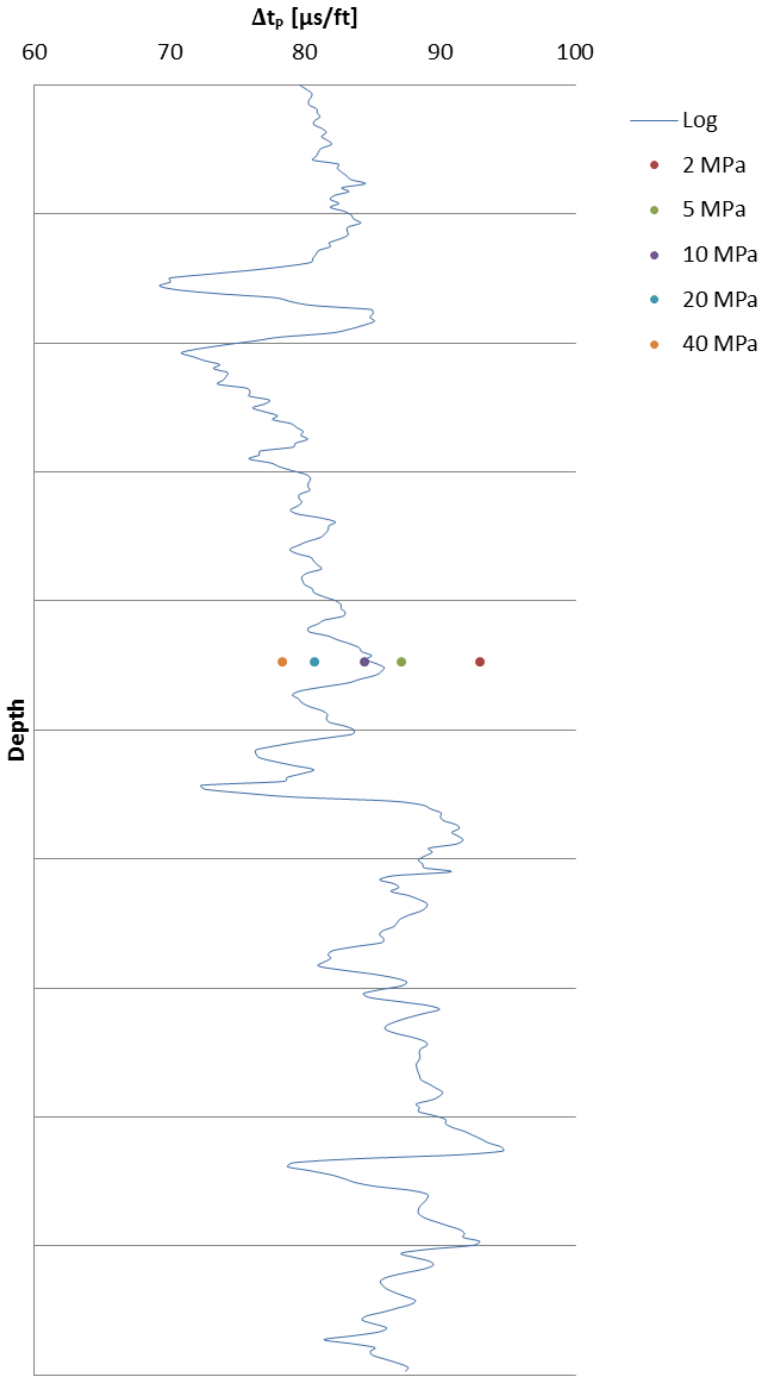

Figure 7-7. Log-depth vs log-Δt_p well 4. Measured Δt_p is included.

7.4 Depth shifting

By depth shifting, the possible stretch of the wireline and the possible non-vertical drill-track are taken into consideration.

In Figure 7-8 and Figure 7-9, a 1 meter (m) downwards depth-shift have been performed, and the resulting compressional transit time has been utilized to model new values for the UCS and the Young's modulus. By comparing Figure 7-2 and Figure 7-8, there is not observed a better correlation between modeled and measured UCS after 1 m downwards depth-shift. It is also observed that two separate group seems to form in Figure 7-8, which may be a result of different compaction and mineralogical composition between the data from the Norwegian shelf. A better correlation for Young's modulus after a 1 m downwards depth-shift is not observed (see Figure 7-3 and Figure 7-9).

In Figure 7-10 and Figure 7-11, a 1 m depth-shift has been performed both downwards and upwards. The plotted lines give the span for the upper and lower limit of the given parameter. Despite several increments for depth-shifting, where only +/- 1 m is presented in this paper, better matches for the UCS and Young's modulus (E) were not obtained.

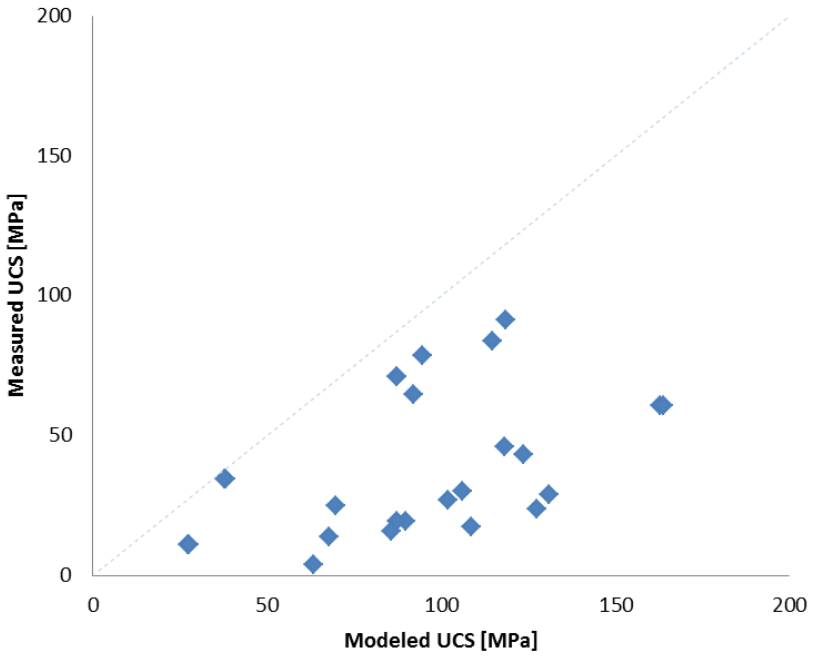

Figure 7-8. Measured UCS vs modeled UCS with 1m downwards depth shift of log.

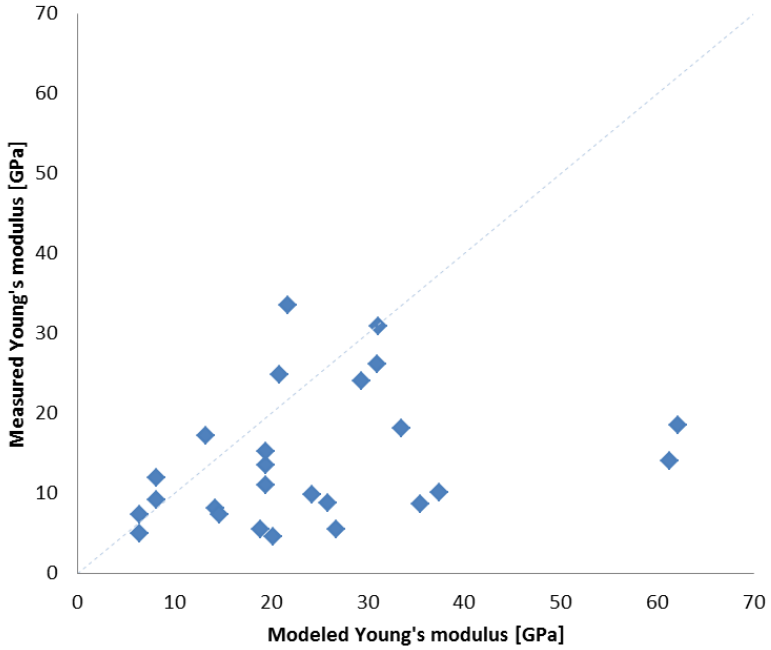

Figure 7-9. Measured E vs modeled E with 1m downwards depth shift of log.

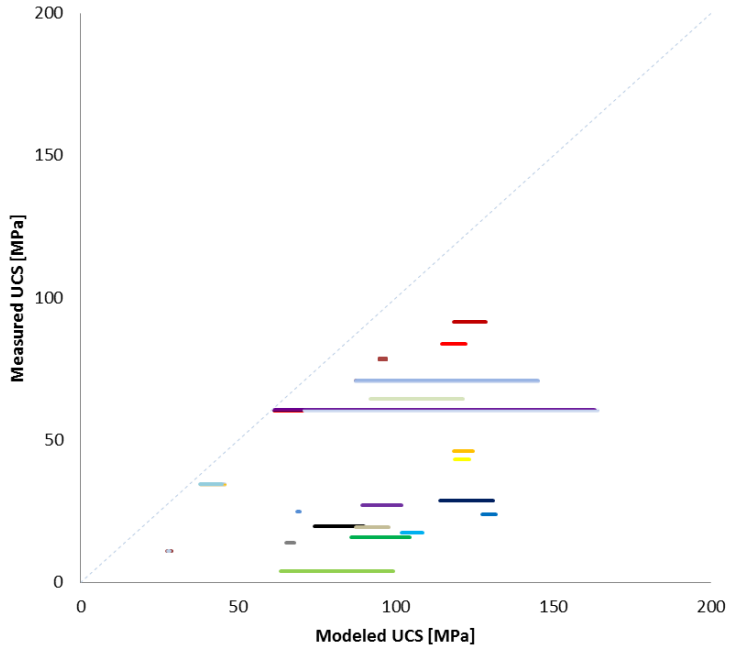

Figure 7-10. Measured UCS vs modeled UCS with +/- 1m depth shift of log.

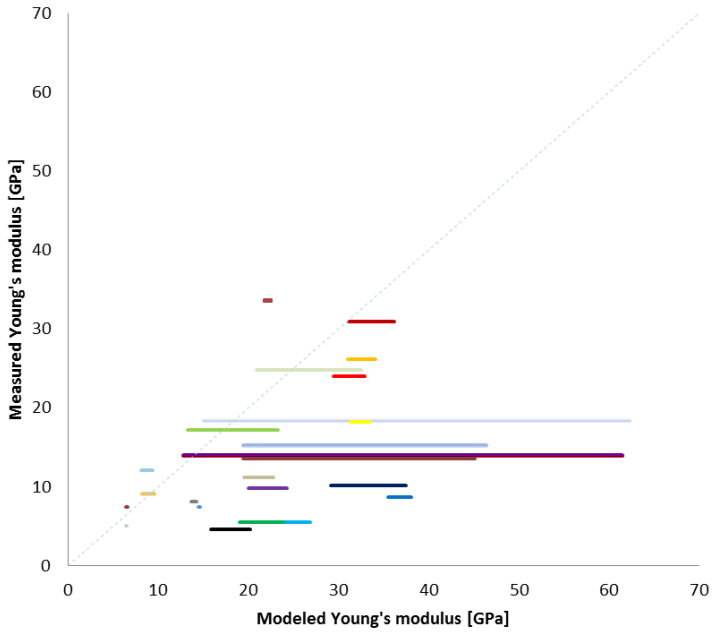

Figure 7-11. Measured E vs modeled E with +/- 1m depth shift of log.

7.5 Summary

The unpublished data from the Norwegian shelf is compared to a set of empirical equations from literature, and it is found that the obtained results fall in the middle of the range spanned by the published results (Brandås et al. 2012). It is also found that the obtained empirical equation for UCS derived from plug samples obtained from the Norwegian shelf, matches almost exactly the empirical relation found by McNally (1987), which were derived for a set of sandstone samples from the Bowen Basin in Australia.

The obtained models for unconfined compressive strength (UCS) and Young's modulus, for compressional transit time (Δt_p), are tested against log data to find the validity of the results. The estimated dynamic measurements are found by utilizing the compressional transit time obtained from directly measured log data in the obtained empirical equations. The laboratory measured Δt_p was plotted together with the log measured Δt_p, and it was found that the laboratory measured value was generally higher than the log value.

It is found that the model for UCS overestimate the values by 0 – 90 %, and that the model for Young's modulus also overestimate its values.

To allow for any possible error from a stretch in the wireline or a non-vertical drill track, depth shifting was performed. Despite several depth-shifts, including +/- 1 meter, the UCS and the Young's modulus were still overestimated by the modeled empirical equations.

7.6 Discussion

A possible explanation for the over-estimation of the UCS is that when linear extrapolation is performed, the value for the friction angle (in particular for low confining pressure) is not correct. Another possible explanation is that the Mohr-Coulomb failure envelope "dips" at a certain angle when the confining pressure approaches zero (Fjær et al. 1992). Thereby, if this "dip" is wrongly estimated, a too low value of the UCS is estimated.

However, the most likely explanation for why the log-data overestimate the strength and the stiffness is not the one described above. The empirical correlations derived in this study are valid for unconfined conditions, while the log measured transit times are valid for a rock in a given distance from the borehole wall. This standard "long-spaced" sonic log thereby give a sonic transit time measured at confining pressure that is significantly higher than what needed for the empirical correlations. As can be seen in Figure 7-7, the sonic transit time decreases with increasing confining pressure, and this should be regarded when the empirical correlations are to be used for prediction of strength and stiffness. It should also be mentioned that a significant part of this dependence to confining pressure for the transit time is most likely a result of core damage (Fjær and Holt 1999).

8. Further work

The obtained data from Statoil was limited to a set of unpublished sandstone plug samples from the Norwegian shelf. More data from all over the world is therefore highly desirable to validate and further develop the obtained empirical models.

Data sets for other lithologies, e.g. carbonates and shales, are also desired to further develop similar models for those lithologies.

As all static measurements in this study are obtained from triaxial compression tests, those values should be regarded as not valid for a zero confining pressure environment. Uniaxial compression tests should thereby be performed to ensure that all data are representative and valid.

9. Conclusion

A set of unpublished sandstone samples from the Norwegian shelf is provided by Statoil and subjected to triaxial compression tests by Weatherford Laboratories.

Empirical models have been derived for peak stress, Young's modulus and Poisson's ratio, each as a function of confining pressure, porosity, density and sonic transit time. By the use of the least squares method, the obtained sum of residuals between the modeled value and the measured value was made as small as possible in defining the fitting parameters. Empirical models for zero confining pressure were also obtained, as the empirical models were plotted as a function of compressional and shear transit time. Coefficients of determination R^2 were found, and the product for both steps were included to give an indication of the goodness of fit. A better correlation was found between S-waves and rock mechanical parameter, than between P-waves and rock mechanical parameters.

The resulting statistical errors for the empirical equations were found by the use of the software language R. For each modeled parameter, the error between the modeled and the measured value is increasing with increasing measured value. This trend was not as evident for the model for peak stress (S-waves) and Young's modulus (S-waves). A 95% confidence interval for each zero confining pressure parameter showed that they do not dependent of their respective transit times. This results in that the estimated standard deviations also are constant. These standard deviations were summarized to ensure that the uncertainty of the whole correlation, i.e. both steps, was taken into account. This resulted in a higher uncertainty, when regarding both steps in the analysis.

A comparison between the strength data obtained from the unpublished plug samples from the Norwegian shelf and a set of empirical correlations available from literature showed that the unpublished data falls in the middle of the range spanned by the published relations. The unpublished data matched the empirical correlation derived by McNally (1987) best, which were derived for a set of sandstone samples from Australia.

The validity of the obtained models for UCS and Young's modulus, for compressional transit time, were tested by the use of log data. It was found that the models overestimate the value for UCS and Young's modulus. A +/- 1 meter depth-shift were performed to compensate for any possible errors by stretch in the wireline or a non-vertical drill track. However, the results did not show any significant changes.

Taking all steps in this study into account, it was found that when establishing empirical correlations for estimation of strength and stiffness based on log-measurements, these correlations should be established as a result of laboratory measured strength or stiffness and log-measured sonic transit time. Such an approach will to a large degree eliminate the problem with core damage and confining pressure dependency. However, such an approach is not straight forward due to depth-shift issues.

10. Bibliography

Bradford, I. D. R., J. Fuller, P. J. Thompson and T. R. Walsgrove, 1998. Benefits of assessing the solids productions risk in a North Sea reservoir using elastoplastic modeling. *SPE/ISRM Eurock '98, Trondheim, Norway, July 8-10, 1998. pp. 261-269.*

Brandås, L. T., E. Fjær, K. Tokle and J. Tronvoll, 2012. Relating acoustic wave velocities to formation mechanical properties. *The 46th US Rock Mechanics / Geomechanics Symposium, Chicago, IL, 24-27 June 2012.*

Britt Rock Mechanics Lab [Internet]. [25 May, 2012] <http://www.rocklaboratory.com/content.aspx?id=23>

Carmichael, R. S., 1982. Handbook of Physical Properties of Rocks, volume 2. CRC Press, Boca Raton.

Chang C., M. D. Zoback and A. Khaksar, 2006. Empirical relations between rock strength and physical properties in sedimentary rocks. Journal of Petroleum Science. Eng 51. 223-237.

Fjær, E., and R. M. Holt, 1999. Stress and stress release effects on acoustic velocities from cores, logs and seismics. SPWLA 40th Annual Logging Symposium, May 30- June 3, 1999.

Fjær, E., R. M. Holt, P. Horsrud, A. M. Raaen and R. Risnes, 1992. Petroleum related rock mechanics. Elsevier, Amsterdam.

Freyburg, E., 1972. Der Untere und mittlere Buntsandstein SW-Thuringen in seinen gesteinstechnicschen Eigenschaften Berlin, Deustche Gesellschaft Geologische Wissenschaften. A; Berlin 176. 911-919.

Jizba, D., 1991. Mechanical and acoustical properties of sandstones and shales. PhD thesis, Stanford university, March, 1991. pp. 260.

Kwasniewski, M., 1989. Laws of brittle failure and of B-D transition in sandstones. In: Maury, V., and D. Fourmaintraux, eds., Rock at great depth. Balkema. pp. 45-58.

Lama, R. D. and V. S. Vutukuri, 1978. Handbook on mechanical properties of rocks, volume 2. Trans Tech Publications, Clausthal, Germany.

McNally, G.H., 1987. Estimation of coal measures rock strength using sonic and neutron logs. Geoexploration. 24. 381-395.

Miller, S. J., 2006. The method of least squares. Mathematics Department Brown University Providence. RI 02912.

Moos, D., M.D. Zoback and L. Bailey, 1999. Feasibility study of the stability of openhole multilaterals, Cook Inlet, Alaska. *The 1999 SPE Mid-Continent Operations Symposium, Oklahoma City, Oklahoma, 28-31 March 1999.* SPE 52186.

Nes, O.-M., P. Horsrud, E. F. Sonstebo, R. M. Holt, A. M. Ese, D. Okland and H. Kjorholt, 1996. Rig site and laboratory use of CWT acoustic velocity measurements on cuttings. *The 1996 SPE European Petroleum Conference, Milan, Italy, 22-24 October 1996.* SPE 50982.

Raaen, A.M., K.A. Hovem, H. Jøranson and E. Fjær, 1996. FORMEL: A step forward in strength logging *The 1996 SPE Annual Technical Conference and Exhibition, Denver*. SPE 36533.

Ringstad, C., E. B. Lofthus, E. F. Sonstebo, E. Fjaer, F. Zausa and G.-F. Fuh, 1998. Prediction of rock parameters from micro-indentation measurements: The effect of sample size. *SPE/ISRM Rock Mechanics in Petroleum Engineering, Trondheim, Norway, 8-10 July 1998.*

Sharma, P.K. and T.N. Singh, 2008. A correlation between P-wave velocity, impact strength index, slake durability index and uniaxial compressive strength. Bulletin of Engineering Geology and the Environment. 67. 17-22.

Wong, T.-f., C. Davis and W. Zhu, 1997. The transition from brittle faulting to cataclastic flow in porous sandstones: mechanical deformation. Journal of Geophysical Research. 102. pp. 3009-3025.

APPENDIX

A. The Article

The result of this thesis has been prepared for and presented at the 46th US Rock Mechanics / Geomechanics Symposium held in Chicago, IL, USA, 24-27 June 2012.

This article, given below, has been prepared in an A4-format, and downscaling to B5 may therefore have led to some minor divagations compared to the original printed article.

ARMA 12-399

Relating acoustic wave velocities to formation mechanical properties

Linn Tove Brandås
NTNU, Department of Petroleum Technology and Applied Geophysics, Trondheim, Norway.
Weatherford Petroleum Consultants, Trondheim, Norway.
Erling Fjær
SINTEF Petroleum Research, Trondheim, Norway.
NTNU, Department of Petroleum Technology and Applied Geophysics, Trondheim, Norway.
Karl Tokle
Weatherford Laboratories, Trondheim, Norway.
Johan Tronvoll
Weatherford Petroleum Consultants, Trondheim, Norway.

This paper was prepared for presentation at the 46th US Rock Mechanics / Geomechanics Symposium held in Chicago, IL, USA, 24-27 June 2012.

ABSTRACT:

Proper correlations between formation mechanical properties and acoustic data is essential for field rock mechanical analysis, and it has thereby a great significance to field operations such as hydraulic fracturing, wellbore stability during drilling, sand production risk evaluation, compaction studies, etc. This paper presents results from a correlation study between formation mechanical properties and acoustic wave velocities from wells in the North Sea. Correlations between formation compressive strength, elastic stiffness and Poisson's number and compressional and shear transit times have been established. The data for this study was collected from triaxial compression tests performed on core plugs at various confining pressures. The results confirm that the stress level and stress configuration affects the acoustic velocities, and this should be accounted for when using generalized empirical correlations to estimate formation strength from acoustic logs in field studies. The results are found to match reasonably well with other published relations.

1. INTRODUCTION

Geomechanics analysis has gradually become an integrated part of oilfield development. This includes topics such as pre-drill wellbore stability analyses, utilizing seismic for pore pressure estimation and basic data acquisition during exploration, wellbore stability and sand production risk analysis during the field development phase, production optimization through e.g. hydraulic fracture stimulation, as well as reservoir compaction and analysis of stress-dependent permeability for infill well placement during the production phase.

For all the above applications of geomechanics to the oil and gas industry basic rock mechanics properties have to be determined or estimated. This includes formation mechanical properties such as compressive and tensile strength, elastic properties (e.g. Young's modulus, shear modulus, bulk modulus/compressibility and Poisson's ratio) and plastic properties. Such data are normally derived from static measurements on core plugs, but measurements on cuttings or cavings may as well be used to derive certain rock mechanical properties [1,2]. However, through theoretical models and correlations well logs may be used to estimate rock mechanical parameters. The formation principal stresses (often the vertical and the maximum/minimum horizontal stresses) as well as the pore pressure are crucial input data. These data are normally harvested from well measurements (e.g. well hydraulic fracture tests, caliper/image logs and density log).

Data from one well may be applied to constitute a simple 1D model of the formation mechanical properties. The integration of various measurements from multiple wells through use of geostatistics or alternatively through a 3D numerical model enables the definition of a 3D geomechanical model or "mechanical earth model". Such models are the basis for almost any geomechanical analysis.

This paper is focusing on the determination of elastic properties and rock compressive strength for sandstone based on acoustic measurements. Based on laboratory measurements of static and dynamic properties of sandstones from North Sea reservoirs a simple empirical model is proposed for the use of sonic log data to determine compressive strength. The results are compared to published correlations from other areas and discussed.

Sonic transit time is directly related to stiffness through the relations

$$x_P = \rho\left(\Delta t_P\right)^{-2} \quad (1)$$

$$x_S = \rho\left(\Delta t_S\right)^{-2} \quad (2)$$

where x_P is the uniaxial compaction modulus, x_S is the shear modulus, ρ is the density, and Δt_p and Δt_s are the compressional and shear transit times, respectively. x_P and x_S are dynamic stiffnesses, which may differ significantly from their static counterparts for sedimentary rocks. However we expect to find some degree of correlation between the static and the dynamic stiffnesses. A link between dynamic stiffness and strength is also to be expected, since both strength and stiffness depend largely on the amount of solid material present in the rock, or – equivalently – they both depend on the porosity. However, the geometrical distribution of the solid material in terms of pore shape, degree of cementation etc.

is also important, and this distribution affects stiffness and strength differently. Thus, some correlation between strength and sonic data, and between static stiffness and sonic data, is to be expected, but these correlations may not be very strong.

A number of empirical relations between strength and sonic transit time have been presented in the literature, like these established for sandstone:

McNally (Australia) [3]:

$$UCS = 1200 \cdot e^{(-0.036\Delta t)} \quad (3)$$

McNally (USA) [3]:

$$UCS = 1.4138 \cdot 10^{7} \Delta t^{-3} \quad (4)$$

Raaen et al. (North Sea) [4]:

$$UCS = 140 - 2.1\Delta t_p + 0.0083\Delta t_p^2 \quad (5)$$

Sharma and Sing [5]

$$UCS = 0.0642V_p - 117.99 \quad (6)$$

Freyburg (Germany) [6]

$$UCS = 0.035V_p - 31.5 \quad (7)$$

Moos et al. (Alaska) [7]

$$UCS = 1.745 \cdot 10^{-9} \rho V_p^2 - 21 \quad (8)$$

Chang et al. (Australia) [8]

$$UCS = 42.1 \cdot e^{(1.9 \cdot 10^{-11} \rho V_p^2)} \quad (9)$$

Chang et al. (Mexico) [8]

$$UCS = 3.87 \cdot e^{(1.14 \cdot 10^{-10} \rho V_p^2)} \quad (10)$$

Here Δt_p is given in μs/ft and UCS is given in MPa. The velocity V_P (= 304800/ Δt_p) is given in m/s, and ρ is given as 2.3 g/cm^3 [8]. Our results will be compared to these relations.

2. CORRELATIONS

2.1 Available data

The samples included in this work are restricted to sandstones from the Norwegian shelf, and were subjected to triaxial compression tests. Elastic moduli such as Young's modulus and Poisson's ratio, as well as peak stress were measured. Petrophysical measurements are also performed, including measurements of the porosity and bulk volume of the samples. Finally, the samples used in this study have been subjected to acoustic measurements.

Acoustic measurements usually include both P- and S-wave velocities. However, interpretation of the S-wave velocity is sometimes difficult since the arrival of the wave is often clouded by a low signal/noise ratio. For this reason, few S-wave velocity data are included here, and thereby give less correlation with petrophysical parameters and elastic moduli.

2.2 Sample Preparation

The samples used in this study all have similar preparation. The plugs were supplied from sets of seal peals, and were drilled parallel to their axis (i.e. vertically oriented). It is convenient to drill three plugs at the same depth of the seal peal axis, as this ensures homogeneous core samples and thus gives the best correlation when constructing the Mohr-Coulomb failure envelope. The plug end-surfaces were then ground plane and parallel according to ISRM-standard, and were adjusted to a length of approximately two times the diameter. The length and diameter of each sample was measured to be used for the calculations of deformation and axial stress. In addition to that the weight of each sample was measured, digital images were used to describe the failure mechanism of each plug.

Cleaning of the samples is essential to remove any residual hydrocarbons that may affect the petrophysical measurements on the plugs, but the cleaning itself may also affect the measurements. Due to this, there have been different trends regarding the question of cleaning the samples before the rock mechanical testing. Some of the samples used in this study have been subjected to a standard soxhlet cleaning with toluene and methanol, before they were dried in a heat cabinet and mercury (Hg) - bulk volume and helium (He) – porosity were measured. Other plugs have not been cleaned, but circulated with paraffin oil to remove the residuals of the heaviest hydrocarbon compounds. This is because some plugs are considered too fragile to be subjected to the standard cleaning procedure. There have not been observed any cleaning effect during the preparation of the plugs.

2.3 Triaxial compression test

This study utilizes data from samples that have been subjected to a standard triaxial compression test. All the samples mentioned in this study have been tested at drained conditions, with a pore pressure of 0.5 MPa for the most recent studies and 1.0 MPa for studies performed several years ago. Pore volume change is also measured, this by connecting the pore pressure system to a volume gauge.

The plugs are then loaded up to a predetermined hydrostatic load value, at a loading rate of about 1.0 MPa/minute. Further on the plugs are unloaded hydrostatically to a low load value, before they are reloaded and subjected to hydrostatic consolidation for 30-60 minutes. Finally the samples are axially compressed with an axial deformation rate of normally 10 mStrain/hour, until clear failure is observed or 20 mStrain axial strain is obtained.

Acoustic velocities are measured in the axial direction of the sample, with either P-wave or S-wave transducers. P-wave transducers were common several years ago, before S-wave transducers became standard, as it was discovered that the arrival of P-waves could also be seen with S-wave transducers. The arrival of the S-wave acoustics is sometimes difficult to interpret, and therefore P-wave velocities are more frequently found in the data available. It is also essential that the signal/noise ratios are high enough to be able to interpret the wave traces to determine the velocities.

2.4 Calculations

The dataset we have available here consists of tests performed at various confining pressures. To be able to compare the tests, we first establish models for the various parameters as functions of confining pressure. The coefficient of determination R^2 is given for each plot in the figure text.

For the peak stress $\sigma_{\max}$ we choose a model based on the Mohr-Coulomb criterion:

$$\sigma_{\max} = A + \sigma_C B \qquad (11)$$

The parameters *A* and *B* are assumed to be functions of the porosity φ and the dynamic stiffness $x_P = \rho\left(\Delta t_P\right)^{-2}$

Fig. 1 shows the best fit between Eq. (11) and the observed peak stress, with the following expressions for *A* and *B*:

$$A = -31.1\phi + 223x_P \qquad (12)$$

$$B = 1.32 + 0.77\phi - 0.40x_P \qquad (13)$$

The porosity is given in fractions and x_P is given in g cm^{-3} cm^2 μs^{-2}.

Based on the calibrated model for the strength (Eqs. (11) – (13)), we may now estimate UCS for each of the tested samples. Fig. 2 shows the results plotted as functions of the compressional transit time Δt_P. The trendline plotted in the figure is the best fit for an exponential function, and is given as

$$UCS = 1198 \cdot e^{-0.035\Delta t_P} \qquad (14)$$

Δt_P is given in μs/ft and *UCS* in MPa. As an indication of the quality of fit for this empirical function, we notice that the product of the coefficients of determination for the two steps involved is $R_1^2 R_2^2 = 0.56$.

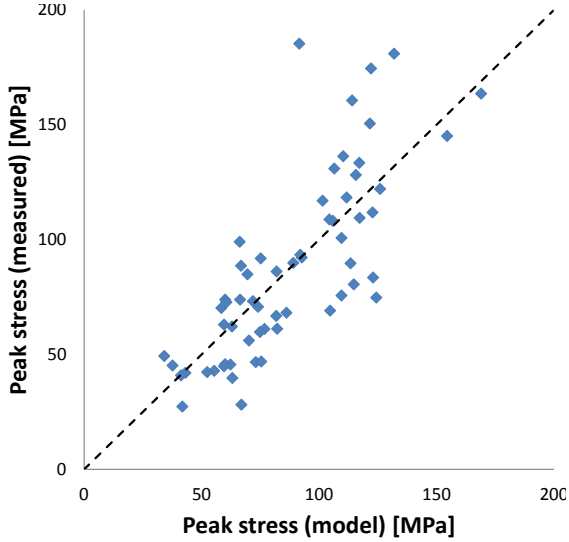

Fig. 1. Measured peak stress versus modeled peak stress estimated from porosity and dynamic stiffness. $R_1^2 = 0.61$.

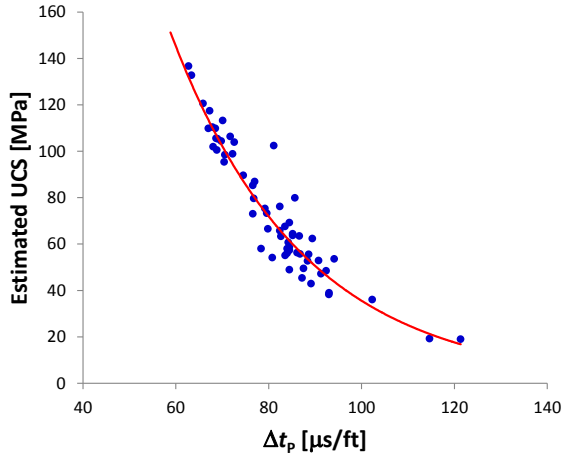

Fig. 2. Estimated unconfined compressive strength (UCS) versus compressional transit time. $R_2^2 = 0.91$.

The same procedure is used for the shear wave data. Fig. 3 shows the best fit between Eq. (11) and the observed peak stress, with the following expressions for A and B:

$$A = -7.97 - 133\phi + 398x_S \qquad (15)$$

$$B = -7.38 + 31.9\phi \qquad (16)$$

where $x_S = \rho\left(\Delta t_S\right)^{-2}$ is the dynamic shear stiffness, given in g cm^{-3} cm^2 μs^{-2}.

Fig. 4 shows the results plotted as functions of the shear transit time Δt_S. The trendline plotted in the figure is the best fit for an exponential function, and is given as

$$UCS = 426 \cdot e^{-0.015\Delta t_S} \qquad (17)$$

Δt_S is given in μs/ft and UCS in MPa, and $R_1^2 R_2^2 = 0.64$.

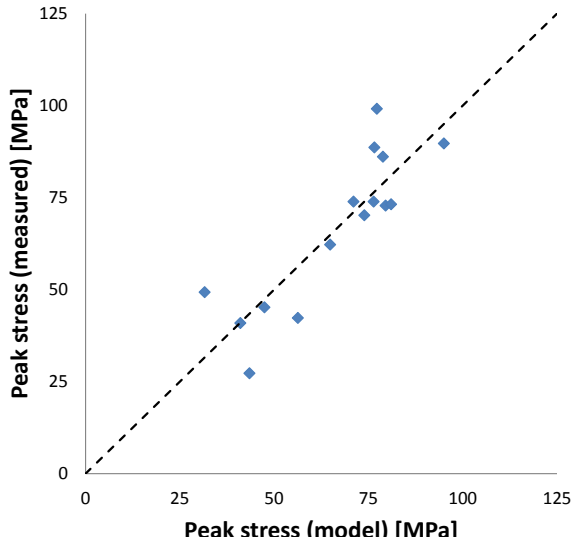

Fig. 3. Measured peak stress versus modeled peak stress estimated from porosity and dynamic shear stiffness. $R_1^2 = 0.74$.

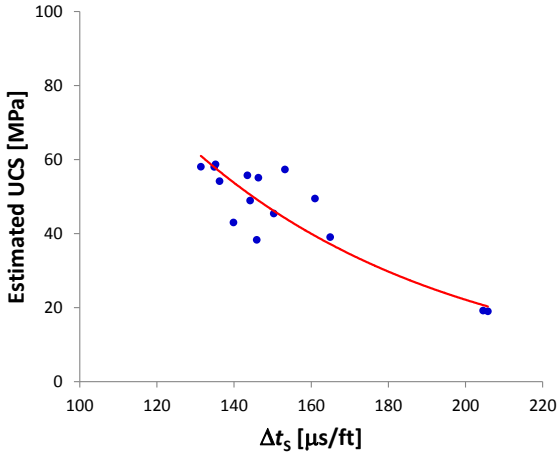

Fig. 4. Estimated unconfined compressive strength (UCS) versus shear transit time. $R_2^2 = 0.86$.

The following model was used for Young's modulus as function of confining pressure and dynamic stiffness:

$$E = 7.2 - 17.7x_P + 0.129\sigma_C + 115x_P^2 + 0.0074\sigma_C^2 - 1.57x_P\sigma_C \quad (18)$$

Fig. 5 shows the match between the modeled Young's modulus at zero confining pressure based on Eq. (18) and the measured Young's modulus.

Fig. 6 shows the estimated Young's modulus based on Eq. (18) as function of the compressional transit time Δt_P. The trendline plotted in the figure is given as

$$E = 9926\left(\Delta t_P - 38.1\right)^{-1.73} \quad (19)$$

Δt_P is given in μs/ft and E in GPa, and $R_1^2 R_2^2 = 0.51$.

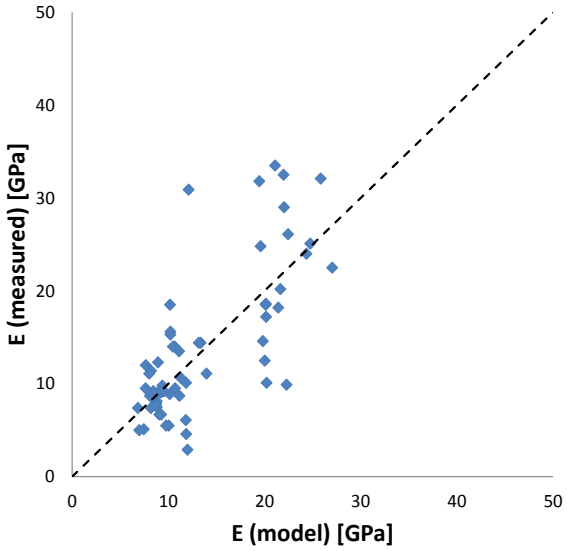

Fig. 5. Measured Young's modulus versus modeled Young's modulus estimated from porosity and dynamic stiffness. $R_1^2 = 0.55$.

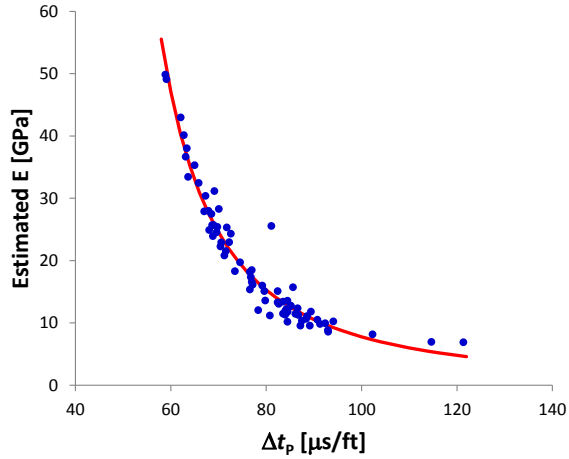

Fig. 6. Estimated Young's modulus at zero confining pressure versus compressional transit time. $R_2^2 = 0.93$.

The model used for Young's modulus as function of confining pressure and dynamic shear stiffness is given as:

$$E = 3.84 + 1061x_S^2 + 0.0062\sigma_C^2 - 2.73x_S\sigma_C \quad (20)$$

Fig. 7 shows the match between the modeled Young's modulus at zero confining pressure based on Eq. (20) and the measured Young's modulus.

Fig. 8 shows the estimated Young's modulus based on Eq. (20) as function of the shear transit time Δt_S. The trendline plotted in the figure is given a

$$E = 170\left(\Delta t_S - 107.4\right)^{-0.716} \quad (21)$$

Δt_S is given in μs/ft and E in GPa, and $R_1^2 R_2^2 = 0.73$.

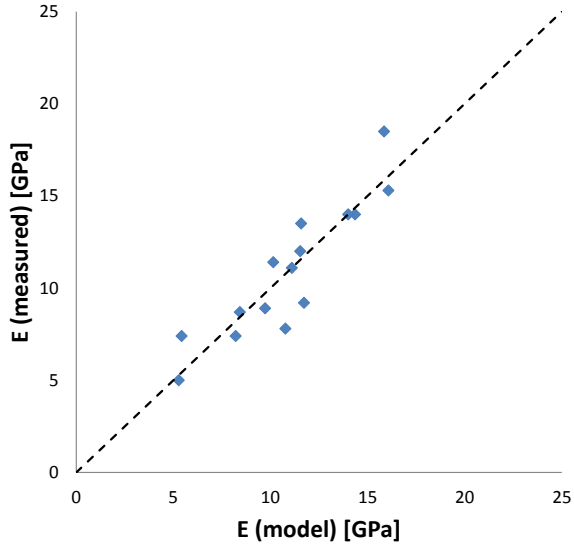

Fig. 7. Measured Young's modulus versus modeled Young's modulus estimated from porosity and dynamic shear stiffness. $R_1^2 = 0.82$.

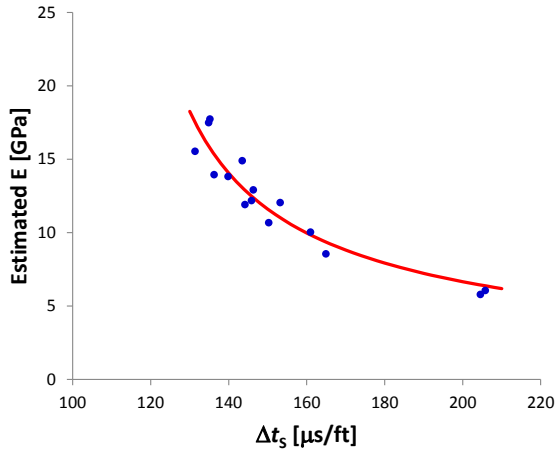

Fig. 8. Estimated Young's modulus at zero confining pressure versus shear transit time. $R_2^2 = 0.89$.

For Poisson's ratio as function of confining pressure and dynamic stiffness we tried among others the model:

$$\nu = 0.0089 + 0.811x_P + 0.0152\sigma_C - 0.0002\sigma_C^2 - 0.041x_P\sigma_C \quad (22)$$

Fig. 9 shows the match between the modeled Poisson's ratio at zero confining pressure based on Eq. (22) and the measured Poisson's ratio. Clearly, there is no match between the model and the measurements, as confirmed by the R^2 parameter. No trendline for Poisson's ratio versus compressional transit time was therefore established.

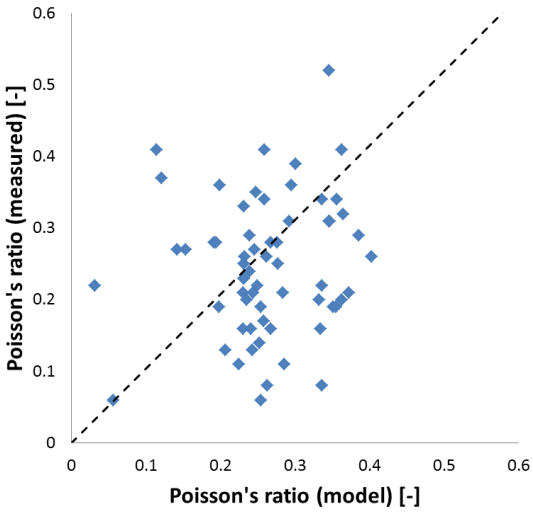

Fig. 9. Measured Poisson's ratio versus modeled Poisson's ratio estimated from porosity and dynamic stiffness. $R_1^2 = 0.02$.

The model used for Poisson's ratio as function of confining pressure and dynamic shear stiffness is given as:

$$\nu = 1.44 - 26.4x_S - 0.055\sigma_C + 135x_S^2 - 0.00067\sigma_C^2 + 0.755x_S\sigma_C \quad (23)$$

Fig. 10 shows the match between the modeled Poisson's ratio at zero confining pressure based on Eq. (23) and the measured Poisson's ratio.

Fig. 11 shows the estimated Poisson's ratio based on Eq. (23) as function of the shear transit time Δt_S. The trendline plotted in the figure is given as

$$\nu = 1.40 - 0.0188\Delta t_S + 7.1\cdot 10^{-5}\Delta t_S^2 \quad (24)$$

Δt_S is given in μs/ft, and $R_1^2 R_2^2 = 0.63$.

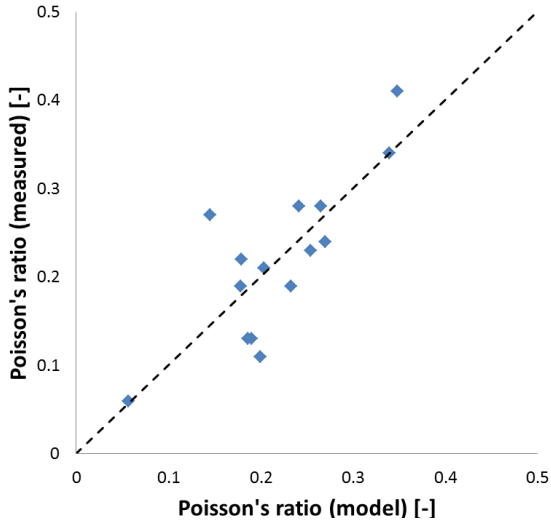

Fig. 10. Measured Poisson's ratio versus modeled Poisson's ratio estimated from porosity and dynamic shear stiffness. $R_1^2 = 0.65$.

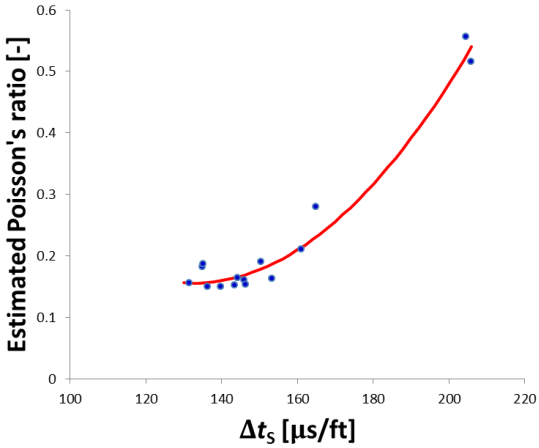

Fig. 11. Estimated Poisson's ratio at zero confining pressure versus shear transit time. $R_2^2 = 0.97$.

2.4 Evaluation of data points

A number of two plugs have been removed from the original data set after evaluation of the rock mechanical reports provided by the laboratory.

One plug has been removed due to the fact that the lithological description shows heterogeneity on this plug, while other plugs from the same seal peal show homogeneity. Observations on the plug after testing show that the measurements are most likely affected by this heterogeneity.

The peak stress of another plug has been removed, as this plug showed a special fracture phenomenon where the radial deformation after failure is positive (reduction of diameter). The measured peak stress on this plug is significantly lower than those measured on plugs from the same seal peal.

3. DISCUSSION

The results presented in Figs. 2, 4, 6, 8 and 11, and in Eqs. (14), (17), (19), (21) and (24), appear to have a very high degree of confidence if we consider the good concentration of the data points shown in the figures. However, it is important to keep in mind that the data points shown in these figures are not the real measurements, but rather estimates based on the models used to project all data to the same confining pressure. The quality of these estimates depend on the match between the observations and the models, as shown in Figs. 1, 3, 5, 7, and 10, hence the quality of the derived relations should be judged on the basis of both steps in the derivation. The product of the coefficients of determination for the two steps, $R_1^2 R_2^2$, is presented as an indication of the quality of fit since this product includes both steps. The importance of accounting for both steps is particularly evident for the relation for Young's modulus as a function of compressional transit time (Eq. (19)). Judged only from Fig. 6 this appears to be a highly reliable relation ($R_2^2 = 0.93$), however the match between model and observation displayed by Fig. 5 is rather poor ($R_2^2 = 0.55$), hence the validity of Eq. (19) is in fact questionable. For the rest of the relations the match is better, and the relations can be considered to have a reasonable credibility. In Figs. 11 an upper limit of 0.5 for Poisson's ratio has not been set, as it is not given that this material is linear elastic and isotropic.

Comparing the results for UCS with relations available in the literature, we notice first of all that Eq. (14) is almost identical to the relation (Eq. (3)) presented by McNally [3] for rocks from the Bowen

Basin (Australia). Fig. 12 shows the data given in Fig. 2, together with the relations for UCS as a function of compressional transit time presented in Chapter 1. Our data are seen to fall in the middle of the range spanned by the various published relations.

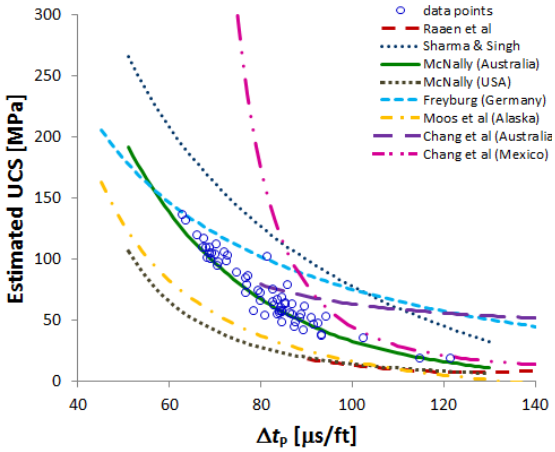

Fig. 12. Estimated unconfined compressive strength versus compressional transit time from this study, compared to a set of published relations for sandstone.

4. CONCLUSIONS

A set of empirical correlations, between unconfined compressive strength and compressional- and shear transit time, between Young's modulus and compressional- and shear transit time, and between Poisson's ratio and compressional- and shear transit time, have been established for a set of sandstones from the North Sea area. The quality of the relations vary somewhat but the trends are generally as expected.

A comparison between the strength data obtained in this study and a set of empirical correlations available in the literature shows that our data falls in the middle of the range spanned by the published relations. The best fit for an exponential trendline through our data matches almost exactly the empirical correlation derived by McNally [3] for a set of sandstones from Australia.

Acknowledgements

We would like to express our appreciation to Statoil and Weatherford Laboratories for the opportunity to publish this study.

NOMENCLATURE

ρ = Bulk density [g/cm^3]

φ = Porosity [frac.]

V_P = Compressional velocity [m/s]

Δt_p = Compressional transit time [μs/ft]

Δt_s = Shear transit time [μs/ft]

UCS = Unconfined compressive strength [MPa]

σ_C = Confining pressure [MPa]

REFERENCES

1. Nes, O.-M., P. Horsrud, E. F. Sonstebo, R. M. Holt, A. M. Ese, D. Okland and H. Kjorholt. 1996. Rig site and laboratory use of CWT acoustic velocity measurements on cuttings. *The 1996 SPE European Petroleum Conference, Milan, Italy, 22-24 October 1996.* SPE 50982.
2. Ringstad, C., E. B. Lofthus, E. F. Sonstebo, E. Fjaer, F. Zausa and G.-F. Fuh. 1998. Prediction of rock parameters from micro-indentation measurements: The effect of sample size. *SPE/ISRM Rock Mechanics in Petroleum Engineering, Trondheim, Norway, 8-10 July 1998.*
3. McNally, G.H. 1987. Estimation of coal measures rock strength using sonic and neutron logs. Geoexploration. 24. 381-395.
4. Raaen, A.M., K.A. Hovem, H. Jøranson and E. Fjær. 1996. FORMEL: A step forward in strength logging *The 1996 SPE Annual Technical Conference and Exhibition, Denver*. SPE 36533.
5. Sharma, P.K. and T.N. Singh. 2008. A correlation between P-wave velocity, impact strength index, slake durability index and uniaxial compressive strength. Bulletin of Engineering Geology and the Environment. 67. 17-22.
6. Freyburg, E. 1972. Der Untere und mittlere Buntsandstein SW-Thuringen in seinen gesteinstechnicschen Eigenschaften Berlin, Deustche Gesellschaft Geologische Wissenschaften. A; Berlin 176. 911-919.
7. Moos, D., M.D. Zoback and L. Bailey. 1999. Feasibility study of the stability of openhole multilaterals, Cook Inlet, Alaska. *The 1999 SPE Mid-Continent Operations Symposium, Oklahoma City, Oklahoma, 28-31 March 1999.* SPE 52186.
8. Chang C., M. D. Zoback and A. Khaksar. 2006. Empirical relations between rock strength and physical properties in sedimentary rocks. Journal of Petroleum Science. Eng 51. 223-237.

B. Laboratory equipment/methods

This is a synopsis of the Laboratory Manual for Weatherford Laboratories, Norway. This Laboratory Manual is the work by Karl Tokle.

This is a general description, and therefore it may contain part which may not be relevant to this study.

B.1 Triaxial cell

The triaxial cell can take 1 1/2”-plugs and is designed by RockMech A/S (Figure B-1). The cell is made of stainless steel (SIS 2324). The design pressure is 70 MPa. The cell can also be used for permeability measurements during triaxial loading. There are openings in the piston and the bottom plate for circulating pore fluid. Disks of stainless steel with concentric grooves and holes are used to distribute the fluid flow before entering the sample. The fluid can be oil, formation water or weak acid (5% HCl). Gas can also be used.

For measuring radial deformation there are 3 symmetrical (120 deg) openings in the cell wall where spring loaded pins "feel" the surface of the core or the core holder. 3 cylinders contain the transducers which measure the position of the pin (Figure B-2). The transducers are so called "Linear Variable Displacement Transformers" (LVDT) produced by Schaevitz, type 250 MHR. The transducers have a nominal stroke of 0.25” (6.35 mm). Accuracy, see section B-7.

Correction for deformations in the cell during hydrostatic loading is done automatically during logging. This correction has been measured by putting a 1.5” diameter steel plug in the cell, and gradually increasing the confining pressure to 30 MPa while logging pressure and radial deformation. The deformations of the steel plug are taken as negligible. At 30 MPa confining pressure the measured deformation was 2.3 mStrain. During hydrostatic loading the average radial deformation is subtracted by $(2.3/30)p$ mStrain, where p is the confining pressure. This correction will not apply in the triaxial phase, since the confining pressure then is constant and the radial deformation is zeroed when entering the triaxial phase.

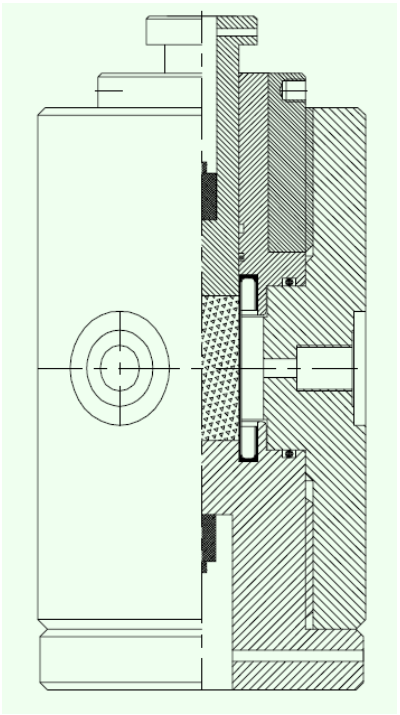

Figure B-1. Triaxial cell.

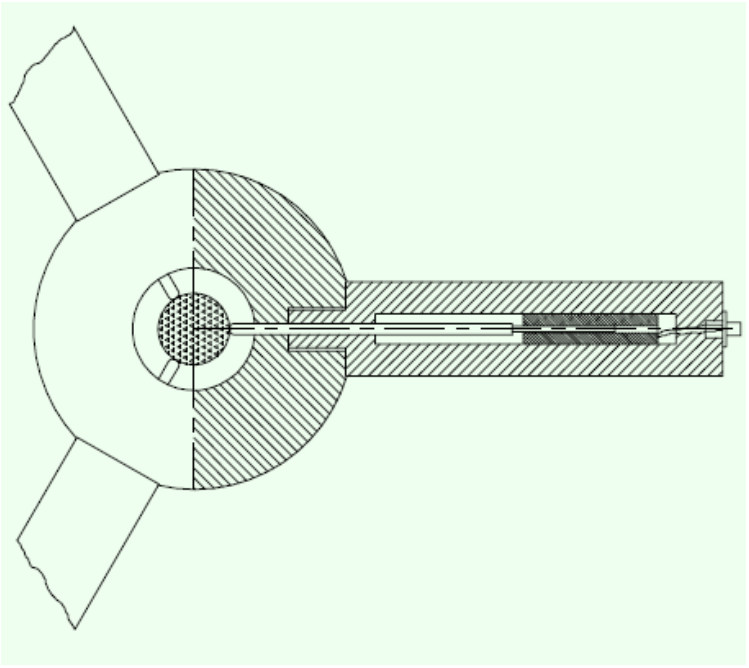

Figure B-2. Triaxial cell with radial deformation transducer.

B.2 Axial load system

A servo-hydraulic loadframe with a capacity of 300 kN is used, see Figure B-3. The servo-hydraulic cylinder can operate either in load control or in displacement control. During displacement control the rate can vary from 0.0001 to 9.9 mm/s. The load frame is designed by RockMech A/S and produced by A/S Delprodukt. The servo-hydraulic cylinder and the pump-unit are supplied by Robcon OY, Finland.

In 1998 a new digital control system was installed. This makes it possible to perform bumpless transfer from the load control to the deformation control. The control electronics was supplied by Instron, England.

Axial deformation of the sample during testing is measured by means of an LVDT, Schaevitz GCA-121-250. The transducer has a nominal stroke of 0.25 inches (6.35 mm). Accuracy, see section B-7. The transducer is mounted on the top plate of the load frame and measures the displacement of the piston of the servo-hydraulic cylinder.

Corrections for deformations in the loadframe, loadcell, servo-hydraulic piston and piston in the triaxial cell are done automatically during datalogging. This correction is based on the same procedure as for correction of radial deformation.

Axial load is measured by a load cell manufactured by HBM, type C3H2. The nominal load is 300 kN. Accuracy, see section B-7.

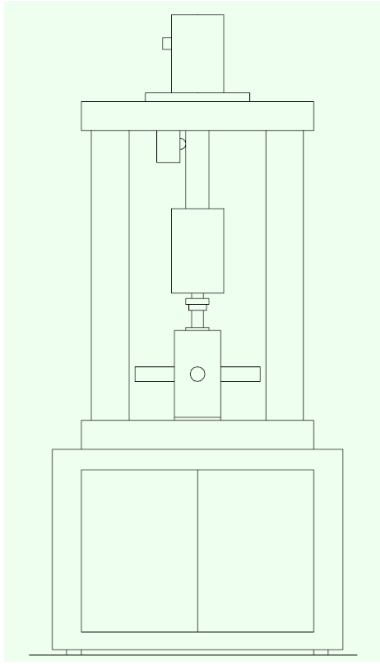

Figure B-3. Axial load system.

B.3 Confining pressure system

The confining pressure system is shown in Figure B-4. A radial piston pump with a capacity of 100 MPa and a constant flow rate of 0.5 l/min is used to obtain the predetermined confining pressure. The pump is manufactured by BIERI, type RP12. The system is divided in two parts; one high pressure, 3-70 MPa, and a low pressure, 1-30 MPa. The pressure is controlled by proportional valves in both parts. The valves and control electronics are manufactured by Wandfluh. The valves can be controlled either manually with a potentiometer or remotely by an analogue signal from the computer. Under computer control the system utilizes closed loop control and the static accuracy of the confining pressure is better than ±0.1 MPa.

The confining pressure is measured with a pressure transducer manufactured by HBM, type P6 0-100 MPa. Accuracy, see section B-7.

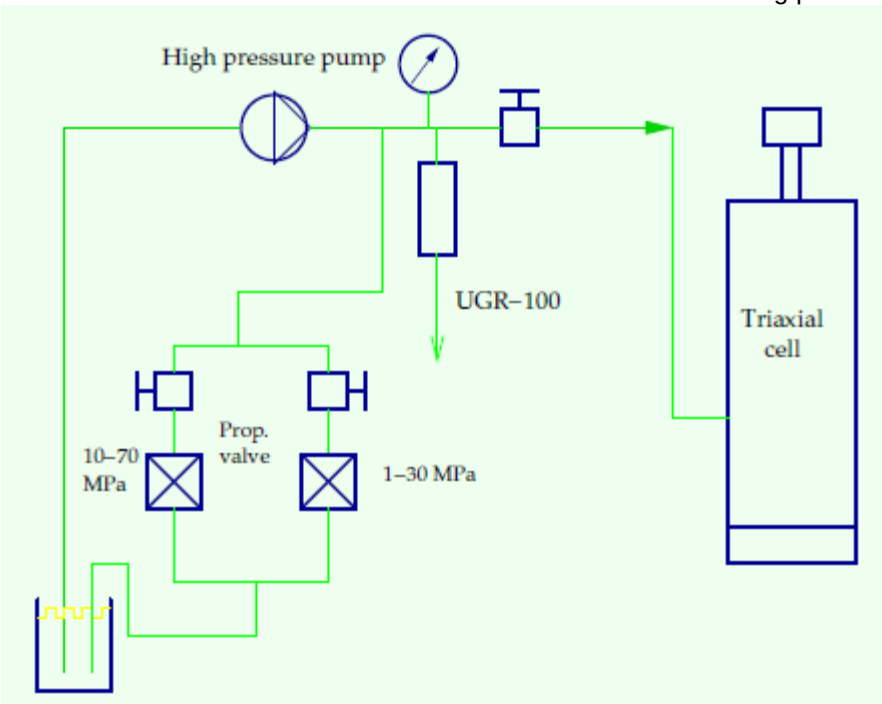

Figure B-4. Confining pressure system.

B.4 Characteristics of failure modes during uniaxial and triaxial compressive testing

In the following section, a brief description of the material responses of the rocks and the typical stress-strain curves, shown in Figure B-5, are given.

MODE 1, Elastic – very brittle: This is a rock that is very hard and when it fails it releases a lot of energy that has been building up in the sample and the testing machine. The failure is normally very violent and it loses all load carrying capacity after the failure. In Figure B-5 is shown a marginal very small stress that can be carried, but in 9 out of 10 times there is no strength left.

MODE 2, Elastic – moderately brittle: This is a hard rock that also will fail violently, but this rock will not collapse totally, but will retain some of its load carrying capacity, even after the failure took place. If the rock transform into an ideal plastic rock after failure this means the sample can continue to deform without any change in effective axial stress.

MODE 3, Elastic–plastic (work softening): This is a mode of failure that is most often seen in sedimentary rocks. In this stress-strain curve there is an initial non-linear elastic part, a linear elastic part, a yielding part to the peak stress is reached. Then the sample reduces the peak stress rapidly to a residual stress. At this stage the sample will deform nearly ideally plastically till the experiment is stopped. In some instances the stress will start to increase after the drop to residual stress due to work weakening. This means that the sample most likely start to reduce volume due to pore collapse.

MODE 4, Elastic–ideal plastic: This sample will show a linear elastic response until it reaches the Yield point. At this stage the sample starts to move like a heavy fluid, and there is no stress increase after this point is reached; – the sample deforms ideally plastic.

MODE 5, Elastic–plastic (work hardening): This rock will show linear elastic response up to the Yield point (YP), and after the YP the sample will show increasing stress as deformation increases. This is a sample that undergoes pore collapse and a continuous pore volume reduction. If the volumetric strain is plotted versus the axial strain this will give a continuously increasing positive volumetric strain; i.e. the sample volume is continuously reduced.

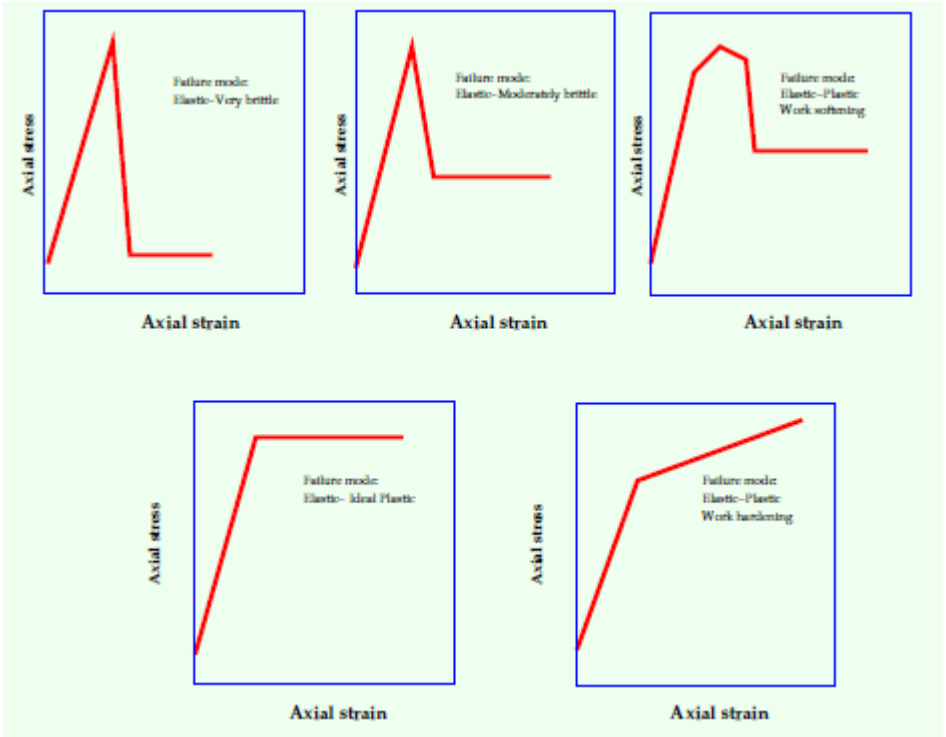

Figure B-5. Failure modes during uniaxial and triaxial testing.

Final comments to the failure modes: A typical characteristic of rocks is that that the same rock shows different behavior, dependent on the effective confining stress it is under.

At low effective confining stress most samples will show a very brittle to moderately brittle mode of failure. If the effective confining stress is increased the sample tends towards the elastic–plastic mode of failure, and at high effective confining stresses the sample will show ideal plastic and work hardening behavior.

This means that a rock has different behavior, dependent on the stress state it is influenced by.

Therefore it is very important to determine the rock and its behavior as early as possible in the field development. This will indicate what stress changes can be tolerated and how the rock will respond to planned depletions or injection campaigns.

B.5 Interpretation of elastic parameters and strength data

Elastic parameters are interpreted as shown in Figure B-6. Linear regression is used to find the best fit. The same range is used for the radial deformation and the same method when calculating Poisson's ratio.

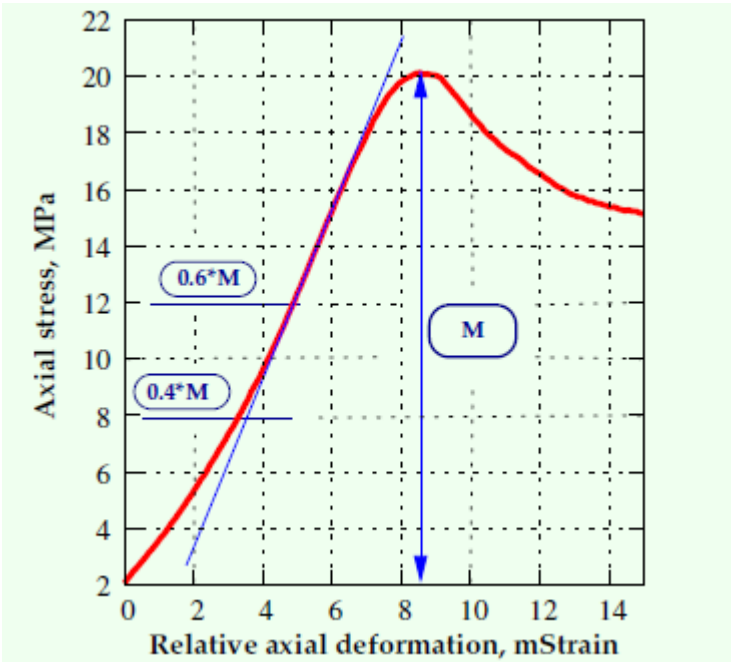

Figure B-6. Interpretation of elastic parameters.

Abnormal failure envelope: In order to obtain a failure envelope three or more samples are tested with different confining pressure. Ideally these three or more samples should have the same rock mechanical properties with respect to strength. The peak stress will normally increase with confining pressure when the samples have the same rock mechanical properties.

When the amount of core material are limited (slabbed seal-peels or fragile materials) it will be necessary to drill vertical samples from different depth. In heterogeneous materials this can results in 3 or more sample with different rock mechanical properties. Figure B-7 is an example of 3 samples having different rock mechanical properties and the results is an abnormal failure envelope. In this case is it not possible to calculate the failure parameters (failure angle, friction angle, cohesion and uniaxial compressive strength).

Strength data are calculated using Coulomb-theory, as shown in Figure B-8. Several straight lines are used, with their own range of validity.

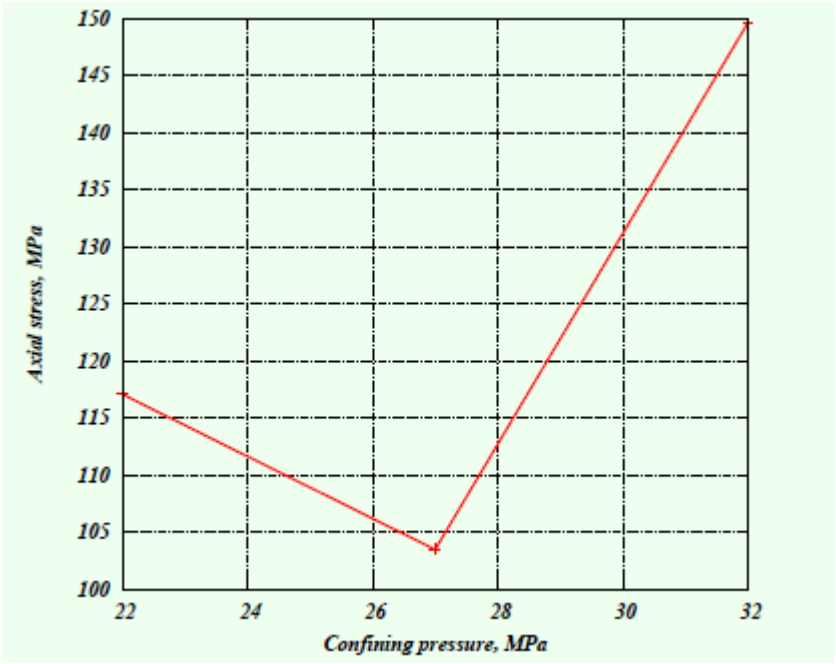

Figure B-7. Abnormal strength of samples from same depth.

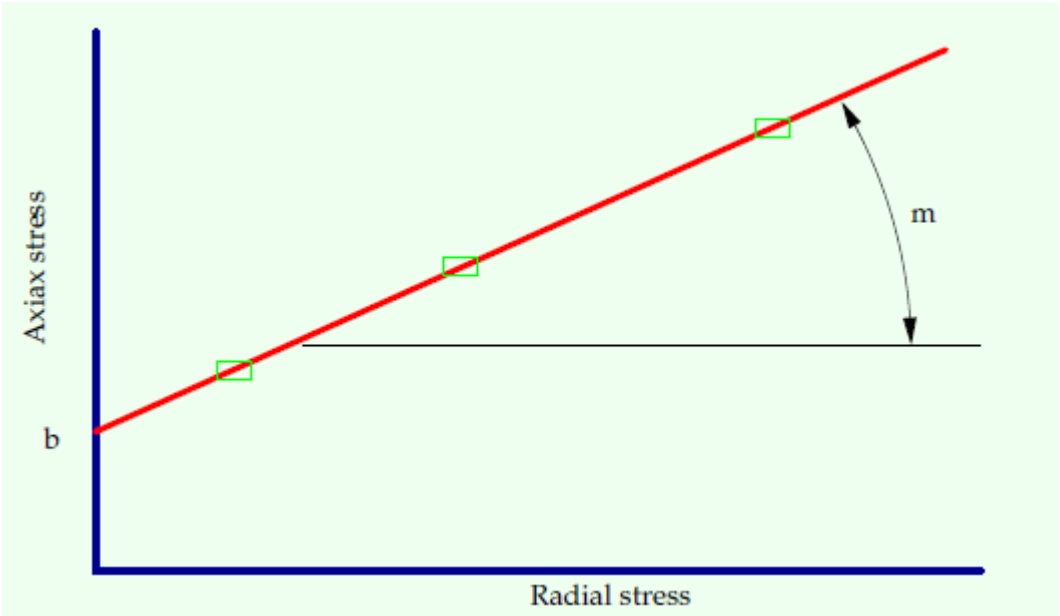

Figure B-8. Interpretation of strength data.

The various constants are:

b	=	C_0 = uniaxial compressive strength
m	=	$\tan^2\alpha$
α	=	failure angle
φ	=	friction angle
φ	=	2 (α - 45)
C_0	=	2 S_{c0} tanα
S_{c0}	=	cohesion

The following two sections apply only when liquid permeability or compressibility have been measured.

B.6 Brazil test

This method is based on "Suggested Methods for Determining Tensile Strength of Rock Materials" given by ISRM. Part 2 of this document describes an indirect method to measure the uniaxial tensile strength of prepared rock specimens called the Brazil test. The justification for the test is based on the experimental fact that most rocks in biaxial stress field fail in tension at their uniaxial tensile strength when one principal stress is tensile and the other finite principal stress is compressive with a magnitude not exceeding three times that of the tensile principal stress.

The test equipment is shown in Fig. A.12 Specimens of 1.5” diameter is cut to a length of 24 mm. The specimen are loaded at a rate about 0.2 kN/s. The force and displacement are recorded by the computer. From the curve of load vs. displacement the force at primary fracture is read.

The tensile strength of the specimen, σ_t, is calculated using the following formula (Eq. (B-1)):

$$\sigma_t = \frac{0.636 \cdot P}{D \cdot t} \qquad \text{(B-1)}$$

Where

P	-	load at failure, N
D	-	diameter of the test specimen, mm
t	-	thickness of the test specimen, mm
σ_t	-	tensile strength, MPa

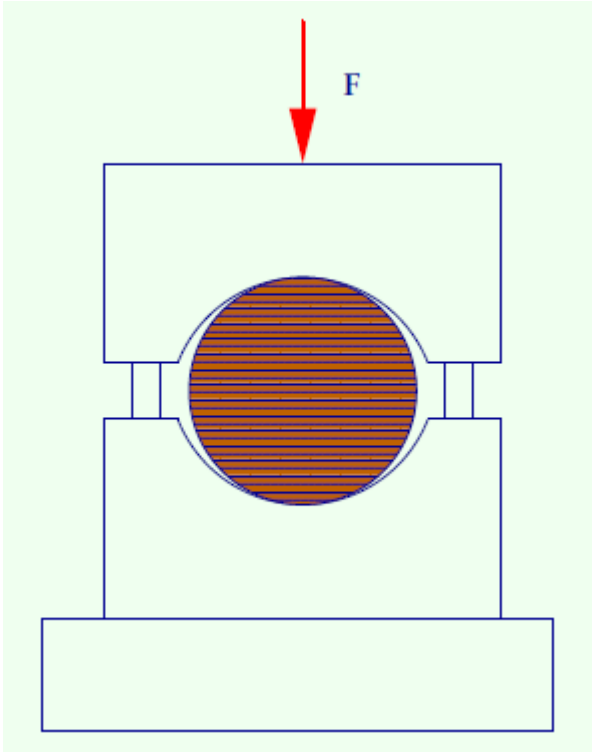

Figure B-9. Brazil testing equipment for measuring tensile strength.

B.7 Sonic velocity

Sonic wave propagation in sedimentary rocks has become an important instrument in the characterization of the rock. Sonic data are logged routinely in boreholes. Extensive research is taking place in order to correlate sonic properties and mechanical properties of rocks. Methods for in-situ stress prediction based on sonic measurements have also been presented. With this background we have seen the need for being able to offer such measurements routinely. So far we have limited this to axial measurement of P-waves and S-wave measurements. A schematic figure of the set-up is shown in Figure B-10.

The system consists of:

• modified piston and bottom plate in the triaxial cell

• contact transducers, 1.0 MHz (Panametrics)

• broadband ultrasonic pulser/receiver (Panametrics). This generates high-amplitude and short electric pulses to the transmitting transducer. The signal from the receiving transducer is amplified and sent to an oscilloscope.

• digital storage oscilloscope (Tektronix TDS 210), 60 MHz with 1 GHz sampling frequency and two channels. We use a PC for storage of the full wave trains.

An S-wave type of transducer is used. This implies that the transducer is mainly tuned for shear waves. In most cases the P-wave (compressional) velocity can also be interpreted.

The client will get the wave trains on diskette, CD or by mail. Normal sampling rate is every 5 MPa in the hydrostatic phase of the test, and every 1.0 mStrain in the triaxial phase.

Sonic velocity can under triaxial conditions be measured on samples of 1.5" (38 mm) diameter. Without the triaxial cell sonic velocity can be measured on any sample diameter and length up to 250 mm.

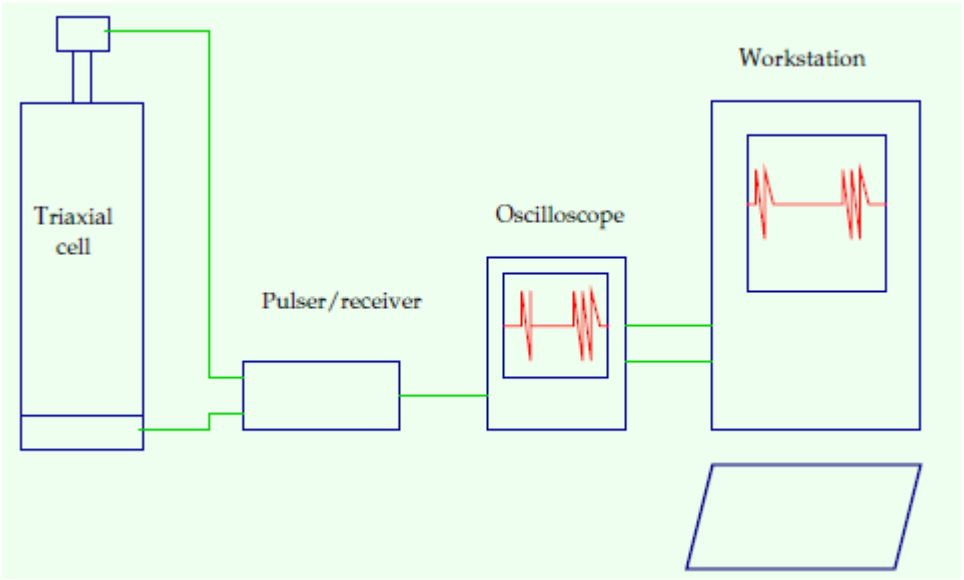

Figure B-10. Schematic of sonic velocity measurements.

B.8 Accuracy

The accuracy of the measuring equipment shown below includes an allowance for errors in the auxiliary equipment (measuring amplifiers, A/D-converter etc.)

The transducers for axial and radial deformation are calibrated against a digital micrometer, Mitutoyo type 164-151 0-50 mm. It is calibrated by Teknologisk Institutt, avdeling Verkstedteknikk, Verkstedteknisk Laboratorium which is traceable to international standards.

The transducer for axial force is calibrated by Nemko. Their load cells of 30, 100 and 1000 kN which are traceable to international standards.

The pressure transducers for the confining pressure and back (pore) pressure are calibrated using our own deadweight tester Budenberg type 3/480C which is traceable to international standards. The differential pressure is calibrated by A/S Fimas and is traceable to international standards.

• Axial force : in the range 0-10 kN the relative accuracy is ±0.7%. In the range 10-300 kN the relative accuracy is ±0.35%. The resolution is 0.1 kN in the range 100–300 kN, 0.01 kN in the range 10–100 kN and 0.001 kN in the range 1–10 kN.

• Confining pressure: relative accuracy better than ±0.35% in the range 7–70 MPa, biggest absolute deviation in the nominal range 0-70 MPa is 90 kPa, resolution 10 kPa.

• Axial deformation: non-linearity better than ±13 micrometer, resolution 1 micrometer.

• Radial deformation: non-linearity better than ±23 micrometer, resolution 1 micrometer.

• Differential pressure (for liq. perm.): relative accuracy better than ±1.6%, biggest absolute deviation in the nominal range 0-100 kPa is 0.6 kPa, resolution 0.1 kPa

• Differential pressure (for gas. perm.): relative accuracy better than ±1%,

• Back (pore) pressure: relative accuracy better than ±0.35% in the range 1-50 MPa, biggest absolute deviation in the nominal range 0-50 MPa is 20 kPa, resolution 10 kPa

• Liquid flowrate: relative accuracy ±1%

• Gas flowrate: relative accuracy ±1%

C. R codes

For the statistical analysis presented in chapter 6, the open source programming language and software environment for statistical computing and graphics, R, was used.

The programming codes for all three parameters, both for P-waves and S-waves are listed below.

C.1 Peak stress (P-waves)

```
function (data=rmdata)

{

windows()

par(mfrow=c(4,2))

true<-peak.true

model<-peak.Vp.model

conf0<-A.Vp

smat<-rmdata[order(rmdata[,"Dt.Vp"]),]

x<-smat[,"Dt.Vp"]

conf0<-smat[,"A.Vp"]

plot(model,true,xlim=c(0,200),ylim=c(0,200),xlab="Peak stress (model)[MPa]",
ylab="Peak stress (measured) [MPa]")

abline(a=0,b=1,lty="dotted",col="lightblue")

linje<-1198.2*exp(-0.035*x)

tips<-cbind(linje,conf0)

tips<-as.matrix(na.omit(tips))

tips2<-cbind(smat[,"peak.Vp.model"],smat[,"peak.true"])

tips2<-as.matrix(na.omit(tips2))

residuals<-tips[,1]-tips[,2]

feil<-tips2[,1]-tips2[,2]

qstd<-quantile(residuals,c(0.025,0.975))

linjelav<-linje+qstd[1]

linjehoy<-linje+qstd[2]

plot(x,conf0,col="red",xlab=paste("\u0394","t(p)    [µs/ft]"),ylab="Estimated
UCS [MPa]")

lines(x,linje,col="red")

lines(x,linjelav,col="blue")

lines(x,linjehoy,col="blue")
```

```
plot(smat[-16,"peak.true"],feil,xlab="Peak    stress    (measured)    [MPa]",
ylab="Peak stress (model - measured)")

plot(x,linjehoy-linjelav,xlab=paste("\u0394","t(p)        [µs/ft]"),ylab="95%
confidence interval")

hist(feil,main="Histogram",xlab="Peak stress (mod - meas) [MPa]")

hist(residuals,main="Histogram",xlab="Estimated UCS - fitted line")

abline(v=qstd,col="red",lwd=2)

qqnorm(feil)

qqnorm(residuals)

svar<-cbind(sd(feil),sd(residuals))

return(svar)

}
```

C.2 Peak stress (S-waves)

```
function (data=rmdata)

{

windows()

par(mfrow=c(4,2))

true<-peak.true

model<-peak.Vs.model

conf0<-A.Vp

smat<-rmdata[order(rmdata[,"Dt.Vs"]),]

x<-smat[,"Dt.Vs"]

conf0<-smat[,"A.Vp"]

plot(model,true,xlim=c(0,125),ylim=c(0,125),xlab="Peak stress(model) [MPa]",
ylab="Peak stress (measured) [MPa]")

abline(a=0,b=1,lty="dotted",col="lightblue")

linje<-425.68*exp(-0.015*x)

tips<-cbind(linje,conf0)

tips<-as.matrix(na.omit(tips))

tips2<-cbind(smat[,"peak.Vs.model"],smat[,"peak.true"])

tips2<-as.matrix(na.omit(tips2))

residuals<-tips[,1]-tips[,2]

feil<-tips2[,1]-tips2[,2]

qstd<-quantile(residuals,c(0.025,0.975))

linjelav<-linje+qstd[1]

linjehoy<-linje+qstd[2]

plot(x,conf0,col="red",xlim=c(100,220),ylim=c(0,100),xlab=paste("\u0394",
"t(s)[µs/ft]"),ylab="Estimated UCS [MPa]")

lines(x,linje,col="red")

lines(x,linjelav,col="blue")

lines(x,linjehoy,col="blue")
```

```
plot(smat[1:15,"peak.true"],feil,xlab="Peak     stress(measured)     [MPa]",
ylab="Peak stress (model - measured)")

plot(x,linjehoy-linjelav,xlab=paste("\u0394","t(s)       [µs/ft]"),ylab="95%
confidence interval")

hist(feil,main="Histogram",xlab="Peak stress(mod - meas) [MPa]")

hist(residuals,main="Histogram",xlab="Estimated UCS - fitted line")

abline(v=qstd,col="red",lwd=2)

qqnorm(feil)

qqnorm(residuals)

svar<-cbind(sd(feil),sd(residuals))

return(svar)

}
```

C.3 Young's modulus (P-waves)

```
function (data=rmdata)

{

windows()

par(mfrow=c(4,2))

true<-E.true

model<-E.Vp.model

conf0<-E.Vp.model.conf.0

smat<-rmdata[order(rmdata[,"Dt.Vp"]),]

x<-smat[,"Dt.Vp"]

conf0<-smat[,"E.Vp.model.conf.0"]

plot(model,true,xlim=c(0,50),ylim=c(0,50),xlab="Young's       modulus(model)
[GPa]",ylab="Young's (measured)  [GPa]")

abline(a=0,b=1,lty="dotted",col="lightblue")

linje<-9925.85*((x-38.09)^(-1.73))

tips<-cbind(linje,conf0)

tips<-as.matrix(na.omit(tips))

tips2<-cbind(smat[,"E.Vp.model"],smat[,"E.true"])

tips2<-as.matrix(na.omit(tips2))

residuals<-tips[,1]-tips[,2]

feil<-tips2[,1]-tips2[,2]

qstd<-quantile(residuals,c(0.025,0.975))

linjelav<-linje+qstd[1]

linjehoy<-linje+qstd[2]

plot(x,conf0,col="red",xlim=c(40,140),ylim=c(0,60),xlab=paste("\u0394","t(p)
[µs/ft]"),ylab=paste ("Estimated Young's(","\u03C3","(c)=0) [GPa]"))

lines(x,linje,col="red")

lines(x,linjelav,col="blue")

lines(x,linjehoy,col="blue")
```

```
plot(smat[,"E.true"],feil,xlab="Young's       modulus(measured)       [MPa]",
ylab="Young's(model - measured)")

plot(x,linjehoy-linjelav,xlab=paste("\u0394","t(p)        [µs/ft]"),ylab="95%
confidence interval")

hist(feil,main="Histogram",xlab="Young's modulus(mod - meas) [GPa]")

hist(residuals,main="Histogram",xlab=paste("Estimated     Young's     modulus
(","\u03C3","(c)=0) - fitted line"))

abline(v=qstd,col="red",lwd=2)

qqnorm(feil)

qqnorm(residuals)

svar<-cbind(sd(feil),sd(residuals))

return(svar)

}
```

C.4 Young's modulus (S-waves)

```
function (data=rmdata)

{

windows()

par(mfrow=c(4,2))

true<-E.true

model<-E.Vs.model

conf0<-E.Vs.model.conf.0

smat<-rmdata[order(rmdata[,"Dt.Vs"]),]

x<-smat[,"Dt.Vs"]

conf0<-smat[,"E.Vs.model.conf.0"]

plot(model,true,xlim=c(0,25),ylim=c(0,25),xlab="Young's       modulus(model)
[GPa]", ylab= "Young's (measured) [GPa]")

abline(a=0,b=1,lty="dotted",col="lightblue")

linje<-170.41*((x-107.35)^(-0.716))

tips<-cbind(linje,conf0)

tips<-as.matrix(na.omit(tips))

tips2<-cbind(smat[,"E.Vs.model"],smat[,"E.true"])

tips2<-as.matrix(na.omit(tips2))

residuals<-tips[,1]-tips[,2]

feil<-tips2[,1]-tips2[,2]

qstd<-quantile(residuals,c(0.025,0.975))

linjelav<-linje+qstd[1]

linjehoy<-linje+qstd[2]

plot(x,conf0,col="red",xlim=c(100,220),ylim=c(0,25),xlab=paste("\u0394",
"t(s) [µs/ft]"), ylab=paste ("Estimated Young's(","\u03C3","(c)=0) [GPa]"))

lines(x,linje,col="red")

lines(x,linjelav,col="blue")lines(x,linjehoy,col="blue")

plot(smat[1:15,"E.true"],feil,xlab="Young's   modulus   (measured)   [MPa]",
ylab="Young's(model - measured)")
```

```
plot(x,linjehoy-linjelav,xlab=paste("\u0394","t(s)        [µs/ft]"),ylab="95%
confidence interval")

hist(feil,main="Histogram",xlab="Young's modulus(mod - meas) [GPa]")

hist(residuals,main="Histogram",xlab=paste("Estimated     Young's     modulus
(","\u03C3","(c)=0) - fitted line"))

abline(v=qstd,col="red",lwd=2)

qqnorm(feil)

qqnorm(residuals)

svar<-cbind(sd(feil),sd(residuals))

return(svar)

}
```

C.5 Poisson's ratio (P-waves)

```
function (data=rmdata)

{

windows()

par(mfrow=c(4,2))

true<-ny.true

model<-ny.Vp.model

conf0<-ny.Vp.model.conf.0

smat<-rmdata[order(rmdata[,"Dt.Vp"]),]

x<-smat[,"Dt.Vp"]

conf0<-smat[,"ny.Vp.model.conf.0"]

plot(model,true,xlim=c(0,0.6),ylim=c(0,0.6),xlab="Poisson's ratio (model) [-]",ylab="Poisson's (measured) [-]")

abline(a=0,b=1,lty="dotted",col="lightblue")

linje<-97.11*((x-26.15)^(-1.46))

tips<-cbind(linje,conf0)

tips<-as.matrix(na.omit(tips))

tips2<-cbind(smat[,"ny.Vp.model"],smat[,"ny.true"])

tips2<-as.matrix(na.omit(tips2))

residuals<-tips[,1]-tips[,2]

feil<-tips2[,1]-tips2[,2]

qstd<-quantile(residuals,c(0.025,0.975))

linjelav<-linje+qstd[1]

linjehoy<-linje+qstd[2]

plot(x,conf0,col="red",xlab=paste("\u0394","t(p)                [my-sec/ft]"),
ylab=paste("Estimated Poisson's (","\u03C3", "(c)=0) [-]"))

lines(x,linje,col="red")

lines(x,linjelav,col="blue")

lines(x,linjehoy,col="blue")
```

```
plot(smat[,"ny.true"],feil,xlab="Poissons's    ratio(measured)[-]",    ylab=
"Poisson's(model - measured)")

plot(x,linjehoy-linjelav,xlab=paste("\u0394","t(p)    [my-sec/ft]"),ylab="95%
confidence interval")

hist(feil,main="Histogram",xlab="Poisson's ratio(mod - meas) [-]")

hist(residuals,main="Histogram",xlab=paste("Estimated    Poisson's    ratio
(","\u03C3","(c)=0) - fitted line"))

abline(v=qstd,col="red",lwd=2)

qqnorm(feil)

qqnorm(residuals)

svar<-cbind(sd(feil),sd(residuals))

return(svar)

}
```

C.6 Poisson's ratio (S-waves)

```
function (data=rmdata)

{

windows()

par(mfrow=c(4,2))

true<-ny.true

model<-ny.Vs.model

conf0<-ny.Vs.model.conf.0

smat<-rmdata[order(rmdata[,"Dt.Vs"]),]

x<-smat[,"Dt.Vs"]

conf0<-smat[,"ny.Vs.model.conf.0"]

plot(model,true,xlim=c(0,0.6),ylim=c(0,0.6),xlab="Poisson's ratio (model)
[-]",ylab= "Poisson's (measured) [-]")

abline(a=0,b=1,lty="dotted",col="lightblue")

linje<-1.4015-(0.0188*x)+(7.1*(10^(-5))*x*x)

tips<-cbind(linje,conf0)

tips<-as.matrix(na.omit(tips))

tips2<-cbind(smat[,"ny.Vs.model"],smat[,"ny.true"])

tips2<-as.matrix(na.omit(tips2))

residuals<-tips[,1]-tips[,2]

feil<-tips2[,1]-tips2[,2]

qstd<-quantile(residuals,c(0.025,0.975))

linjelav<-linje+qstd[1]

linjehoy<-linje+qstd[2]

plot(x,conf0,col="red",xlim=c(100,220),ylim=c(0,0.6),xlab=paste("\u0394",
"t(s)[µs/ft]"), ylab=paste ("Estimated Poisson's(","\u03C3","(c)=0) [-]"))

lines(x,linje,col="red")

lines(x,linjelav,col="blue")

lines(x,linjehoy,col="blue")
```

```
plot(smat[1:15,"ny.true"],feil,xlab="Poisson's ratio (measured) [-]",
ylab="Poisson's(model - measured)")

plot(x,linjehoy-linjelav,xlab=paste("\u0394","t(s) [µs/ft]"),ylab="95%
confidence interval")

hist(feil,main="Histogram",xlab="Poisson's ratio(mod - meas) [-]")

hist(residuals,main="Histogram",xlab=paste("Estimated Poisson's ratio
(","\u03C3","(c)=0) - fitted line"))

abline(v=qstd,col="red",lwd=2)

qqnorm(feil)

qqnorm(residuals)

svar<-cbind(sd(feil),sd(residuals))

return(svar)

}
```